

Microscopic properties of grain boundaries in Cu(In,Ga)Se₂ and CuInS₂ thin-film solar cells studied by transmission electron microscopy

vorgelegt von
Diplom-Physiker
Sebastian Simon Schmidt
aus Backnang

Von der Fakultät IV - Elektrotechnik und Informatik
der Technischen Universität Berlin
zur Erlangung des akademischen Grades
Doktor der Naturwissenschaften
Dr. rer. nat.

genehmigte Dissertation

Promotionsausschuss:

Vorsitzender: Prof. Dr. C. Boit
Gutachter: Prof. Dr. H.-W. Schock
Gutachter: Prof. Dr. B. Rech
Gutachter: Prof. Dr. H. Lichte

Tag der wissenschaftlichen Aussprache: 08.07.2011

Berlin 2011

D83

Zusammenfassung

Polykristalline Cu(In,Ga)Se₂- und Cu(In,Ga)S₂-Dünnschichten werden als Absorbermaterial in hocheffizienten Dünnschichtsolarzellen eingesetzt. Die Auswirkungen von Korngrenzen auf die elektronischen Eigenschaften dieser Dünnschichten und damit auf die Effizienz der entsprechenden Solarzellen sind nicht ausreichend verstanden. In der vorliegenden Arbeit wurden Methoden der Transmissionselektronenmikroskopie genutzt, um die mikroskopischen Eigenschaften von Korngrenzen in polykristallinen Cu(In,Ga)(Se,S)₂ Schichten zu untersuchen. Dazu wurde die integrale Zusammensetzung der Dünnschichten variiert.

Mittels Elektronenholographie wurde gemessen, dass das parallel zur Korngrenze gemittelte elektrostatische Potential, welches sowohl durch Atomkerne als auch durch Elektronen verursacht wird, in einem etwa 1 nm breiten Bereich um die Korngrenze um bis zu 3 V verringert ist. Die Tiefe dieser Potentialtöpfe unterscheidet sich von Korngrenze zu Korngrenze, sogar innerhalb derselben Cu(In,Ga)(Se,S)₂ Schicht, und ändert sich mit der integralen Zusammensetzung der Dünnschichten. Des Weiteren nimmt die Tiefe der Potentialtöpfe mit sinkender Symmetrie der Korngrenzen von $\Sigma 3$ Zwillings-, über $\Sigma 9$ Zwillingskorngrenzen bis hin zu Korngrenzen mit noch niedrigerer Symmetrie zu.

Eine gebundene Überschussladung an Korngrenzen und eine daraus resultierende Umverteilung von freien Ladungsträgern in der Umgebung, kann als alleinige Ursache der Potentialtöpfe ausgeschlossen werden. Deshalb kommen als Hauptursachen für die Potentialtöpfe eine lokale Änderung der Kristallstruktur bezüglich der Dichte und der Zusammensetzung in Frage. Die entsprechenden Beiträge werden in der vorliegenden Arbeit diskutiert.

Mit Hilfe von Elektronenenergieverlustspektroskopie wird ein Zusammenhang zwischen dem Auftreten der Potentialtöpfe und einer lokalen Änderung der Zusammensetzung an Korngrenzen aufgezeigt. Die gemessenen Zusammensetzungsänderungen hängen dabei stark von der integralen Zusammensetzung der Dünnschichten ab. In Cu(In,Ga)Se₂ Schichten mit $[Cu]/([In] + [Ga]) = 0.83$ wurde eine verringerte Cu- und eine erhöhte In-Konzentration an Korngrenzen gemessen, während in Schichten mit $[Cu]/([In] + [Ga]) = 0.43$ der umgekehrte Effekt beobachtet wird. Die gemessenen Unterschiede in den lokalen Cu- und In-Konzentrationen verhalten sich dabei immer entgegengesetzt. Basierend auf diesen Ergebnissen wird gezeigt, dass die gemessene Zusammensetzungsänderung einen großen Beitrag zu der Verringerung des elektrostatischen Potentials an Korngrenzen darstellen kann.

Ein Modell für das Banddiagramm an Korngrenzen in Cu(In,Ga)Se₂-Dünnschichten wird vorgestellt. Es basiert auf einer Verschiebung des Valenzbands zu niedrigeren Energien in einem etwa 1 nm breiten Bereich um die Korngrenze im Fall von Schichten mit einem Cu-Gehalt von $[Cu]/([In] + [Ga]) = 0.83$, wobei das Ausmaß der Verschiebung mit zunehmender Symmetrie der Korngrenzen kleiner wird. Im Fall von Korngrenzen in Schichten mit $[Cu]/([In] + [Ga]) = 0.43$ wird eine Verschiebung des Valenzbands zu höheren Energien vorgeschlagen.

Abstract

Polycrystalline Cu(In,Ga)Se₂ and Cu(In,Ga)S₂ thin films are employed as absorber layers in highly efficient thin-film solar cells. The impact of grain boundaries on the electronic properties of these thin films and consequently on the conversion efficiency of the corresponding solar cells is not sufficiently understood. In the present work, methods in transmission electron microscopy were employed in order to study the microscopic properties of grain boundaries in Cu(In,Ga)(Se,S)₂ layers with varying integral compositions.

Electron holography measurements show that the electrostatic potential caused by atomic nuclei and electrons, averaged parallel to the plane of the grain boundary, is lower in an about 1 nm wide region at grain boundaries by up to 3 V. The depths of these potential wells varies between individual grain boundaries, even within the same Cu(In,Ga)(Se,S)₂ layer, and with the integral composition of the investigated layer. The potential well depths increase from $\Sigma 3$ twin boundaries to $\Sigma 9$ twin boundaries and further to grain boundaries with even lower symmetry.

A bound excess charge at grain boundaries and a resulting redistribution of free charge carriers in the vicinity is ruled out as sole origin of the potential wells. Based on this result, it is concluded that major contributions to the measured potential wells may arise from a local change in the crystal structure with respect to the atomic density and the composition. The individual contributions are discussed in the present work.

By use of electron energy-loss spectroscopy, the presence of the potential wells at grain boundaries is correlated with the presence of a local change in composition. The changes in composition are found to depend strongly on the integral composition of the investigated layers. In the case of Cu(In,Ga)Se₂ thin films with a composition of $[Cu]/([In] + [Ga]) = 0.83$, a Cu deficiency and an In enrichment is found at grain boundaries, while the opposite effect is found in the case of thin films exhibiting $[Cu]/([In] + [Ga]) = 0.43$. The local changes in the atomic Cu and In concentrations always show an anticorrelated behavior. Based on these results, it is estimated that a local change in composition contributes significantly to the lowering of the electrostatic potential at grain boundaries.

A model for the band diagram at grain boundaries within Cu(In,Ga)Se₂ is proposed. This model comprises a local offset of the valence-band maximum towards lower energies in an about 1 – 2 nm wide region at the grain boundary in Cu(In,Ga)Se₂ thin films with a composition of $[Cu]/([In] + [Ga]) = 0.83$. The magnitude of the offset decreases with increasing grain boundary symmetry. For grain boundaries in Cu(In,Ga)Se₂ thin films with a composition of $[Cu]/([In] + [Ga]) = 0.43$, an offset of the valence-band maximum towards higher energies is proposed.

Contents

1	Introduction	1
2	Basics of Cu(In,Ga)Se₂ and CuInS₂ thin-film solar cells	5
2.1	Properties of Cu(In,Ga)Se ₂ and CuInS ₂ thin-film solar cells	5
2.1.1	Stacking sequence of the solar cells	5
2.1.2	Electronic band diagram of the solar cells	7
2.2	Properties of Cu(In,Ga)Se ₂ and CuInS ₂ thin films	8
2.2.1	Crystal structure of Cu(In,Ga)Se ₂ and CuInS ₂	8
2.2.2	Band-gap energies	10
2.2.3	Electrical properties and defects	11
2.2.4	Phase diagram	12
2.2.5	Influence of the composition on the electrical properties	13
2.2.6	The role of Na	15
2.2.7	Fabrication	16
2.3	Grain boundaries in polycrystalline Cu(In,Ga)(Se,S) ₂	17
2.3.1	Introduction into grain boundaries	18
2.3.2	Models of the electrical properties of grain boundaries	21
2.3.3	Overview of the characterization of grain boundaries	25
2.3.4	Summary on grain boundaries in Cu(In,Ga)(Se,S) ₂	29
3	Experimental methods and details	31
3.1	Properties of the investigated Cu(In,Ga)Se ₂ and CuInS ₂ thin films	31
3.2	Transmission electron microscopy	33
3.2.1	Basics	33
3.2.2	The principle of electron holography	34
3.2.3	Off-axis electron holography	38
3.2.4	Inline electron holography	41
3.2.5	Application of inline and off-axis electron holography	45
3.2.6	Determination of the averaged electrostatic potential	47
3.2.7	Electron energy-loss spectroscopy and energy-filtered imaging	50
3.2.8	TEM specimen preparation	52

3.3 Atom probe tomography	53
4 Grain boundaries in Cu(In,Ga)(Se,S)₂ thin films studied by TEM	55
4.1 Averaged electrostatic potential measurements	55
4.1.1 Grain boundaries in Cu(In,Ga)Se ₂ absorbers and their dependence on the integral composition	56
4.1.2 Comparison of off-axis and inline electron holography	61
4.1.3 The mean inner potential of CuInSe ₂	63
4.1.4 Grain boundaries in CuInS ₂ absorber films	64
4.1.5 Single $\Sigma 9$ grain boundary in CuGaSe ₂	65
4.1.6 Comparison of grain boundaries exhibiting different symmetries . .	66
4.2 Discussion on possible origins of the measured potential distributions . .	68
4.2.1 Redistribution of free charge carriers at grain boundaries	70
4.2.2 Electrostatic contribution to the strain at grain boundaries	85
4.2.3 Local change in composition and ionicity at grain boundaries	89
4.2.4 Effect of grain boundary geometry investigated by simulations . . .	92
4.2.5 Possible measurement artifacts	97
4.3 Comparison with studies on grain boundaries in other materials	100
4.4 Correlation between the potential wells and a local change in composition .	102
4.4.1 Experimental results	103
4.4.2 Discussion on local compositional changes, their origins and impacts	109
4.5 Grain boundary model	122
4.6 Summary of grain boundaries in Cu(In,Ga)(S,Se) ₂ studied by TEM . .	126
5 Concluding remarks and outlook	129
A Wave aberration function	133
B Transmission cross coefficient	135
Bibliography	137
Acknowledgements	156

Chapter 1

Introduction

Today, energy generated from the combustion of fossil fuels is the main energy source. However, the environmental pollution, the finite nature and instability of fossil fuel supply require an entirely new philosophy in the field of power generation urgently. Unless great progress will be made in nuclear fission, the ever increasing energy demand of the world population can only be satisfied in the long run by a mix of renewable energy sources. Besides wind, geothermal, and solar thermal energy, photovoltaics is a promising energy source. Especially the scope of local and mobile power generation makes photovoltaics an interesting choice even for everyone.

In photovoltaics, the power of solar light radiation is converted into electrical power, which is then fed into a power network. This process employs solar cells consisting of—depending on the type—several layers of doped semiconductors, and conductors for the contacts. In order to make photovoltaic systems competitive, especially in comparison with fossil fuels, highly efficient solar cells are required at low fabrication costs.

Currently, monocrystalline silicon based solar cells dominate the solar-cell market. About 25 % [1] conversion efficiency was achieved by monocrystalline silicon based solar cells on a laboratory scale, and commercially available modules—consisting of many serially connected solar cells—exhibit efficiencies of about 16 %. The solar cells consist of few hundred micron thick silicon wafers containing a *p-n* homojunction, i.e., a *n*-doped part and a *p*-doped part of the wafers. However, monocrystalline silicon has an indirect band gap and hence absorbs the solar light radiation less effective than direct band gap semiconductors. This requires a greater thickness compared with other solar cell types consisting of direct

band-gap semiconductors.

High energy consumption and material costs arising from the fabrication of the wafers are the main reason why less efficient thin-film solar cells can conquer the solar cell market. Solar cells based on the direct band-gap semiconductor Cu(In,Ga)Se₂ exhibit the highest conversion efficiency among thin-film solar cells. Already 20.3 % conversion efficiency have been achieved on a laboratory scale with a Cu(In,Ga)Se₂ based solar cell [1]. Such highly efficient Cu(In,Ga)Se₂ and also the related Cu(In,Ga)S₂ thin-film solar cells are typically produced in several layers of different materials, including a polycrystalline Cu(In,Ga)Se₂ or Cu(In,Ga)S₂ absorber layer.

The impact of interfaces between the different layers of the solar cell stack—and of internal interfaces, i.e., grain boundaries within the polycrystalline semiconductors—on the electrical properties of the solar cells is not sufficiently understood. Especially the role of grain boundaries in the Cu(In,Ga)Se₂ and Cu(In,Ga)S₂ absorbers has been under intense discussion for several years now. In order to improve the conversion efficiency of Cu(In,Ga)Se₂ and Cu(In,Ga)S₂ thin-film solar cells, further comprehensive understanding of grain boundaries within the polycrystalline absorber is fundamental.

In this work, transmission electron microscopy methods, i.e., electron holography and electron energy-loss spectroscopy, are applied in order to gain detailed insight into the microscopic properties of grain boundaries within polycrystalline Cu(In,Ga)Se₂ and Cu(In,Ga)S₂ thin films. The main focus is on grain boundaries within thin films that are employed in state of the art thin-film solar cells.

The outline of this thesis is as follows:

- Chapter 2 provides an introduction into Cu(In,Ga)Se₂ and CuInS₂ thin-film solar cells. The main focus is on the physical properties of the polycrystalline Cu(In,Ga)Se₂ and CuInS₂ absorber layer therein. The issue of grain boundaries within these layers is introduced and discussed with respect to existent models and to published studies.
- Chapter 3 presents the properties of the Cu(In,Ga)Se₂ and CuInS₂ layers analyzed in this thesis. The basics of the applied experimental methods, electron holography and electron energy-loss spectroscopy in transmission electron microscopy, are discussed. The application of both methods and the preparation of the TEM samples are addressed at the end of this chapter

- In Chapter 4, the properties of grain boundaries within Cu(In,Ga)Se₂ and CuInS₂ thin films are studied by use of electron holography and electron energy-loss spectroscopy in transmission electron microscopy. The results are presented and discussed in detail, also with respect to measurement artifacts and similar measurements on grain boundaries in other materials. A model, consistent with the results, is proposed and compared with the models available in the literature.
- Chapter 5 presents concluding remarks on the properties of grain boundaries within Cu(In,Ga)Se₂ and CuInS₂ thin films based on the results developed in Chapter 4. These remarks are combined with an outlook.

Chapter 2

Basics of Cu(In,Ga)Se₂ and CuInS₂ thin-film solar cells

This chapter introduces Cu(In,Ga)Se₂ and CuInS₂ thin-film solar cells. The layered device structure of the solar cells is illustrated and discussed with respect to the properties of each individual material layer as well as the complete device. The main focus is on summarizing the properties of the polycrystalline Cu(In,Ga)Se₂ and CuInS₂ layer within the solar cell stack. Especially the properties of the two solids, i.e., the crystal structure, the band gap and its dependence on the elemental composition, are presented and discussed. The chapter also covers the issue of grain boundaries within the polycrystalline Cu(In,Ga)Se₂ and CuInS₂ thin films.

2.1 Properties of Cu(In,Ga)Se₂ and CuInS₂ thin-film solar cells

2.1.1 Stacking sequence of the solar cells

A Cu(In,Ga)Se₂ and similarly a CuInS₂ thin-film solar cell consists of a number of material layers. The notation derives from a polycrystalline Cu(In,Ga)Se₂ or CuInS₂ layer within the solar cell stack which is the most relevant layer in the framework of this thesis. Fig. 2.1 shows a schematic of a typical layer stack, which is employed in current record efficiency Cu(In,Ga)Se₂ thin-film solar cells and a scanning transmission electron microscope (STEM)

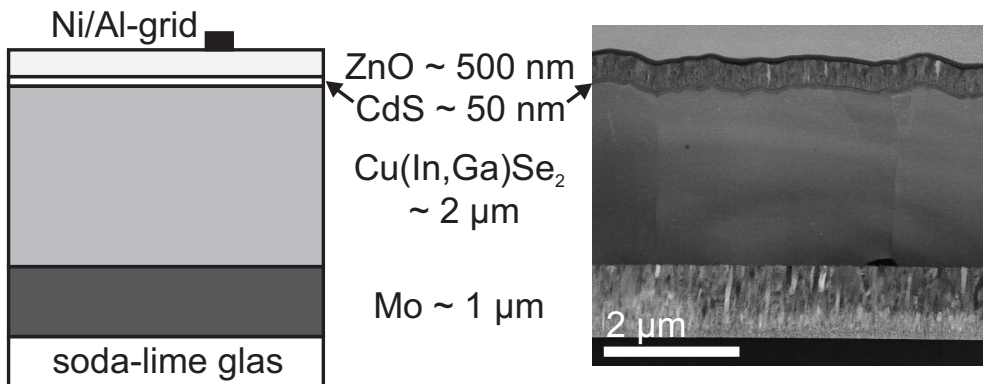


Figure 2.1: Schematic and STEM-HAADF image of the cross section of a Cu(In,Ga)Se₂-based thin-film solar cell. Several material layers are combined to a stack. This stack consists of a glass substrate, a Mo back contact, a *p*-type Cu(In,Ga)Se₂ layer, a *n*-type CdS buffer layer, and a *n*-type i-ZnO/ZnO:Al double layer. An Al/Ni-grid on top of the stack serves as front contact.

high angle annular dark field (HAADF) image of a Cu(In,Ga)Se₂ thin-film solar cell in cross-section view. The layer stacking sequence of deposition is as follows. Na containing soda-lime glass serves as a substrate for the thin-film solar cells. An approximately 1 μm thick polycrystalline molybdenum (Mo) layer is sputtered on top of the glass substrate. This Mo layer functions as the back electrode of the solar cells. On top of the back electrode, there is an about 2 μm thick polycrystalline Cu(In,Ga)Se₂ or CuInS₂ semiconductor layer, which is *p*-type. The crystal structure of device relevant Cu(In,Ga)Se₂ and CuInS₂ equals the crystal structure of chalcopyrite (CuFeS₂) which is why the compounds Cu(In,Ga)Se₂ and CuInS₂ will be referred to as chalcopyrites in the following. The fabrication of this layer is addressed in Sec. 3.1. An about 25 – 50 nm thick *n*-type CdS buffer layer is deposited on top of the Cu(In,Ga)Se₂ or CuInS₂ layer by means of chemical bath deposition. Subsequently, an approximately 500 nm thick transparent conductive oxide (TCO) double layer, consisting of intrinsic i-ZnO and Al doped ZnO (ZnO:Al), is sputtered on the CdS and serves as a transparent window for photons within the visible spectrum. Together with CdS, this layer forms the *n*-type part of the *p-n* junction of the solar cell. The front electrode is made of a Ni/Al grid which is deposited from the vapor phase.

In between the material layers, there are interfaces that may contain structural and electronic defects. The properties of these interfaces can have a huge impact on the properties of the complete solar cells. Therefore, the interfaces must be considered as additional layers

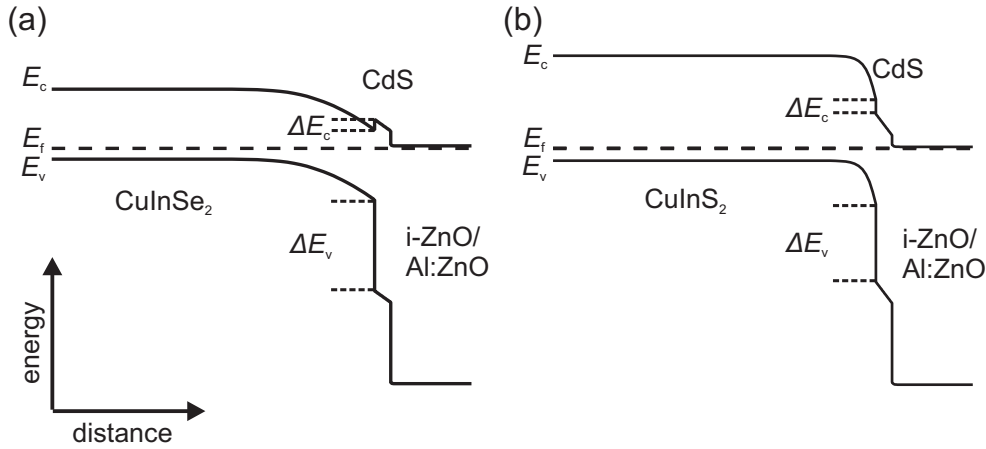


Figure 2.2: Schematics of the equilibrium band diagrams of (a) CuInSe₂ and (b) CuInS₂ thin-film solar cells, including the valence band maximum E_v , the conduction band minimum E_c , and the Fermi energy E_f . The conduction-band and valence-band offsets between the chalcopyrite-type layers and the CdS layers are denoted by ΔE_c and ΔE_v .

within the solar cell.

2.1.2 Electronic band diagram of the solar cells

The electronic band diagram of the completed Cu(In,Ga)Se₂ and CuInS₂ thin-film solar cells are still subject to intense discussions. Especially the interface between the Cu(In,Ga)Se₂ or CuInS₂ layer and the CdS is not understood sufficiently. Fig. 2.2 shows the current idea of the electronic band diagram of a CuInSe₂, and a CuInS₂ solar cell in equilibrium. CuInSe₂ has a band-gap energy of $E_g \approx 1.04$ eV [2, 3] and CuInS₂ of $E_g \approx 1.53$ eV [3, 4]. The band-gap energies and the dependence on the Ga-concentration will be discussed in detail in Sec. 2.2.2. For simplicity reasons, the Mo back contact is omitted at this point.

The electronic band diagrams are determined by the band-gap energies, the Fermi energies, and the electron affinities of the individual layers, as well as the properties of the interfaces between them [5]. Conduction- or valence-band discontinuities must occur at the interfaces between the layers due to their different band-gap energies. Values of conduction-band and valence-band offsets ΔE_c and ΔE_v at the interfaces can be estimated according to the model of Anderson [6, 7], which, however, neglects a possible dipole layer, as well as electronic defect states within the band gap at the interfaces.

A major difference between the two electronic band diagrams is located at the chalcopyrite-type/CdS interface. Photoelectron spectroscopy data [8] and theoretical calculations [9] suggest a negative valence-band offset and corresponding positive conduction-band offsets at the CuInSe₂/CdS interface. Similarly, the valence-band offset between CuInS₂ and the CdS layer was found to be negative. In contrast to the positive conduction-band offset at the CuInSe₂/CdS interface, however, measurements [10, 11] showed a negative conduction-band offset at the CuInS₂/CdS interface. In general, the sign and magnitude of such a conduction-band offset at the chalcopyrite-type/CdS interface may affect the electrical properties of the solar cell significantly. A negative conduction-band offset, as found in CuInS₂ thin-film solar cells, has shown to be detrimental to the conversion efficiency [12]. The different effective doping densities of Cu(In,Ga)Se₂ and CuInS₂ are responsible for the different band bendings and its spatial extension close to the interface with the CdS.

2.2 Properties of Cu(In,Ga)Se₂ and CuInS₂ thin films

The main focus of this thesis is on the Cu(In,Ga)Se₂ and CuInS₂ layers within the solar cell stack. They are typically *p*-type semiconductors, forming a *p-n* junction with *n*-type counterparts, and absorb the majority of the photons that contribute to the conversion of solar power into electrical power. Therefore, these layers are often referred to as the absorbers of the solar cells. As a result of an optimized fabrication-energy cost versus conversion efficiency relationship that empirically evolved in the past, the absorbers are polycrystalline in state of the art devices. In the following, the most important properties of Cu(In,Ga)Se₂, and CuInS₂ thin films are summarized.

2.2.1 Crystal structure of Cu(In,Ga)Se₂ and CuInS₂

Depending on the temperature and the element supply during the growth of compounds consisting of Cu, In, Ga, Se, and S, there are several phases possible, as well as corresponding crystal structures of the resulting solids. In this section, the main focus is on the α -phase Cu(In,Ga)Se₂ and CuInS₂ which crystallizes in the tetragonal chalcopyrite structure and is relevant for current thin films solar cells. Both materials are ternary I-III-VI₂ compounds, consisting of group I elements (Cu) and group III elements (In, Ga) in equal parts, as well as two parts of group VI elements (Se, S). In the following, I, III, and VI

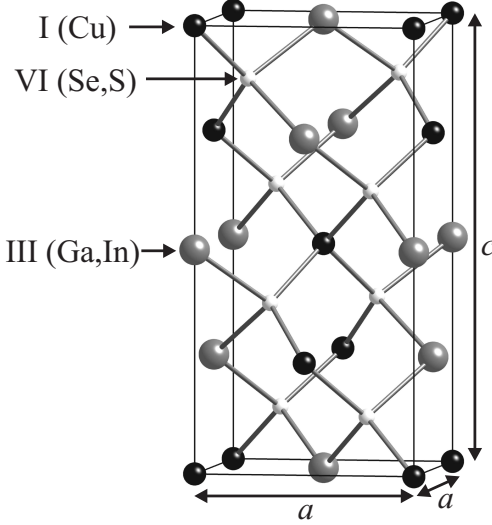


Figure 2.3: Unit cell of Cu(In,Ga)Se₂ and CuInS₂. I, III and VI show the positions of group I (Cu), group III (In, Ga), and group VI (Se, S) elements. The size of the unit cell in the three spatial dimensions is given by the lattice parameters a and c .

are used as synonyms for the elements of the corresponding group. The elements of each group occupy dedicated sites within the unit cell of the crystal structure.

The unit cell of the crystal structure, shown in Fig. 2.3, can be deduced from the cubic sphalerite (zincblende) structure by doubling its unit cell. The sphalerite structure itself corresponds to a modified diamond cubic structure, in which each carbon atom is bound to four carbon atoms in a tetrahedral configuration. In contrast to the diamond cubic structure, in the sphalerite structure, each atom is bound to four atoms of a different type. In diamond, the bonds between the atoms are covalent and form due to a sp^3 hybridization [13] of the s and p orbitals of the involved atoms. According to the Grimm-Sommerfeld rule, each atom provides four valence electrons to form the covalent bonds [14]. Similarly, the average number of valence electrons provided by the constituent atoms of Cu(In,Ga)Se₂ and CuInS₂ has to be four. In contrast to diamond and sphalerite, the bonds between Cu and Se or S result from a $p-d$ hybridization of the involved orbitals [15]. Due to the different electronegativity of the atoms, the bonds are not completely covalent but also show an ionic character. Theoretical calculations of the local charge density performed by Jaffe et al. [16] indicate that the bonds between group I and group VI elements exhibit a more covalent character, whereas the bonds between group III and group VI elements exhibit a more ionic character. As a consequence, the bonds between group I and group VI

elements and those between group III and group VI elements exhibit different bond lengths which is apparent in the tetragonal distortion $\delta = c/2a \neq 1$ of the crystal structure [17–19]. This is why it requires an extension of the cubic unit cell of the sphalerite structure. In the following, group I, and III elements and occupation sites will be also referred to as cations, and cation sites, whereas group VI elements and occupation sites will be referred to as anions, and anion sites.

2.2.2 Band-gap energies

The compounds Cu(In,Ga)Se₂ and CuInS₂ are semiconductors with a direct band gap at the Γ -point. CuInSe₂ and CuInS₂ have fundamental band-gap energies of about $E_g(\text{CuInSe}_2) \approx 1.04 \text{ eV}$ [2, 3] and $E_g(\text{CuInS}_2) \approx 1.53 \text{ eV}$ [3, 4].

In combination with spin-orbit coupling, the crystal field of the Cu atoms forces the initially degenerate Cu *d* orbitals into split energetic levels which form the valence-band maxima at the Γ -point. As a result, there is one fundamental band-gap energy and, depending on the compound, additionally allowed transitions between the conduction and the valence band [3, 20].

The fundamental band-gap energies of CuInSe₂ and CuInS₂ can be gradually manipulated to some extend by substituting In atoms for the same number of isovalent Ga atoms. The higher the Ga concentration, the higher is the band-gap energy of the compound. The band-gap energy of Cu(In,Ga)Se₂ for example is given by [21]

$$E_g(x_c) = (1 - x_c)E_g(\text{CuInSe}_2) + x_c E_g(\text{CuGaSe}_2) - bx_c(1 - x_c), \quad (2.1)$$

with $b = 0.15 - 0.24 \text{ eV}$ being an "optical bowing coefficient", and $x_c = [\text{Ga}] / ([\text{In}] + [\text{Ga}])$ being the ratio of the Ga concentration and the concentration of group III elements within the compound, and $E_g(\text{CuGaSe}_2) \approx 1.65 \text{ eV}$ [3]. While this band-gap manipulation is widely applied in the case of the Cu(In,Ga)Se₂ compound, it is less prominent in the fabrication of CuInS₂ based solar cells. This is due to the higher band-gap energy of CuInS₂ which is already close to the optimum band-gap energy for absorber materials within highly efficient thin-film solar cells with respect to the solar spectrum [22]. For this is of no importance in this thesis, the substitution of In for Ga in the case of CuInS₂ is disregarded in the following.

Interestingly, first-principle calculations of Wei et al. [23] indicate that the increase of the

fundamental band-gap energy of Cu(In,Ga)Se₂, upon an increase of the ratio x_c , occurs due to an upward shift of the conduction-band minimum, while the valence-band maximum shifts only slightly downwards. In general, first-principle calculations also suggest that the valence-band maximum is determined by an antibonding state which forms between Cu *d* and Se *p* orbitals, whereas the conduction band minimum is determined by group III *s* and Se *sp* orbitals [16, 24].

2.2.3 Electrical properties and defects

The electronic properties of semiconductors are governed by the degree of doping. Typical free hole densities within Cu(In,Ga)Se₂ and CuInS₂ thin films are in the range of 10^{16} - 10^{17} cm⁻³ at room temperature [25, 26]. In contrast to impurity doping applied for other semiconductors like silicon or GaAs, the electronic properties of Cu(In,Ga)Se₂, and CuInS₂ are usually governed by intrinsic defects. The following 12 intrinsic point defects exist in a ternary chalcopyrite

- 3 Vacancies (denoted by V_I, V_{III}, and V_{VI}),
- 3 Interstitials (denoted by I_i, III_i, VI_i),
- 6 Antisite defects (denoted by I_{III}, I_{VI}, III_I, III_{VI}, VI_I, and VI_{III}).

All these point defects have different enthalpies of formation and may act as acceptors or as donors. Calculations based on the macroscopic cavity model [27, 28] as well as on density-functional theory [23, 29] were applied to gain insight into this issue. It has been shown that the enthalpies of formation depend on the ratio x_c [23] as well as on the position of the Fermi energy and the chemical potential of the atomic species [29, 30]. Hence, the defect physics at polar surfaces possibly differs significantly from the defect physics in the volume of the chalcopyrite-type thin films.

The calculations further indicate that especially the enthalpy of formation of Cu vacancies (V_{Cu}^-), but also other vacancies and antisites, and the enthalpy of formation of the defect complexes ($2V_{Cu}^- + In_{Cu}^{2+}$), ($Cu_{In}^{2-} + In_{Cu}^{2+}$) are very small and in some cases even negative. Interestingly, the defect complex ($2V_{Cu}^- + Ga_{Cu}^{2+}$) was shown to have a higher enthalpy of formation than ($Cu_{In}^{2-} + In_{Cu}^{2+}$) in Cu(In,Ga)Se₂ [23]. Here, + and - denote the charge of the defect, if the atomic bonds showed only ionic character. Since this is not the case

(see Sec. 2.2.1) they simply indicate a tendency. In the simple model of ionic bonds, this suggests that the negatively charged V_{Cu}⁻ acts as a single acceptor and is responsible for the generally observed *p*-type doping of Cu(In,Ga)Se₂ and CuInS₂. A reduction of the Cu concentration by 2 at.%, which, according to the phase diagram, is allowed for the α phase (CuInSe₂) at 300 °C (see Fig. 2.4 in Sec. 2.2.4), would therefore result in a *p*-type doping of about $\approx 10^{21}$ cm⁻³¹.

This rough estimation and the calculated low enthalpy of formation of the defect complex (2V_{Cu}⁻ + In_{Cu}²⁺) indicate that there may be a high degree of self compensation of point defects, i.e., a coexistence of a high acceptor and a high donor density effectively compensating each other, which results in a small excess of acceptors responsible for the net *p*-type doping. There is experimental evidence for such a high degree of compensation within Cu(In,Ga)Se₂ [31]. Furthermore, these findings are able to explain the existence of stable phases CuIn₅Se₈ and CuIn₃Se₅, by successively removing units of (2V_{Cu}⁻ + In_{Cu}²⁺) from the CuInSe₂ unit cell [29]. These stable phases are sometimes referred to as ordered defect compounds (ODCs).

2.2.4 Phase diagram

Due to the high complexity of the defect physics, the process of fabrication of absorbers, suitable for the application within thin-film solar cells, in terms of temperature, supply of elements, reaction time etc., is very challenging. For the fabrication of Cu(In,Ga)Se₂ and Cu(In,Ga)S₂ thin films, it is therefore essential to understand and to control the growth process, since small deviations from stoichiometry may have a huge impact on intrinsic defects and along with it on the electronic properties. Although the deposition or growth of Cu(In,Ga)Se₂ and CuInS₂ is not a thermal equilibrium process, the thermal equilibrium phase diagram helps to understand the growth process. Fig. 2.4 shows the pseudo binary cut along the Cu₂Se-In₂S₃ section of the CuInSe₂ phase diagram. Note that a Cu content of 25 at.% corresponds to [Cu]/([In] + [Ga]) = 1. For temperatures up to 800 °C, there is a wide Cu concentration range of several at.%, where only the α phase, i.e., the chalcopyrite-type phase, exists. This means that, e.g. at 300 °C, the total Cu content may be varied by 2 - 3 at.% without changing the structure. For a Cu content of 25 at.% and higher, an additional (Cu,In)₂Se-phase coexists besides the α phase, the latter still exhibiting a

¹An atomic density within the crystal of about 4×10^{22} cm⁻³ was assumed

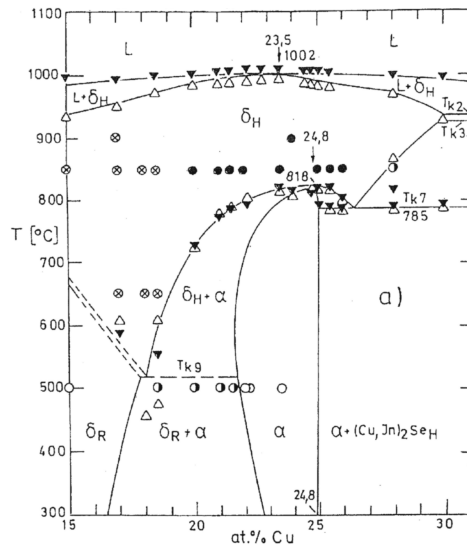


Figure 2.4: Phase diagram of CuInSe₂ along the quasi-binary cut In₂Se₃-Cu₂Se from [32]. The Greek letters α and δ denote the chalcopyrite-type CuInSe₂ phase and the compound CuIn₃Se₅.

Cu-content of about 23 to 24.8 at.%. At Cu contents below ~ 23 at.%, a phase with the chemical formula CuIn₃Se₅ coexists with the α phase. For Cu contents below ~ 16 - 17 at.%, only CuIn₃Se₅ is stable. CuIn₃Se₅ crystallizes in the same structure as CuInSe₂, however, its unit cell exhibits a defined number of Cu-vacancies V_{Cu}⁻ and antisite defects In_{Cu}.

The phase diagram of CuInS₂ is qualitatively similar to the one of CuInSe₂, however, it is not clear if a phase CuIn₃S₅ exists. Instead, for Cu contents below ~ 20 at.%, the phase CuIn₅S₈ coexists with the chalcopyrite phase.

2.2.5 Influence of the composition on the electrical properties

In the following, the focus is on compositional changes within Cu(In,Ga)Se₂, including other phases, and their effect on the electronic band diagram as well as the defect states. The impact of composition is assumed to be similar for CuInS₂, unless mentioned. Intrinsic as well as extrinsic compositional changes are covered as far as necessary for this work. Preliminary studies mainly restrict themselves to compositions or phases along the quasi-binary cut In₂Se₃-Cu₂Se.

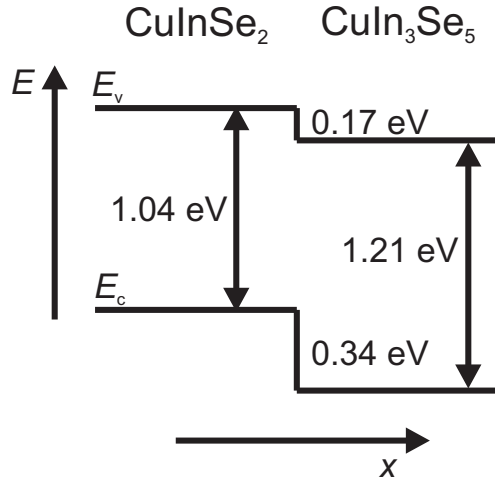


Figure 2.5: Electronic band diagram of a CuInSe₂-CuIn₃Se₅ interface after [29].

First, the impact of a variation of the Cu content of the chalcopyrites is considered. Such a variation may affect the doping density, as well as the band structure. According to several calculations, the Cu d orbital forms an antibonding state with the Se p orbital which is responsible for the energetic level determining the maximum of the valence band [29, 33, 34]. Persson et al. [33, 34] showed that (112) (cation) terminated surfaces of CuInSe₂ tend to reconstruct the lattice to a Cu deficient composition. A reduced repulsion of Cu d and Se p states therefore leads to a downward shift of the valence band maximum of few hundred meV, while, in the case of CuInSe₂, the conduction-band minimum almost remains at the same energetic level, resulting in an increase of the band-gap energy. A reduced Cu concentration at surfaces was indeed found in numerous experiments in the case of Cu(In,Ga)Se₂ layers exhibiting $[Cu]/([In] + [Ga]) > 1$ [35, 36]. Similarly, it has been shown that the valence-band maximum of the CuIn₃Se₅ phase, in which some Cu-vacancies are occupied by In, is few hundred meV lower compared with CuInSe₂ and the conduction-band minimum exhibits a negligible downward shift [29]. This is depicted in Fig. 2.5. An increased band-gap energy of these phases was indeed found by Wasim et al. [37] by means of optical absorption measurements. In the case of CuGaSe₂, a removal of Cu leads to a more pronounced downward shift of the valence-band maximum as well as a significant downward shift of the conduction-band minimum [34]. One may speculate that a local substitution of In by Cu, i.e., an increase of the Cu content, leads to an upward shift of the valence band maximum, due to an enhanced Cu d Se p repulsion, as long as the phase does

not change. However, experiments showed a negligible dependence of the band-gap energies on the [Cu]/([In] + [Ga]) ratio of near stoichiometric as well as Cu-rich samples [2]. This indicates that small compositional changes within the chalcopyrite phase rather influence the doping than the band structure. As soon as the Cu-content of the chalcopyrite exceeds ≈ 24.5 at.%, Cu_ySe ($1 \leq y \leq 2$) precipitates form which exhibit completely different electronic behavior compared with the chalcopyrite (see Fig. 2.4). Cu₂Se for example has a band-gap energy of about 1.2 eV and is a degenerate *p*-type semiconductor with the Fermi-level below the valence-band maximum [38, 39]).

Less is known about the band structure upon variations of group III elements or Se. The impact on the band structure upon an increase of the In-content and an increase of the relative Se-content in terms of CuIn₃Se₅ has already been discussed. The electrical properties of other In-rich phases are not discussed in the literature. Similarly, Cu_ySe ($1 \leq y \leq 2$) are the only In and Se poor phases discussed.

A comparison of Se and Cu/In terminated surfaces by means of density functional theory calculations shows that Se terminated $(\bar{1}\bar{1}\bar{2})$ planes of both chalcopyrites, CuInSe₂ and CuGaSe₂, exhibit almost no change in the band-gap energy and the band offsets are negligible [34]. This is due to a reconstruction of the subsurface atomic layer, in which In occupies Cu sites, and a relaxation of the surface Se layer.

2.2.6 The role of Na

The soda-lime glass substrate was shown to beneficially affect the conversion efficiency of the solar cells, especially in the case of Cu(In,Ga)Se₂ thin-film solar cells [40]. It became evident, that the Na within the soda-lime glass is responsible for this effect. During the deposition of the absorber, Na diffuses out of the substrate through the Mo layer into the absorber. It was found that this induces larger grain sizes as well as a smaller resistivity of the absorbers [41–45]. Conductivity, photoluminescence (PL) and deep level transient spectroscopy (DLTS) measurements suggest an increase of the *p*-type doping induced by Na, either through direct doping or indirectly by passivating donors, and additionally, a passivation of trap states deep within the band gap [44, 46, 47]. Possible mechanisms are Na occupying Cu-vacancies (V_{Cu}^-) thereby suppressing the compensating effect of In_{Cu}²⁺ which acts as a donor or the suppression of the formation of (V_{Cu}^- - V_{Se}^{2+}) defect complexes [44]. It is still unclear if the beneficial effect occurs due to a different absorber growth induced

by Na or simply by an increased *p*-type doping of the absorber independent from growth. Experiments with post absorber growth deposition of Na show a similar improvement of the solar cell performance and suggest that the change of the absorber growth conditions play a minor role compared with the effect of increased *p*-type doping [48, 49]. Based on DFT calculations, it was shown that an addition of Na to Cu(In,Ga)Se₂ increases the band-gap energy by lowering the valence-band maximum [33, 50]. Na on Cu-vacancies, similar to V_{Cu}⁻, reduces the Cu *d* Se *p* repulsion and affects predominantly the valence-band maximum. However, significant amounts of Na above 1 at.% may be required to induce this effect. Integral Na concentrations in Cu(In,Ga)Se₂ absorbers grown on soda-lime glass are typically smaller. However, local accumulations of Na, e.g. at grain boundaries, may be present.

Moreover, the passivation of surfaces and grain boundaries by Na, or Na-promoted O passivation is discussed [33, 51, 52]. Na as catalyst for O incorporation at surfaces and grain boundaries has been discussed by Kronik et al. [52]. The incorporated O passivates the donor states resulting from V_{Se}²⁺ (60 – 80 meV below the conduction-band minimum) which leads to a shallow acceptor 120 – 140 meV above the valence-band maximum [53].

2.2.7 Fabrication

Highly efficient Cu(In,Ga)Se₂ absorbers are usually deposited within a vacuum chamber from the vapor phase of the individual elements. This process is called physical vapor deposition (PVD). A co-evaporation of the elements during a multi-stage process [54, 55] has been shown to be beneficial for the device performance of the corresponding solar cells. Such a multi-stage process has a number of stages in which the elements—or combinations of elements—are evaporated sequentially. For this thesis, the absorbers were deposited on a rotating Mo-coated soda-lime glass substrate within the framework of a three-stage process:

- In stage one, In and Se (In-Se) are co-evaporated alternately with Ga and Se (Ga-Se) leading to a layered structure. The corresponding time intervals determine the final Ga content and, to some extent, the Ga grading within the absorber [56]. The substrate temperature is usually $\sim 330\text{ }^{\circ}\text{C}$.
- In stage two, Cu is co-evaporated together with Se (Cu-Se) and the substrate tem-

perature is increased to $\sim 525^{\circ}\text{C}$. Due to the higher substrate temperature, the elements alloy and the chalcopyrite phase forms. However, the substrate temperature affects the Ga grading significantly [55]. Usually, Cu and Se are co-evaporated until a Cu-rich composition is reached $[\text{Cu}] / ([\text{In}] + [\text{Ga}]) > 1$ in order to induce a larger grain size in the order of $1 \mu\text{m}$ during the growth process [57], which has been proven well empirically.

- In stage three, In, Ga, and Se are co-evaporated at the same substrate temperature as in stage two until the desired final Cu/III ratio of $[\text{Cu}] / ([\text{In}] + [\text{Ga}]) \approx 0.8 - 0.9$ is reached. Finally, the cooling down of the absorber is initiated.

During the whole process, the deposition of the absorber is monitored by the use of a pyrometer and a detector that measures diffusely scattered laser light applied on the surface of the deposited layer. Amongst others, the systems provide information about the thickness of the deposited layer, its roughness, and composition [58, 59] which effectively allows to control of the growth process to some extent.

2.3 Grain boundaries in polycrystalline Cu(In,Ga)Se₂ and Cu(In,Ga)Se₂ layers

Grain boundaries are defects within a polycrystalline material, where the structure deviates from the perfect crystal structure [60]. In many polycrystalline semiconductors, e.g. Silicon [61–63], GaAs [64–66], and ZnO [67], grain boundaries have shown to be detrimental for the conductivity behavior. On the other hand, grain boundaries in polycrystalline CdTe, which is employed as absorber layer in CdTe thin-film solar cells, are believed to affect the conversion efficiency of the corresponding solar cells beneficially [68–70]. In contrast to other polycrystalline thin-film solar cells, like CdTe and Si, conversion efficiencies beyond 20 % were achieved with Cu(In,Ga)Se₂ thin films solar cells on a small scale. This rises the following questions:

- How do grain boundaries affect the electrical properties of Cu(In,Ga)Se₂ and CuInS₂ thin films?
- What is the role of grain boundaries in the polycrystalline absorbers with respect to the conversion efficiency of the devices?

Both questions could not be answered so far. However, a deeper understanding of grain boundaries in polycrystalline Cu(In,Ga)Se₂ and CuInS₂ thin films might be the crucial factor leading to a further improvement of the conversion efficiency of the corresponding solar cells. This section gives a general introduction into the issue of grain boundaries within polycrystalline semiconductors before the main focus is on grain boundaries in Cu(In,Ga)Se₂, and CuInS₂ thin films. The currently most intensively discussed models of the electrical properties of grain boundaries in Cu(In,Ga)Se₂, and CuInS₂ thin films are summarized in this context. The last subsection gives a résumé of the previous experimental characterization.

2.3.1 Introduction into grain boundaries

Grain boundaries are considered as two dimensional—but not necessarily planar—defects within a polycrystalline material, where two misaligned crystalline grains meet [60]. They usually form during a nucleation based growth process of a material, when two individual crystals grown from individual nuclei with different crystal orientation contact each other. Although only localized to several atomic layers in between two grains, grain boundaries may have a large impact on the electrical properties of a polycrystalline semiconductor. In the formalism of the electronic band diagram, the local lattice distortions at grain boundaries may give rise to a distribution of electronic states within the band gap, i.e., a defect distribution. The probability of occupation of this defect distribution then determines the amount of excess charge which is bound at a grain boundary. Such bound charges induce an electric field which is screened by charges of opposite polarity. Hence, even local lattice distortions or compositional changes may influence the current transport behavior through the correlated potential barriers or wells.

A defect distribution within the band gap also decreases the mean lifetime of free electrons and holes in the local vicinity, since the small—smaller than the band-gap energy—energetic differences between the states increase the transition probability between the states due to a more effective interaction with phonons. The process, where electrons change their electronic state from the conduction band to the valence band via a cascade of transitions involving phonons, is termed recombination via defect states. Note that the inverse process, which is termed generation, has the same rate in equilibrium. The timescale of these processes is usually much smaller than the timescale of band-to-band

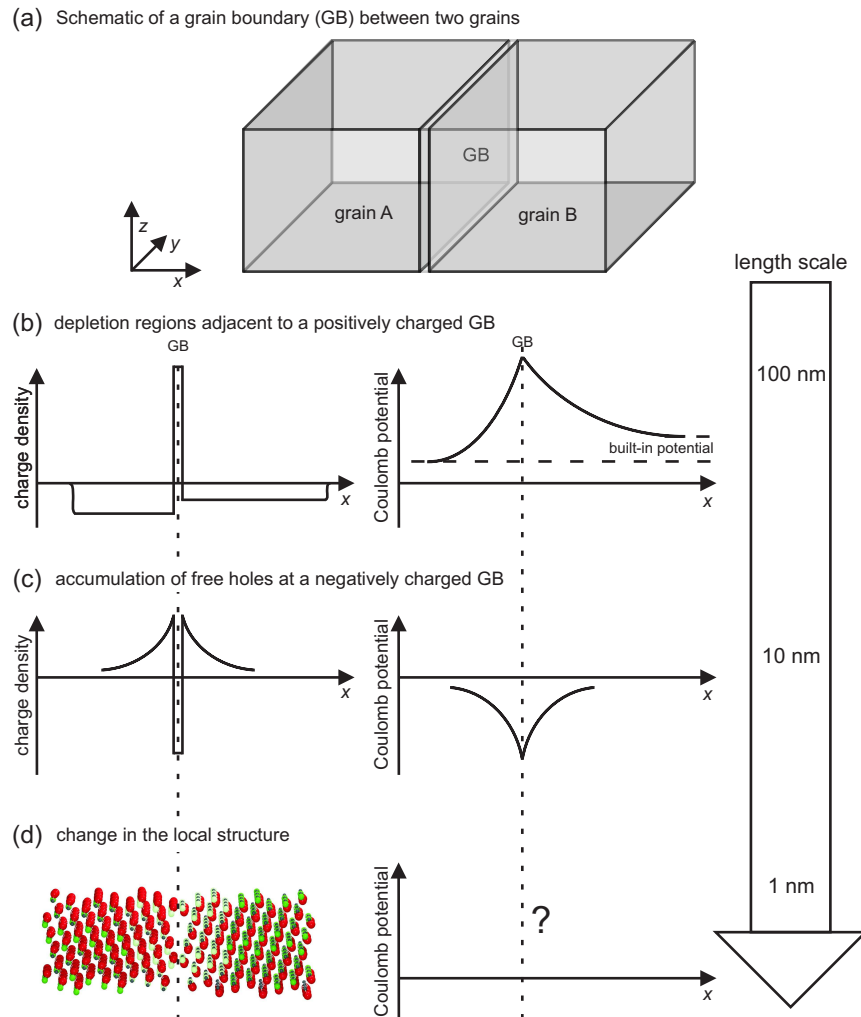


Figure 2.6: Schematic of a grain boundary and the length scales on which a grain boundary can have an impact on the adjacent grains in a *p*-type semiconductor with a doping density of about $1 \times 10^{16} \text{ cm}^{-3}$. (a) A grain boundary (GB) between two adjacent grains. (b) Charge density and resulting Coulomb potential if positive charge is bound at the grain boundary. A space charge region forms on either side of the grain boundary screening the electric field generated by the bound charge on a length scale of few 100 nm. A built-in potential forms if two adjacent grains exhibit different doping densities, even if no charge is bound at the grain boundary. (c) Charge density and resulting Coulomb potential if negative charge is bound at the grain boundary. An accumulation of free holes in the valence band screens the electric field of the negative bound charge on a length scale of few 10 nm. (d) The local atomic lattice determines the Coulomb potential and the electronic defect states within the band gap on a length scale of about few nm.

recombination or the transition via a single electronic state within the band gap, for which the interaction with photons is the dominant process. Under applied voltage or solar irradiation, the recombination rate outbalances the generation rate in the local vicinity of a defect distribution, and results in a locally smaller free charge carrier density. The recombination via defect states is therefore considered as detrimental for the conversion efficiency of corresponding solar cells.

Fig. 2.6 illustrates a grain boundary between two neighboring grains, and outlines different scenarios and lengthscales on which a grain boundary in a *p*-type semiconductor with a doping density in the order of $1 \times 10^{16} \text{ cm}^{-3}$ may affect the charge densities, and the resulting Coulomb potential in the adjacent grains. If no band discontinuities are present, the behavior of the Coulomb potential can be directly translated into the potential energy, which determines the electronic band diagram, by multiplication with the electron charge $-e$. It can be seen that length scales from the μm range down to the \AA range must be considered to fully describe a grain boundary.

There are various types of grain boundaries which can be distinguished depending on the misalignment of the adjacent grains. A possible differentiating factor may be the orientation relation between the two adjacent grains or the concept of the coincidence site lattice. In the latter, the ratio between the unit cell volume of the coincidence site lattice, which is obtained if the crystal lattice of one grain is continued into the other grain, and the unit cell volume of the crystal lattice [60] relates the orientation of one grain to the other. In the coincidence site lattice description, grain boundaries are denoted by the Greek letter Σ and the value of the described ratio.

In device grade polycrystalline Cu(In,Ga)Se₂, and CuInS₂ thin films which are actually applied in thin-film solar cells, the average grain size is usually smaller than the film thickness. In contrast to other semiconductors, e.g. silicon, a direct correlation between the average grain size and the conversion efficiency of the corresponding solar cells could not be found. Similarly to the electric properties, little is known about the structure and local composition of grain boundaries within Cu(In,Ga)Se₂, and CuInS₂. Only the structure of highly symmetric twin grain boundaries, for which the crystal lattices of the adjacent grains exhibit a mirror symmetry, have been studied in some detail [71, 72]. This is clearly not sufficient to understand the larger set of grain boundaries without a highly symmetric configuration. Hence, there is a lack of investigations of grain boundaries in device grade polycrystalline Cu(In,Ga)Se₂, and CuInS₂ thin films, which requires further studies. The

most important models expressing the current understanding of grain boundaries within Cu(In,Ga)Se₂, and CuInS₂ are described in the following section.

2.3.2 Models of the electrical properties of grain boundaries

As discussed in the last section, the electrical properties of grain boundaries within polycrystalline Cu(In,Ga)Se₂ thin films may play an important role for the conversion efficiency of the corresponding solar cells. It is therefore essential to get an idea about the electronic band diagram at and in the vicinity of grain boundaries to understand the impact on the solar cells. Few models have been proposed in the past describing the electronic band diagram of grain boundaries within polycrystalline Cu(In,Ga)Se₂ thin films. Some of them are based on grain boundary models that were established for other materials, like silicon and GaAs, and some of them are based on material specific measurements or calculations. So far, the models are restricted to Cu(In,Ga)Se₂ but might be applicable to Cu(In,Ga)S₂ as well. The following four models (see also Fig. 2.7) have proven of value to explain results of electrical and microscopic measurements.

2.3.2.1 Model of electrically benign grain boundaries

Yan et al. [51, 73] proposed electronically benign grain boundaries. Their model is based on DFT calculations on two $\Sigma 3$ grain boundary models containing dislocation cores, i.e., regions, where the interatomic bonds are broken or forced to have different lengths compared with the grain interior. The calculations show that, in contrast to polycrystalline silicon and CdTe, a lattice relaxation in Cu(In,Ga)Se₂ is responsible for a shift of electronic defect states from the band gap into the valence band. The electronic band diagram at the grain boundary is indistinguishable from the one in the grain interior. This is illustrated in Fig. 2.7(a). Without electronic states within the band gap, the dominant recombination path is the interaction with photons. The local net recombination under perturbations is therefore similar compared with the one far away from the grain boundaries. A similar but more phenomenological model was proposed by Cahen et al. [74] already in 1989. They suggested that oxygen, which is incorporated into the solar cell absorbers as soon as they are exposed to air, leads to a passivation of (positively charged) Se vacancies at surfaces and grain boundaries within Cu(In,Ga)Se₂. This passivation leads to a neutralization or at least to a reduction of charge located at the grain boundaries and consequently to an

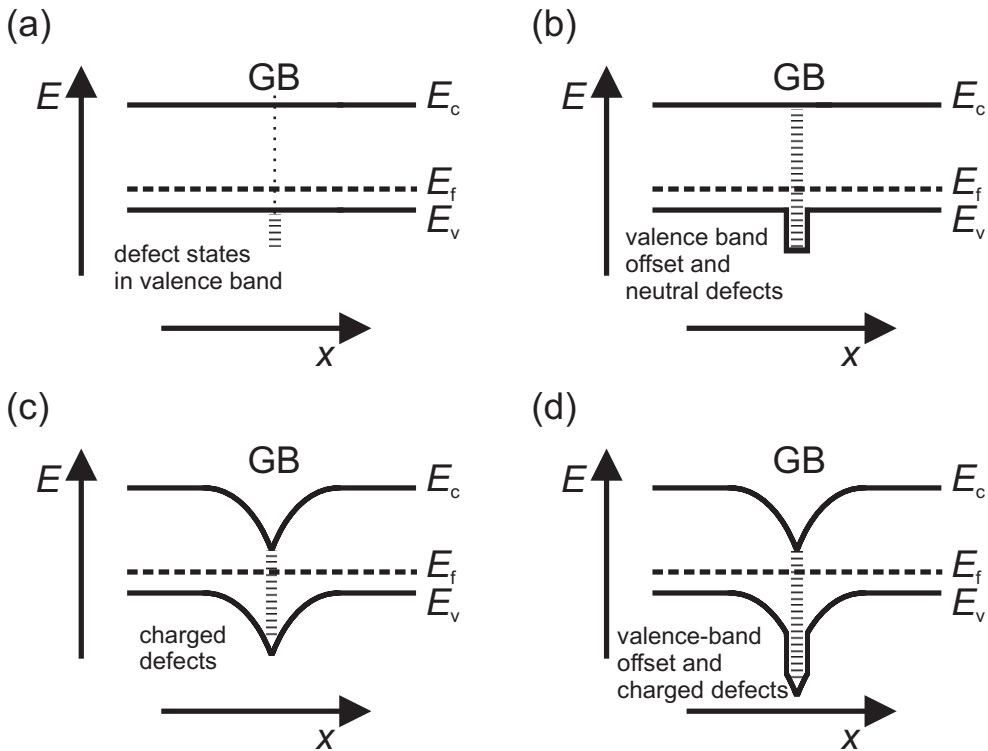


Figure 2.7: Schematic of the electronic band diagrams of the grain boundary models discussed in the text. The respective length scales are depicted in Fig. 2.6. Defect distributions within the band gap are denoted by a sequence of dashes. (a) Yan et al. proposed the model of electrically benign grain boundaries (see Sec. 2.3.2.1). A local relaxation of the crystal lattice is responsible for a shift of electronic defect states from the band gap into the valence band. The electronic band diagram at the grain boundary is indistinguishable from the one in the grain interior in the framework of this model. (b) A valence-band offset of several hundred mV and a width of a few atomic layers at a grain boundary without charged defects, according to the model of Persson et al. (see Sec. 2.3.2.2). (c) In the Seto model (see Sec. 2.3.2.3), a positive, bound excess charge at the grain boundary (GB) causes a space charge region, which leads to a downward bending of the bands towards the grain boundary core. (d) A valence-band offset in combination with a space charge region as proposed by Hafemeister et al. (see Sec. 2.3.2.4).

improvement of the performance of the corresponding solar cells, especially after an annealing of the solar cell absorbers in air. Later, this model was extended to include Na as a catalyst for surface oxidation [52, 75].

2.3.2.2 Valence band offset model

Based on density functional theory (DFT) calculations on a (112) $\Sigma 3$ twin grain boundary, Persson et al. [33, 34] proposed a neutral transport barrier, i.e., a valence-band offset, to be present at the grain boundary. For their calculations, they assumed that the grain boundary consists of two stable (112) surfaces of Cu(In,Ga)Se₂ crystals, each surface exhibiting a Cu-poor composition [76–78], facing each other. This assumption is based on the observation that surfaces of CuInSe₂ exhibit a Cu-poor composition [35]. They found that a Cu-poor composition of such grain boundaries should lead to a valence-band offset of several hundred meV towards lower energies which is few atomic layers in width. Fig. 2.7(b) shows the corresponding electronic band diagram. A reduced repulsion of Se *p*, and Cu *d* states, both forming an antibonding state at the valence-band maximum, is responsible for the valence-band shift to lower energies. Due to the valence-band offset, a reduced free hole density is present at the grain boundary leaving less unoccupied states available for electrons within the conduction band, which effectively results in a reduced recombination rate. If a voltage or irradiation perturbs this system, the net recombination rate at the grain boundary is reduced compared with the case without the valence-band offset.

2.3.2.3 The Seto model

In order to explain the electrical properties of *p*-type polycrystalline silicon films, i.e., the temperature dependence of the measured resistivity and Hall mobility, Seto [79] proposed a space charge region being present at grain boundaries. In his model, electronic states within the band gap are assumed to exist at the grain boundaries due to imperfections of the lattice, which was already proposed by [61]. These electronic states are occupied by holes and result in a positive excess charge at the grain boundaries which is screened by a negatively charged space charge region on both adjacent sides. For the current transport through grain boundaries, this means that the majority carriers (holes) have to overcome a potential barrier. This process can be described by thermionic emission theory. Seto's model has later been adopted for grain boundaries within polycrystalline Cu(In,Ga)Se₂ (and CuInS₂ films) in order to explain surface sensitive Kelvin probe force microscopy (KPFM) measurements, which suggest the presence of a positive excess charge at grain boundaries (e.g. see Refs. [80, 81]). The corresponding electronic band diagram is shown in

Fig. 2.7(c). Assuming that the band bending close to the grain boundary is less than about half the band-gap energy, this configuration leads to a locally increased net recombination rate via defect states at the grain boundaries, if the thin films are perturbed by the application of a voltage or solar irradiation [82]. This is because the free electron and free hole densities become similar, i.e., the number of occupied electronic states in the conduction band and the number of unoccupied electronic states in the valence band become similar. If the band bending is larger than about half the band-gap energy, the net recombination rate may become smaller again [82].

2.3.2.4 Model of space charge and additional neutral tunneling barrier

Azulay et al. [83] proposed a valence-band offset of several hundred meV in addition to a downward bending of the electronic bands of about 100 meV to be responsible for an increased current through grain boundaries compared with the bulk which they measured with conductive atomic force microscopy (C-AFM) for applied voltages smaller than 1 V. The downward bending of the bands was suggested, since the direction of the current switches sign for an applied bias of about 100 mV. A valence-band offset in combination with a downward bending of the bands can therefore lead to an increased current density through grain boundaries under external perturbations.

Recently, Hafemeister et al. [84] proposed a similar model. They suggested the presence of a 1 - 2 nm narrow and several hundred mV deep neutral tunneling barrier for majority carriers at a $\Sigma 3$ and $\Sigma 9$ grain boundary in CuGaSe₂. Based on KPFM measurements, they also suggested a space charge region to be present at the $\Sigma 9$ but not at the previously investigated $\Sigma 3$ grain boundary [85]. Fig. 2.7(d) shows the electronic band diagrams in the case of the $\Sigma 9$ grain boundary. Their model is based on results of resistivity, Hall and KPFM measurements. The model has been applied earlier to describe the conductivity of polycrystalline silicon [86]. In general, it is the balance between the detrimental downward band bending, the valence-band offset, and the properties of the defect density at grain boundaries which determines the local net recombination rate under applied voltage or solar irradiation.

2.3.3 Overview of the characterization of grain boundaries

Numerous measurements have been performed in the past in order to study the properties of grain boundaries within polycrystalline Cu(In,Ga)Se₂. The applied techniques can be roughly divided into three main categories. The respective results are summarized in the following. Less effort has been made to study grain boundaries within the related material Cu(In,Ga)S₂.

2.3.3.1 Electron microscopy and atom probe tomography

Various techniques in the transmission electron microscope and the scanning electron microscope have been employed to investigate the structure, the composition as well as the electrical properties of grain boundaries within Cu(In,Ga)Se₂. Furthermore, electron backscatter diffraction (EBSD) in SEM has been utilized in order to provide statistics on the relative frequency of grain boundaries and grain boundary types. In the following, the focus will be on the structure and composition of grain boundaries within Cu(In,Ga)Se₂ thin films. The relevant length scale is in the order of few nm.

By use of TEM, the particular structure of grain boundaries can only be studied if both adjacent grains are oriented in zone axis. This is only possible in the case of a few highly symmetric grain boundaries. These in turn may not generate a high defect density or charge density at the grain boundary core and may be of little interest with respect to the overall solar cell efficiency.

Yan et al. [72] performed high-resolution Z-contrast imaging in STEM on a $\Sigma 3$ twin grain boundary within Cu(In,Ga)Se₂, where the grain boundary is a (112) plane with respect to both adjacent grains. They found that the stacking sequence of the lattice does not end at the grain boundary but is rather reversed. Hence, the grain boundary can not be described by two (112) surfaces, for which the stacking sequence ends at the surface, facing each other as proposed by Persson et al. [33, 34]. Furthermore, they were not able to measure a Cu-poor composition close to the grain boundary by means of high resolution Z-contrast imaging and nanoprobe energy-dispersive X-ray spectrometry in scanning mode of the transmission electron microscope (STEM-EDX). Another investigation of the chemical composition at grain boundaries has been performed by Lei et al. [87]. STEM-EDX measurements at high angle grain boundaries revealed no substantial change in composition compared with the grain interior. However, the applied point to point distance of

> 10 nm is not sufficient to detect changes in composition on smaller length scales.

Auger electron spectroscopy (AES) has been applied on grain boundaries by the groups of Hetzer et al. [88] and Niles et al. [89] in the scanning electron microscope. Hetzer et al. measured a massively reduced Cu-concentration at the investigated grain boundaries and Niles et al. found Na and O impurities primarily residing at grain boundaries. However, in both publications, the grain boundaries were not explicitly identified by means of EBSD but from the topography of the sample or the Auger electron signal. In addition, AES is a very surface sensitive technique. A different chemical absorption behavior of grain boundaries at surfaces compared with the volume may have a huge impact on these kind of measurements. In summary, the results on the structure and composition of grain boundaries within Cu(In,Ga)Se₂ given in the literature remain ambiguous.

Complementary cathodoluminescence (CL) and electron beam induced current (EBIC) measurements in the SEM and TEM provide elegant methods to study the electrical properties of grain boundaries within Cu(In,Ga)Se₂ and CuInS₂ on a length scale of about few tens of nm. In CL, the measured signal is the local photon current density caused by radiative recombination of free electrons and holes which were generated by local irradiation with an electron beam. In EBIC, the corresponding charge current density which is flowing through the device contacts under short circuit conditions is measured. Most of the performed CL measurements showed a decrease of the total CL signal at grain boundaries [90–93]. However, the degree of the decrease in the CL signal depends on the texture [90] and the Na content [93] of the investigated thin films. Abou-Ras et al. [92] also showed that $\Sigma 3$ grain boundaries within Cu(In,Ga)S₂ exhibit a less pronounced reduction in the CL signal than random non $\Sigma 3$ grain boundaries. Similar results, measured at the back surface of Cu(In,Ga)Se₂ absorbers which were stripped off from the Mo back contact, have been found recently by Kavalakkatt [94]. Romero et al. [91] measured a redshift of the averaged CL intensity along grain boundaries. Evidently, there is less radiative recombination occurring at most grain boundaries compared with the bulk material. EBIC measurements of Nichterwitz et al. [95] showed a reduced current from some grain boundaries. They successfully modeled the reduced current collection at a grain boundary by assuming an increased recombination velocity at the plane of the grain boundary. Additional measurements of Kavalakkatt [94] also showed that the measured current seems to depend on the grain boundary type, i.e., $\Sigma 3$ or random. Similarly to the CL results, the decrease in the EBIC signal at random grain boundaries is substantially higher compared with $\Sigma 3$.

grain boundaries, for which almost no EBIC contrast could be detected. All this indicates that the reduction in radiative recombination at grain boundaries is in favor of the faster non-radiative recombination path, at least for non $\Sigma 3$ grain boundaries.

Recently, Cadel et al. [96] performed atom probe measurements on grain boundaries. They found an increased Na concentration of about 0.89 at.% at grain boundaries, less Se and a different Cu, Ga, and Se contents in the two adjacent grains.

2.3.3.2 Surface scanning techniques

Kelvin probe force microscopy (KPFM) as well as other scanning techniques like scanning tunneling microscopy (STM) and atomic force microscopy (AFM) are suitable in order to study the surface properties of polycrystalline chalcopyrites on length scales of few nm. For the former, the general procedure of most groups is to measure the topography of a certain area of interest on the specimen, and afterwards the contact potential of the same area of interest, from which the work function can be determined. Regardless of the particular material composition, almost all measurements, showed either no change in work function or a dip of the work function across grain boundaries with a full width at half maximum of 50 - 100 nm [80, 84, 85, 93, 97–103]. This corresponds to a downward bending of conduction and valence band if the band gap is unchanged. Only Hannah et al. [93] measured a slight increase of the work function at grain boundaries in Na containing (220/204)-textured thin films, which they attributed to a negative excess charge at the grain boundary and a corresponding upward bending of the electronic bands towards the grain boundary. In contrast, Yan et al. [51] found a reduction of the work function across grain boundaries in Na containing thin films which is not present in Na free thin films. Again, the complexity of the material requires a discrimination of the Ga content, the texture, and the Na content of the specimens as well as the studied grain boundary types. These parameters are in turn strongly linked with the fabrication process of the chalcopyrites. This issue, however, is not addressed at this point.

Jiang et al. [100, 101] measured a dip in the work function across grain boundaries within CuInSe₂ of about 150 mV but no change of the work function across grain boundaries within CuGaSe₂. In contrast, other groups found a reduction in work function of 50 - 150 mV also in CuGaSe₂ [80, 84, 97–99]. However, the investigated $\Sigma 3$ grain boundaries within CuGaSe₂ showed no dip of the work function [85, 102]. For some grain boundaries

within CuGaSe₂, illumination with red light resulted in a reduction of the work function dip [80, 97–99], whereas others showed no response. This indicates that at least two types of grain boundaries have to be distinguished.

KPFM measurements are very sensitive to the surface properties of the investigated samples. Therefore, it is worth mentioning that KPFM measurements which were performed on etched or polished samples [103] (CuInS₂) exhibited no contrast of the work function at grain boundaries.

A subsidiary approach present conductive atomic force microscopy (C-AFM) measurements performed by Azulay et al. [83] and scanning tunneling microscopy measurements (STM) performed by Romero et al. [104–106]. In order to explain a reduced photoemission at CuInSe₂ grain boundaries measured upon current injection through a scanning tunneling microscope, they suggested a reduced free hole density being present at the grain boundaries [104]. Electroluminescence mapping of CuGaSe₂ solar cells, for which a voltage was locally applied by an atomic force microscopy tip [106], showed that the transport of an injected current is confined to individual grains and does not spread to adjacent grains. Therefore, grain boundaries seem to act as an insulator between grains. By means of electro-assisted STM Romero et al. [105] further measured a barrier for free electrons located at the grain boundaries within CuGaSe₂. Again, the grain boundaries were not explicitly identified by suitable techniques, e.g. EBSD, in most publications mentioned above. Topography grooves mostly served as indication. An exception are the works on single grain boundaries within CuGaSe₂ [84, 85, 102].

2.3.3.3 Electrical measurements

Temperature dependent resistivity and Hall measurements on Cu(In,Ga)Se₂ and CuInS₂ thin films aim at studying a possible energetic barrier for majority carriers at grain boundaries. Such a barrier should manifest itself in an activation energy of the hole mobility μ_{mob} . Besides the resistivity and Hall measurements on single $\Sigma 3$ and $\Sigma 9$ grain boundaries within CuGaSe₂ [84, 85], all measurements were performed on polycrystalline samples which were fabricated by co-evaporation or sequential processes. In general, the conversion efficiencies of Cu(In,Ga)Se₂ based solar cells depend very sensitively on the fabrication process of the absorber. Since all resistivity measurements showed similar results, details with respect to the fabrication processes are disregarded at this point.

So far, the activation energies of the conductivity σ determined by means of resistivity measurements exhibited values between 30 and 350 meV [107–110]. Activation energies above 150 meV have been found only in Na free samples [107, 109]. It is not clear, if this activation energy can be attributed to a potential barrier for holes, since the conductivity $\sigma = e\mu_{mob}p$ is also determined by the charge-carrier density p . Hence, the measured activation energy is determined by both, the activation energy of the charge-carrier density p and the activation energy of the mobility μ_{mob} . Rissom [110] found activation energies of the charge carrier density p of about 150 meV in polycrystalline CuGaSe₂ which he deduced from Hall measurements. Resistivity measurements in the same study showed very similar activation energies of the conductivity indicating that the activation energy is mainly determined by the activation of the charge carrier density p and not by the activation of the mobility μ_{mob} . Other studies which employed a combination of resistivity and Hall measurements found an activation energy of the mobility of 50 - 135 meV for polycrystalline Cu(In,Ga)Se₂ [25, 111, 112], 32 meV and 100 meV for a single Σ 3 and a Σ 9 grain boundary within CuGaSe₂ [84, 85] as well as 50 - 60 meV for polycrystalline p -doped CuInS₂ [26]. As implemented in the work of Hafemeister et al. [84], it is not necessary to assume band bending due to a space charge region at the grain boundaries in order to model the temperature dependence of the Hall mobility and the resistivity which they measured across a single Σ 3 grain boundary. The temperature dependence can be equally well simulated by assuming a several nm wide potential barrier for holes, only few tens of meV deep, and in addition a 1 - 2 nm wide and several hundred meV deep valence-band offset through which the holes may tunnel through.

2.3.4 Summary on grain boundaries in Cu(In,Ga)(Se,S)₂

The presence of local lattice distortions at grain boundaries may give rise to a bound excess charge, causing potential barriers or wells, and a locally increased recombination rate of free charge carriers. Both effects are usually considered as detrimental for the conversion efficiency of the corresponding solar cell [81, 82], however, this is not necessarily the case. Some models have been proposed in the past describing the electrical properties of grain boundaries within polycrystalline Cu(In,Ga)Se₂ films (see Sec. 2.3.2). In these models, the presence of bound excess charge, a local relaxation of the lattice, and a local change in composition at grain boundaries are considered.

However, the main outcome of previous characterizations of grain boundaries within polycrystalline Cu(In,Ga)(Se,S)₂ layers is that individual grain boundaries exhibit individual physical properties. The properties depend at least on the grain boundary symmetry, the integral composition of the polycrystalline layer, its texture and the presence of impurity atoms. Especially surface scanning measurements also suggest a strong dependency of the results on the particular treatment of the polycrystalline layers before the measurement. These findings make it difficult to develop a general grain boundary model.

The approach of this thesis is to gain more insight into the properties of grain boundaries on an sub nm length scale since the very local lattice distortions at grain boundaries may determine their electrical properties in a much larger length scale of up to μm . In particular, electron holography and electron energy-loss spectroscopy in transmission electron microscopy are applied, for they provide the possibility to investigate the local Coulomb potential and the local composition on a length scale below 1 nm.

Chapter 3

Experimental methods and details

This chapter gives an overview of the experimental methods that were applied in the framework of this thesis. The overview covers the particular fabrication of the investigated Cu(In,Ga)Se₂ and CuInS₂ thin films, as well as the characterization methods employed to analyze these thin films. The main focus will be on transmission electron microscopy, especially the techniques of electron holography and electron energy-loss spectroscopy.

3.1 Properties of the investigated Cu(In,Ga)Se₂ and CuInS₂ thin films

The Cu(In,Ga)Se₂ thin films being investigated in the present thesis were prepared in such a way that they exhibit varying nominal compositions. The main focus is on a series of Cu(In,Ga)Se₂ thin films with a constant Ga content of $[Ga]/([In] + [Ga]) \approx 0.3$ and varying Cu contents $[Cu]/([In] + [Ga])$ of 0.83, 0.67, and 0.43, and on a series with a constant Cu content of ~ 0.85 and varying Ga contents of 0, 0.45, and 1. The nominal composition of these thin films are presented in Tab. 3.1.

The fabrication method for the Cu(In,Ga)Se₂ layers of these two series will be addressed briefly in the following. The series of thin films in which the Ga content was varied will be referred to as Ga series, whereas that in which the Cu content was varied will be referred to as Cu series.

First, the fabrication of the Cu series is depicted. In the first stage, Ga-Se and In-Se were co-evaporated alternatingly at a nominal substrate temperature of 330 °C, such that a final

Table 3.1: The atomic concentrations and respective ratios $[Cu]/([In] + [Ga])$ and $[Ga]/([In] + [Ga])$ with respect to the integral composition of the $Cu(In,Ga)Se_2$ thin film solar cell absorbers investigated in this work measured by use of X-ray fluorescence spectroscopy.

	[Cu] (at. %)	[In] (at. %)	[Ga] (at. %)	[Se] (at. %)	$\frac{[Cu]}{[In]+[Ga]}$	$\frac{[Ga]}{[In]+[Ga]}$
Cu series						
	22	19	8	51	0.83	0.28
	19	20	9	52	0.67	0.31
	14	22	10	54	0.43	0.32
Ga series						
	22	28	0	50	0.82	0
	22	15	12	51	0.82	0.45
	23	0	26	51	0.88	1

composition ratio of $[Ga]/([In] + [Ga]) \approx 0.27$ was obtained. The temperature was then increased to 525 °C in the second stage, and Cu-Se was co-evaporated. The final Cu content was predetermined by choosing different process duration in stage two. Here, only the thin film with a Cu content of 0.83 exceeded a nominal Cu content of $[Cu]/([In] + [Ga]) > 1$ at the end of the second stage. In stage three finally, In-Ga-Se were co-evaporated at the same temperature until the final Cu content was reached. For more details see Ref. [113], in which a similar process is described.

In the first stage of the Ga series fabrication, the weighting of the corresponding co-evaporation durations of Ga-Se and In-Se was varied in order to achieve different ratios $[Ga]/([In] + [Ga])$. The nominal substrate temperature during this stage was 330 °C. In the second stage, the substrate temperature was increased to nominally 530 °C, and Cu-Se was co-evaporated until the nominal Cu content was $[Cu]/([In] + [Ga]) > 1$. This was followed by an annealing time of 300 s for the In-containing samples and an annealing time of 600 s for the thin film without In. Depending on the final Ga content, In-Se ($CuInSe_2$), Ga-Se ($CuGaSe_2$) or In-Ga-Se ($Cu(In,Ga)Se_2$) were co-evaporated until the thin films exhibited their final Cu content. Only Se was evaporated for 20 minutes during the cooling down.

The $CuInS_2$ absorbers investigated in this work were grown differently. Typically, a Cu-In precursor with slight Cu excess ($[Cu]/([In] + [Ga]) > 1$) is sputtered on Mo coated glass and subsequently annealed in sulfur atmosphere. The sequence of this annealing process starts with a steep temperature ramp, followed by a reaction period of about 2 min at the

maximum temperature of 560 °C, and finally cooling down. This growth process is called rapid thermal process (RTP). Due to the Cu excess, Cu_yS ($1 < y < 2$) forms on top of CuInS_2 , which is etched off by use of potassium cyanide (KCN).

3.2 Transmission electron microscopy

This section introduces the principle of transmission electron microscopy (TEM) and specific imaging techniques therein. The main focus is on electron holography, electron energy-loss spectroscopy and energy-filtered imaging. Inline as well as off-axis electron holography are discussed in the context of electron holography. Finally, the specimen preparation for transmission electron microscopy is addressed.

3.2.1 Basics

In TEM, electrons with a defined kinetic energy are employed in order to analyze specimens or structures on scales that can not be resolved or imaged by visible-light microscopes. There are several imaging techniques in TEM, each one customized to analyze a specific detail of the specimen under investigation. The particle and the wave nature of electrons are considered in order to illustrate the principles of the techniques that have been applied in the present work.

In the particle picture, the general principle of a TEM is the following: Electrons emanating from an electron gun are accelerated to a defined kinetic energy—typically in the range of several hundred keV—and momentum. This will be referred to as electron beam. Guided through ultra high vacuum by a system of magnetic lenses, the electrons penetrate a specimen and interact with it in terms of an exchange of momentum and energy. This process is called scattering.

If the statistical momentum and the energy distribution of the electrons prior to the interaction with the specimen is known, the statistical momentum and energy distribution of the electrons in a plane far away from the specimen, such that the interaction with the specimen in this plane is negligible, contains information about the specimen. In electron energy-loss spectroscopy (EELS) and energy-filtered TEM (EFTEM), the energy distribution of the beam electrons after the interaction with the specimen is investigated in order to obtain information about the local composition, thickness, etc.

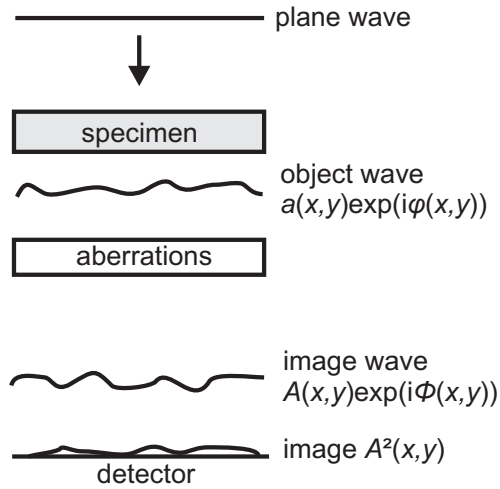


Figure 3.1: Schematic of the imaging principle. The interaction of the incident plane wave with the specimen results in a modulation of the wave which can be described by an object wave $obj(\vec{r})$. Aberrations of the electron lenses lead to an image wave $img(\vec{r})$. The nature of the detector prohibits, however, imaging the phase of the complex image wave.

In the wave nature approach, the electron beam is described by a wavefunction. In this picture, the interaction with the specimen alters the frequency, the amplitude and the phase of the wavefunction. The wavefunction at the exit plane of the specimen then contains valuable information about the specimen. In conventional TEM however, only the intensity distribution is recorded, which is given by the squared modulus of the image wavefunction that arises from the transfer of the exit plane wave (also object wave) function by the microscopic system (see Fig. 3.1). Any additional information which is contained in the phase shift of the wavefunction due to the interaction with the specimen can not be exploited. By means of electron holography, the phase shift of the initial wavefunction—owing to the interaction with the specimen—can be determined and utilized in order to obtain information about local electromagnetic fields within the specimen.

3.2.2 The principle of electron holography

Fig. 3.1 illustrates the basic principle of the imaging principle in TEM with respect to the wave nature of the electrons. In the following it is assumed that the incident electron beam in the vacuum prior to the interaction with the specimen can be described by a plane wave $\psi_0(\vec{r}_{3d}, t) = a_0 \exp(i(2\pi\vec{k}_0\vec{r}_{3d} - \omega_0 t + \varphi_0))$, with amplitude a_0 , space vector $\vec{r}_{3d} = (x, y, z)$,

wave vector $\vec{k}_0 = (0, 0, |\vec{k}_0|)$, time t , angular frequency ω_0 , and phase φ_0 . Without loss of generality, the amplitude may be set to $a_0 = 1$ and the phase to $\varphi_0 = 0$. Due to a local exchange of momentum and energy with the specimen, the wavefunction at the exit plane of the specimen can not be described by a plane wave anymore. However, a part of the wavefunction does not exchange energy nor momentum with the specimen. This part can be described by $\psi_f(\vec{r}, t) = a(\vec{r}) \exp(i(2\pi\vec{k}_0\vec{r}_{3d} - \omega_0 t + \varphi(\vec{r})))$, with modulated amplitude $a(\vec{r})$ and modulated phase $\varphi(\vec{r})$, both depending on the spatial coordinates within the exit plane $\vec{r} = (x, y)$. In the following, \vec{r} is applied as the two-dimensional spatial coordinate within all planes perpendicular to the propagation direction of the electron beam, i.e., within planes with a constant z value. ψ can now be expressed by

$$\psi_f(\vec{r}_{3d}, t) = obj(\vec{r})\psi_0(\vec{r}_{3d}, t), \quad (3.1)$$

with the object wave

$$obj(\vec{r}) = a(\vec{r}) \exp(i\varphi(\vec{r})). \quad (3.2)$$

The amplitude of the incident plane wave is modified, since a part of the wave exchanges energy and momentum with the specimen. The phase of the incident plane wave is affected by the interaction with the specimen because the wavelength of the wavefunction depends on the local Coulomb and vector potentials within the specimen. Disregarding the magnetic flux, the local wavelength of the wavefunction is given by [114]

$$\lambda = \frac{1}{|\vec{k}|} = \frac{h}{\sqrt{2m_0e(U + V)(1 + \frac{e(U+V)}{2m_0c^2})}}, \quad (3.3)$$

with Planck's constant h , the electron's rest mass m_0 and charge e , the acceleration voltage U of the transmission electron microscope, and the electrostatic potential V which the electrons from the incident beam experience while traveling through the specimen. V contains contributions from scattering atoms (or ions) of the sample as well as from free charge carriers and any other electrical potentials.

If the specimen is assumed to be a pure phase object, i.e., the interaction of the wavefunction with the specimen affects only the phase, one can apply the phase object approximation (POA). The POA is a good approximation for electrons with high kinetic energy traveling through thin specimens that are not oriented along a low index zone axis with

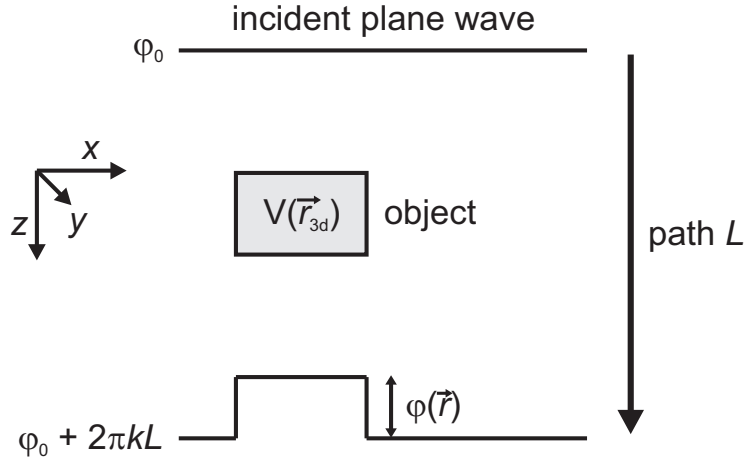


Figure 3.2: Objects with electrostatic potential $V(\vec{r}_{3d})$ induce a phase shift $\varphi(\vec{r})$ in the object wave $obj(\vec{r})$ with respect to the wave that traveled through vacuum.

respect to the beam. It is further assumed that the total wavefunction of the specimen and the electron beam can be written as a product of the individual wavefunctions due to the distinguishability of the electrons bound in the solid and the high energy beam electrons [115]. The change in phase $\varphi(\vec{r})$ at the exit plane due to the electrostatic potential $V(\vec{r}_{3d})$ within the specimen, which is assumed to be small compared with the kinetic energy of the beam electrons, is then given by [114]

$$\varphi(\vec{r}) = \int_{\text{path}} 2\pi \vec{k} d\vec{s} = \sigma(U) \int_{\text{path}} V(\vec{r}_{3d}) dz = \sigma(U) d(\vec{r}) V_a(\vec{r}). \quad (3.4)$$

$d(\vec{r})$ is the local specimen thickness, $V_a(\vec{r})$ the electrostatic potential within the specimen averaged along the path of the incident plane wave through the specimen, i.e., along the z axis perpendicular to the specimen surface. $\sigma(U) = 2\pi em/h^2k_0$ is an acceleration voltage dependent interaction constant, where m is the relativistic electron mass. The change in phase caused by an object with electrostatic potential $V(\vec{r}_{3d})$ is illustrated in Fig. 3.2. A modulation of the local amplitude of the object wave can be included by adding an imaginary phase shift $iM(\vec{r})$. In the framework of the POA, it is therefore possible to retrieve the local electrostatic potential $V_a(\vec{r})$, if the phase $\varphi(\vec{r})$ and the local specimen thickness $d(\vec{r})$ are known.

The imaging system transfers the object function $obj(\vec{r})$ to the image plane of the microscopic system. Due to aberrations of the objective lens, the image wave $img(\vec{r})$ at the

image plane of the objective lens differs from the object wave and may be expressed by

$$img(\vec{r}) = \text{FT}^{-1} [\text{FT}[obj(\vec{r})] \text{WTF}(\vec{q})] = A(\vec{r}) \exp(i\Phi(\vec{r})), \quad (3.5)$$

where FT denotes the Fourier transform, $\text{WTF}(\vec{q})$ is the wave transfer function depending on the two-dimensional spatial frequencies \vec{q} , and A and $\Phi(\vec{r})$ are amplitude and phase of $img(\vec{r})$. The wave transfer function is given by

$$\text{WTF}(\vec{q}) = E^{\text{ap}}(\vec{q}) E^{\text{sc}}(\vec{q}) E^{\text{tc}}(\vec{q}) \exp(-i\chi(\vec{q}, \Delta f)), \quad (3.6)$$

where $\chi(\vec{q})$ is the wave aberration function which describes the transfer of spatial frequencies \vec{q} by the objective lens, even if the incident electron beam is perfectly coherent. It contains contributions from defocus Δf , spherical aberration, astigmatism, axial coma etc. (for details, see Appendix A). $E^{\text{sc}}(\vec{q})$ and $E^{\text{tc}}(\vec{q})$ are damping envelope functions arising from imperfect spatial and temporal coherence of the illumination, i.e., partial coherence, and $E^{\text{ap}}(\vec{q})$ is an aperture function cutting off spatial frequencies larger than a defined value (see also Appendix A for details).

In conventional TEM, only the squared modulus $|img(\vec{r})|^2 = A^2(\vec{r})$ of this function is recorded by a CCD camera. Electron holography opens up the possibility of retrieving the information about the specimen which is contained in the phase $\Phi(\vec{r})$. The object function $obj(\vec{r})$ can be reconstructed from the image wave if the aberrations of the objective lens and distortions introduced by the projective lenses are known. The principle idea of electron holography in TEM is to bring the image wave and a coherent wave to interference. The imaged interference pattern is called hologram and contains information about the phase $\Phi(\vec{r})$ and the amplitude $A(\vec{r})$ of the image wave. This approach was proposed by Gabor already in 1948 [116]. In general, there are a number of ways to realize the interference, for a review, see Ref. [117]. In this work, bright-field off-axis and bright-field inline electron holography were applied in order to study the local electrostatic (Coulomb) potential at grain boundaries within polycrystalline Cu(In,Ga)Se₂ and CuInS₂ thin films. For a comparison of inline and off-axis electron holography, see Refs. [118, 119]

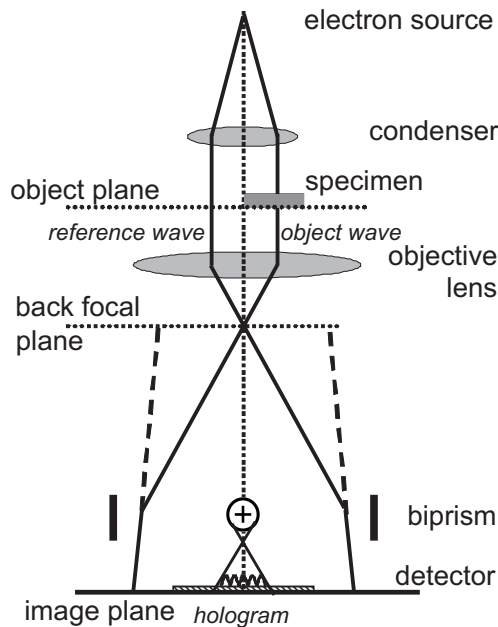


Figure 3.3: Schematic of the principle of off-axis electron holography after [120]. The specimen is placed into the optical path, such that part of the incident electron beam penetrates the specimen, while the other part is employed as reference wave. A positively charged biprism between the back focal plane and the image plane of the objective lens deflects object and reference wave, superimposing them in the image plane. The resulting interference pattern is called electron hologram.

3.2.3 Off-axis electron holography

Fig. 3.3 illustrates the principle idea of off-axis electron holography. The specimen under investigation is placed under the electron beam, such that part of the incident electron wave penetrates the specimen and part of the electron wave travels through a nearby hole in the specimen, i.e., through vacuum, and does not interact with the specimen. The latter part is used as reference wave which is coherent with the object wave. Object wave and reference wave are imaged by the objective lens and then brought to an overlap by a positively charged wire in the optical path between the back focal plane and the image plane of the objective lens. The wire is called biprism and was invented by Möllenstedt et al. in 1956 [121]. A hologram forms in the image plane of the microscope in a region where both waves overlap. By setting the amplitude of the reference wave image $A_r = 1$, the intensity distribution of the hologram, which is detected by a camera, is given by [120, 122]

$$I_{\text{holo}}(\vec{r}) = 1 + I_{\text{elast}}(\vec{r}) + I_{\text{inelast}}(\vec{r}) + 2\mu A(\vec{r}) \cos(2\pi\vec{q}_c \cdot \vec{r} + \Phi(\vec{r}) + \gamma(\vec{r})). \quad (3.7)$$

$|\vec{q}_c| = |\vec{k}_0|/\beta$ is the carrier frequency of the interference fringes, where β denotes the overlapping angle between the image wave and the image of the reference wave. μ is the contrast of the fringes. It depends on the degree of spatial and temporal coherence, as well as inelastic scattering, any instabilities, and the modulation transfer function of the camera [123]. These contributions can not be neglected in microscopy. $I_{\text{elast}}(\vec{r})$ represents the intensity caused by elastically scattered electrons and $I_{\text{inelast}}(\vec{r})$ represents the intensity caused by inelastic scattered electrons having lost energy of equal to or larger than about 10^{-15} eV [124]. The position dependent phase shift $\gamma(\vec{r})$ describes distortions introduced by the projective lens system, the biprism, and the recording device. In order to correct for the phase shift $\gamma(\vec{r})$ during the reconstruction of the object wave, an empty hologram, i.e., a hologram of a vacuum region acquired under the same imaging conditions, is required. The image intensity of such an empty hologram is given by

$$I_{\text{empty}}(\vec{r}) = 2 + 2\mu \cos(2\pi\vec{q}_c \cdot \vec{r} + \gamma(\vec{r})). \quad (3.8)$$

The amplitude $A(\vec{r})$ and the phase $\Phi(\vec{r})$ of the image wave can be retrieved from the intensity distributions $I_{\text{holo}}(\vec{r})$ and $I_{\text{empty}}(\vec{r})$. In a first step, $I_{\text{holo}}(\vec{r})$ is Fourier transformed leading to

$$\begin{aligned} \text{FT}[I_{\text{holo}}(\vec{r})] = & \\ & \text{FT}[1 + I_{\text{elast}}(\vec{r}) + I_{\text{inelast}}(\vec{r})] && \text{centerband} \\ & + \mu \text{FT}[A(\vec{r}) \exp(i(\Phi(\vec{r}) + \gamma(\vec{r})))] * \delta(\vec{q} - \vec{q}_c) && \text{sideband } +1 \\ & + \mu \text{FT}[A(\vec{r}) \exp(-i(\Phi(\vec{r}) + \gamma(\vec{r})))] * \delta(\vec{q} + \vec{q}_c) && \text{sideband } -1. \end{aligned} \quad (3.9)$$

The Fourier transform consists of one centerband, and two sidebands (+1 and -1). The centerband essentially represents the diffractogram of a conventional electron micrograph and contains contributions from elastically and inelastically scattered electrons. The sidebands are spatially separated from the centerband in Fourier space by the vector $\pm\vec{q}_c$ and represent the complex (+1) and complex conjugate (-1) diffraction pattern of the image wave with damped contrast μ . Note that the phase and amplitude of both sidebands are

linearly related to the object wave.

In a second step, a mask is placed around the sideband (+1) and the resulting diffraction pattern is centered with respect to \vec{q}_c . The inverse Fourier transform of this diffraction pattern results in the reconstructed image wave

$$img_{\text{rec}}(\vec{r}) = \mu A(\vec{r}) \exp(i(\Phi(\vec{r}) + \gamma(\vec{r}))). \quad (3.10)$$

If the same procedure is applied on the empty hologram, see Eq. (3.8), this yields

$$img_{\text{empty}}(\vec{r}) = \mu \exp(i\gamma(\vec{r})). \quad (3.11)$$

The image wave $img'(\vec{r})$ can now be obtained by dividing the reconstructed image wave $img_{\text{rec}}(\vec{r})$ by the image wave of the empty hologram $img_{\text{empty}}(\vec{r})$

$$img'(\vec{r}) = \frac{img_{\text{rec}}(\vec{r})}{img_{\text{empty}}(\vec{r})} = A(\vec{r}) \exp(i\Phi(\vec{r})). \quad (3.12)$$

In principle, the recorded object wave $obj'_{\text{rec}}(\vec{r})$ can be retrieved from $img'(\vec{r})$ by inverting Eq. (3.5) if the WTF of the objective lens is known

$$obj'_{\text{rec}}(\vec{r}) = \text{FT}^{-1} \left[\frac{\text{FT}[img'(\vec{r})]}{\text{WTF}(\vec{r})} \right]. \quad (3.13)$$

However, it is a challenging task to determine the aberration coefficients and to actually perform the reconstruction since it involves numerical image processing. In addition, special care has to be taken in the consideration of the incident wave, which is generally not a plane wave. It has been shown (for elliptical illumination) that this can be corrected by adding a phase curvature, modeling the shape of the incident wave front, to the image phase Φ prior to the reconstruction described by Eq. (3.13) and then by subtracting the same curvature from the phase of $obj'_{\text{rec}}(\vec{r})$ [125]. This procedure yields

$$obj_{\text{rec}}(\vec{r}) = obj(\vec{r}).$$

The total coherent current is an optical invariant. Elliptical illumination is applied in order to achieve a high spatial coherence in the direction perpendicular to the biprism and the z axis, whereas the spatial coherence in the normal direction is reduced. In principle, this high spatial coherence in one direction makes it possible to image phase relations on

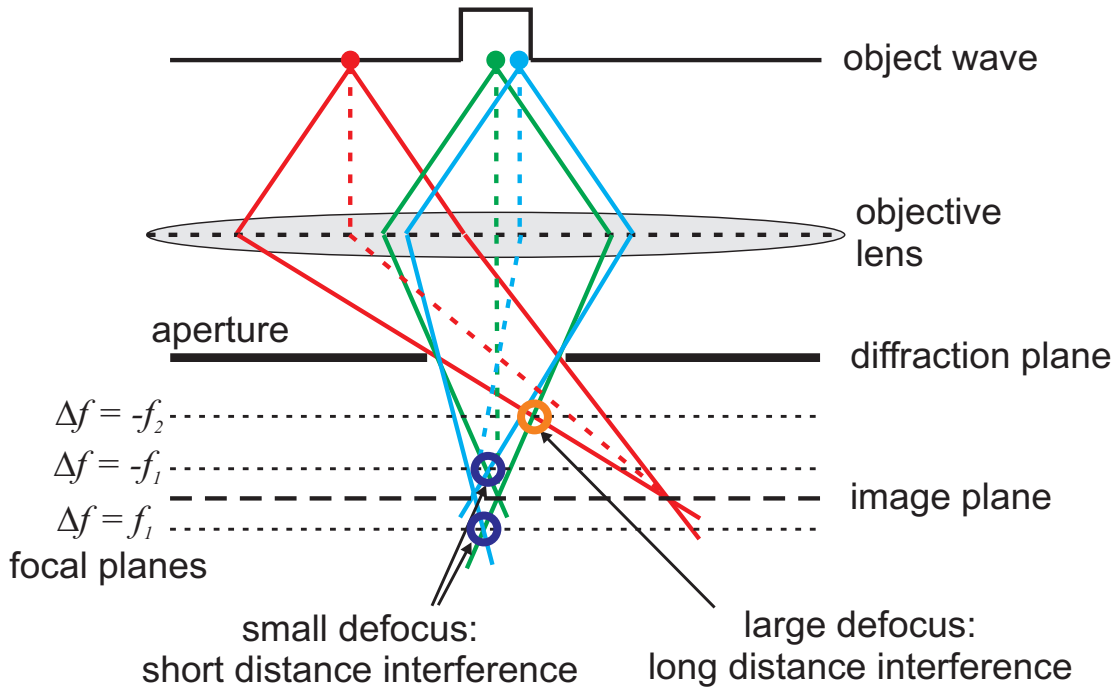


Figure 3.4: Schematics of the principle of inline electron holography. Different parts of the object wave interfere at different focal planes Δf . At large defocus ($\Delta f = -f_2$), waves with large distances in the object wave interfere. This is highlighted by the orange circle. At small defocus, waves with small distances in the object wave interfere ($\Delta f = \pm f_1$). This is highlighted by the dark blue circles. The illustration is based on a schematic provided by C. T. Koch, Max Planck Institute for Metals Research, Stuttgart, Germany.

distances larger than about 100 nm. It should be noted that the smallest detectable phase difference $\delta\Phi_{min}$ is given by [126, 127]

$$\delta\Phi_{min} = \frac{SNR}{\mu} \sqrt{\frac{2}{N \cdot DQE}},$$

with a signal/noise ration SNR , the number N of detected electrons per resolved pixel and the detection quantum efficiency DQE of the applied charged-coupled device (CCD) camera.

3.2.4 Inline electron holography

In contrast to off-axis electron holography, there is no external coherent reference wave employed in inline electron holography to provoke an interference with the object wave.

Instead, the object wave is its own reference wave. In general, a set of minimum three images, for which at least one parameter of the imaging system is varied, is required in order to reconstruct the object wave $obj(\vec{r})$ unambiguously [128]. For this work, the focus, i.e., the objective lens current, was varied. The principle of interference is illustrated in Fig. 3.4. In a very similar method, the image contrast at different defoci is investigated in order to obtain information about the object wave phase. This method is named Fresnel contrast analysis and has previously been applied by other groups [129–133] to study various interfaces in solids.

Off-axis electron holography is considered as linear imaging, since only linear equations are involved in the reconstruction of the object wave. In the more general case of nonlinear imaging, the impact of imperfect spatial and temporal coherence on the image intensity can not be described by use of the damping envelope functions $E^{sc}(\vec{q})$ and $E^{tc}(\vec{q})$ anymore, but requires the concept of the transmission cross coefficient (TCC) [134]. The image intensity of a conventional TEM image is given by

$$I(\vec{r}) = \text{FT}^{-1} \left[\int_{-\infty}^{+\infty} obj(\vec{q}') \text{TCC}(\vec{q}', \vec{q}'') obj^*(\vec{q}'') d^2\vec{q}'' \right], \quad (3.14)$$

where $obj(\vec{q})$ is the Fourier transform of the object wave $obj(\vec{r})$, $\vec{q}' = \vec{q} + \vec{q}''$, and $*$ denotes the complex conjugate. The TCC is given in Appendix B.

If astigmatismus, third and higher order aberrations are neglected, and perfect temporal coherence is assumed, the TCC may be approximated by [134] (see also Appendix B)

$$\begin{aligned} \text{TCC}(q', q'') &= \exp(-(\pi\theta_{coh}\Delta f q)^2) \\ &\times \exp(-i(\chi(q', \Delta f) - \chi(q'', \Delta f))), \end{aligned} \quad (3.15)$$

where θ_{coh} is the illumination aperture half width (convergence half-angle). The integral over $d^2\vec{q}''$ in Eq. (3.14) then yields [135]

$$I(\vec{r}) = |img_{\Delta f}(\vec{r})|^2 * \text{FT}^{-1} [\exp(-(\pi\theta_{coh}\Delta f q)^2)], \quad (3.16)$$

with the image wave at the focal plane with defocus Δf

$$img_{\Delta f}(\vec{r}) = \text{FT}^{-1} [obj(\vec{q}) \exp(-i\chi(q, \Delta f))]. \quad (3.17)$$

In principle, this simplification is applicable for aberration-corrected microscopes or if a

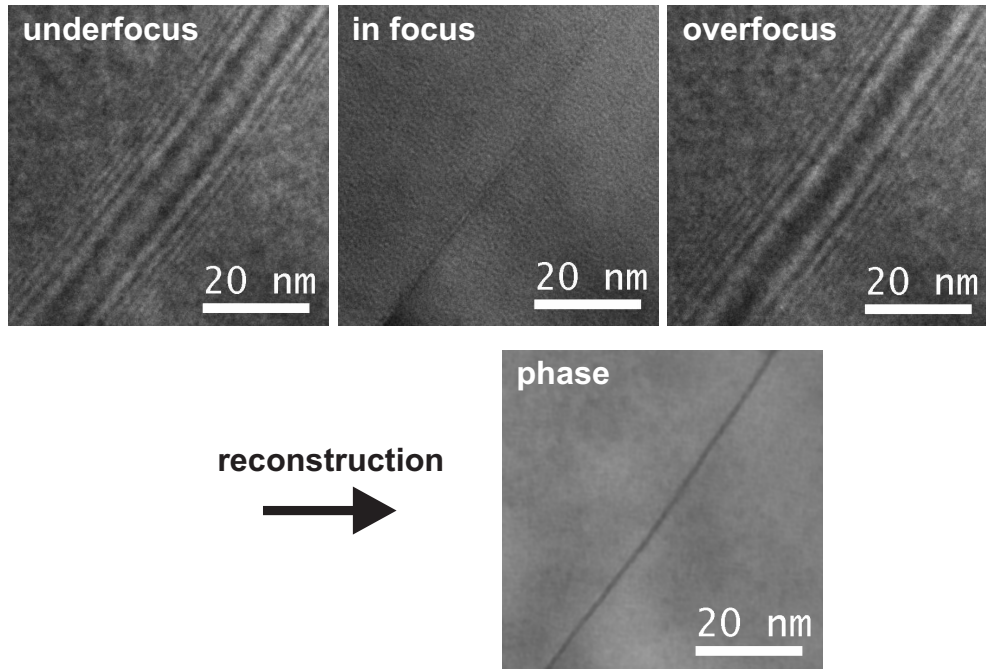


Figure 3.5: Three bright-field TEM images of a grain boundary within a CuInS₂ thin film, which were acquired at different focus ($\Delta f \approx -5690$ nm (underfocus), $\Delta f \approx 70$ nm ("in focus"), $\Delta f \approx 6050$ nm (overfocus)), and the reconstructed relative phase difference $\Delta\varphi(\vec{r})$ displayed as a gray-value image. The three acquired images are part of the through focal series which is the starting point of the reconstruction of the object wave. Fresnel fringes form on either side of the grain boundary due to an interference of parts of the object wave owing to an abrupt change of the local averaged electrostatic potential.

sufficiently small objective aperture is used during imaging. It is worth noting that the total flux, i.e., the integral image intensity for a given electron current density, is conserved since there are no damping envelope functions applied in this description cutting away high spatial frequencies of the object wave.

For the present work, through focal series, i.e., series of N images with varying defocus, served as a starting point of the reconstruction process of the phase images which is based on an algorithm developed by Koch [135] and Bhattacharyya et al. [136]. A number $N > 3$ is typically chosen since images with small and large defocus are required for an optimized transfer of the phase information. In images with small defocus, higher spatial frequencies are transferred by Eq. (3.16) than in images with large defocus since the damping of high spatial frequencies by the last term is smaller (see also Fig. 3.4). Images with high defocus contain information on large distance interference, see Fig. 3.4, and are therefore required

to retrieve low spatial frequencies. Moreover, a small defocus step between the images of the through-focal series facilitates the image alignment.

For objects in the specimen that affect the phase of the object wave abruptly, such as grain boundaries in CuInSe₂, a varying focus results in Fresnel fringes in the recorded images originating from interference of different parts of the object wave, see Fig. 3.4 and Fig. 3.5. This interference is employed in order to reconstruct gray-value images of the phase $\varphi(\vec{r})$ in the object wave. The iterative reconstruction process starts with a guess of the object wave, typically $\varphi(\vec{r}) = 0$, and a the square root of the image with smallest defocus, and involves the following iteration steps:

1. By use of Eq. (3.17), the current estimate of the object wave is propagated to each of the N focal planes with defocus Δf_n . n ($1 \leq n \leq N$) denotes a specific plane.
2. A new estimate of the image wave in each plane with defocus Δf_n is obtained by comparing the simulated intensity with the experimental one. For the simulated and experimental image wave

$$I_{\Delta f_n}^{\text{sim/exp}}(\vec{r}) = |img_{\Delta f_n}^{\text{sim/exp}}(\vec{r})|^2 * \text{FT}^{-1} [\exp(-(\pi\theta_{\text{coh}}\Delta f q)^2)], \quad (3.18)$$

the difference of their amplitude

$$\text{dim}g_{\Delta f_n}(\vec{r}) = \sqrt{I_{\Delta f_n}^{\text{exp}}(\vec{r})} - \sqrt{I_{\Delta f_n}^{\text{sim}}(\vec{r})}, \quad (3.19)$$

is used to update the amplitude of the current image wave to

$$img'_{\Delta f_n}(\vec{r}) = [|img_{\Delta f_n}(\vec{r})| + \text{dim}g_{\Delta f_n}(\vec{r})] img_{\Delta f_n}(\vec{r}) / |img_{\Delta f_n}(\vec{r})|. \quad (3.20)$$

3. A new estimate of the object wave is obtained by back propagation of the image waves $img'_{\Delta f_n}(\vec{r})$ by inverting Eq. (3.17) and a subsequent weighted averaging of the corresponding object waves. In Fourier space, the weighting is performed by a multiplication with $\exp(-(\pi\theta_{\text{coh}}\Delta f q)^2)$ [136].

The steps described above are executed within a loop until a preassigned convergence criterion is reached.

In transmission electron microscopes, a change in the objective lens current does not only cause a defocus Δf but also image distortions, such as a change of magnification and image rotations. This and additional image drift necessitate proper image correction as well as image alignment, which is implemented in the reconstruction algorithm that has been applied in the present work [135]. Although not included in this overview, the spherical aberration (C_s) is also considered within the wave aberration function $\chi(q, \Delta f)$. An additional low-pass filter may be applied on the images prior to the reconstruction in order to damp noise. The exact defocus of each image and the convergence angle are determined during the computational reconstruction, where the simulated images are fitted to the experimental ones.

The maximum distances for which changes in the phase can be retrieved, i.e., the effective coherence length of the method is determined by the maximum applied defocus value (see Fig. 3.4). A rough estimate is obtained by measuring the width of the Fresnel fringes (see Fig. 3.5), which appear in the TEM image on either side of a feature within the specimen that exhibits a strong change in the local Coulomb potential, at the highest applied defocus values. For defocus values of about $10\text{ }\mu\text{m}$ as applied in this thesis, this can be estimated to be about 20 nm .

It is generally not possible to retrieve the absolute phase $\varphi(\vec{r})$ of the object wave with respect to the incident plane wave. The determination of the absolute phase is only possible if part of the phase image resembles the (object wave) phase of a vacuum region in a nearby hole and if there is no abrupt phase shift of more than 2π at the specimen vacuum interface. Instead, the phase shift at an arbitrary position r_{zero} is chosen as zero point and the phase shift at other positions r is then expressed as the relative phase shift $\Delta\varphi(\vec{r})$ with respect to the zero point. However, this drawback is an advantage at the same time, for specimen positions far away from vacuum regions, i.e., holes within the specimen, can be studied.

3.2.5 Application of inline and off-axis electron holography

Regarding electron holography, the present work aims at revealing the electrostatic potential at grain boundaries within polycrystalline $\text{Cu}(\text{In},\text{Ga})\text{Se}_2$ and CuInS_2 thin films. This information is contained in the phase $\varphi(\vec{r})$ of the object wave (see Eq. (3.4)). In order to retrieve the phase $\varphi(\vec{r})$, off-axis holograms were acquired by use of a Philips CM200FEG (ST/Lorentz) TEM at the Triebenberg laboratory of the Technical University Dresden,

operated by John Sandino. Low resolution in Lorentz mode, as well as medium resolution holographic imaging were applied. Elliptic illumination [137] with a higher degree of coherence in direction perpendicular to the biprism filament was used in all cases. The reconstruction of the image wave $img_{rec}(\vec{r})$ from the holograms was achieved with the procedure described in Sec. 3.2.3 (for more details, see Ref. [120, 123]).

The reconstruction of the relative phase differences $\Delta\varphi(\vec{r})$ in the object wave determined by use of inline electron holography was based on the acquisition of a through focal series with a set of 15 images by use of a Zeiss LIBRA 200FE TEM. A nominal defocus step of 800 – 1200 nm between the individual images was adjusted. The actual defocus steps were fitted during the computational reconstruction of the object wave. Inelastically scattered electrons were filtered out by a 10 eV wide energy-selecting slit placed on the zero-loss region in the energy dispersive plane of the electron spectrometer. An objective aperture with radius of about 1.2 nm^{-1} was applied in order to satisfy the conditions of the reconstruction algorithm (see Sec. 3.2.4 for details). A low-pass filter of the same size in Fourier space was applied on the acquired images of the through focal series before the reconstruction, to filter out noise. A magnification of ~ 135000 was typically chosen for the acquisition of the through focal series. Illumination angles (illumination apertures) smaller than nominally $50 \mu\text{rad}$ were chosen for the acquisition of the through focal series. These illumination angles emerged as an optimum considering the tradeoff between the highest possible degree of coherence of the incident electron beam and a reasonable signal to noise ratio of the images. As consequence, this also kept the generation of free charge carriers within the semiconductors by the electron beam as low as possible. This issue will be addressed in Sec. 4.2.1.1. The computational reconstruction of the object wave was performed by the procedure described in Sec. 3.2.4.

The sensitivity of this method to the microscope parameters was tested by varying the objective aperture size, as well as the defocus step size, and the energy width of the energy-selecting slit which was employed for the energy filtering. No significant dependencies of the retrieved object wave on these parameters were found.

Crystal orientations along low index zone axes were avoided for inline and off-axis electron holography. It is therefore assumed that the influence of dynamical scattering on the object wave phase and the mean inelastic path is negligible [138], and the POA is applicable for all object wave phases that have been determined during this work.

The grain boundaries that have been investigated during this work were tilted edge-on

as accurately as possible, i.e., such that the plane of the grain boundary was parallel to the incident direction of the electron beam. The smallest extension of the bright field contrast perpendicular to the plane of the grain boundary was an indication for the best possible edge-on tilt. At large defocus, symmetric Fresnel fringes on both sides of the grain boundary served as additional indicator for an accurate edge-on tilting of the grain boundaries (see Fig. 3.5).

3.2.6 Determination of the averaged electrostatic potential

Ferromagnetic properties of Cu(In,Ga)Se₂ and CuInS₂ are not known, which is why the magnetic flux in the TEM specimens during the measurements is neglected in the following. If the POA is applicable, the phase shift $\varphi(\vec{r})$ in the object wave $obj(\vec{r})$ is in a good approximation proportional to the electrostatic potential averaged along the local path of the electron wave through the specimen $V_a(\vec{r})$ (see Eq. (3.4)). This averaged electrostatic potential originates from the Coulomb potential of the atomic nuclei and of the electrons within the sample as well as any additional external electrostatic potential. In a neutral solid without any charge accumulations and negligible external electric fields, the mean value of the averaged electrostatic potential $V_a(\vec{r})$ is the so called mean inner potential (MIP). The MIP can be expressed as [139]

$$\text{MIP} = \frac{1}{vol} \int_{vol} V(\vec{r}_{3d}) d^3r, \quad (3.21)$$

with the volume of the specimen vol , and the electrostatic potential within the specimen $V(\vec{r}_{3d})$. vol may also be a more localized volume, e.g. the local unit cell volume. The zero point of the electric potential is typically chosen far away from the specimen within the vacuum in the TEM column. The atomic potential—not to be confused with potential energy—and hence the MIP are always positive resulting in beam electrons having a larger kinetic energy inside the specimen. In the following, it is assumed that the measured quantity $V_a(\vec{r})$ is a superposition of the local MIP(\vec{r}) and the potential $\Delta V_{cr}(\vec{r})$ that arises from local redistributions of the free charge carriers within the investigated semiconductors and external electric fields [140]

$$V_a(\vec{r}) = \text{MIP}(\vec{r}) + \Delta V_{cr}(\vec{r}). \quad (3.22)$$

This relationship is applicable if the potential which is caused by locally redistributed free charge carriers is a small perturbation of the potential caused by the total charge distribution, including atomic charges, i.e., $\Delta V_{\text{cr}} \ll \text{MIP}$. This leads to the fundamental equation

$$\Delta V_a(\vec{r}) = \Delta \text{MIP}(\vec{r}) + \Delta V_{\text{cr}}(\vec{r}), \quad (3.23)$$

i.e., local changes $\Delta V_a(\vec{r})$ in the averaged electrostatic potential are induced by a superposition of local changes $\Delta \text{MIP}(\vec{r})$ in the MIP and local changes in the potential $\Delta V_{\text{cr}}(\vec{r})$ generated by a redistribution of free charge carriers.

The general procedure of retrieving the averaged electrostatic potential $V_a(\vec{r})$ or differences $\Delta V_a(\vec{r})$ of a region of interest—including grain boundaries within the specimen—was as follows: From the gray-value images of the phase shift $\varphi(\vec{r})$ or the relative phase difference $\Delta\varphi(\vec{r})$ obtained by use of electron holography in TEM (see Sec. 3.2 for details about image acquisition and phase reconstruction), profiles were extracted across features in the phase images that were correlated with grain boundaries. In favor of better statistics, 50 – 100 individual profiles extracted perpendicular to the grain boundary were averaged. The local specimen thickness $d(\vec{r})$ along the profiles was determined by the use of EFTEM and Eq. (3.26), for which the mean free path λ_{mfp} was calculated according to Ref. [141]. The averaged electrostatic potential was then calculated by rewriting Eq. (3.4)

$$V_a(\vec{r}) = \frac{\varphi(\vec{r})}{\sigma(U)d(\vec{r})}. \quad (3.24)$$

In the case of CuInS₂, the procedure is exemplarily illustrated in Fig. 3.6. The averaged electrostatic potentials in the grain interiors, several nm away from the grain boundary cores, were chosen as zero points of $\Delta V_a(\vec{r})$.

If the grain boundaries appear as lines in the phase images with lengths much larger than the regions of interest used for the extraction of $\Delta V_a(\vec{r})$, and if the MIP is assumed to be constant in the region of interest, the charge distribution perpendicular to this line $\rho(x)$ can be calculated from $\Delta V_a(\vec{x})$ by use of Poisson's equation (for constant permittivity ϵ)

$$\frac{\partial^2 \Delta V_a(x)}{\partial x^2} = -\frac{\rho(x)}{\epsilon}, \quad (3.25)$$

with x being the spatial coordinate perpendicular to the line, and $\epsilon = \epsilon_0 \epsilon_r$ being the

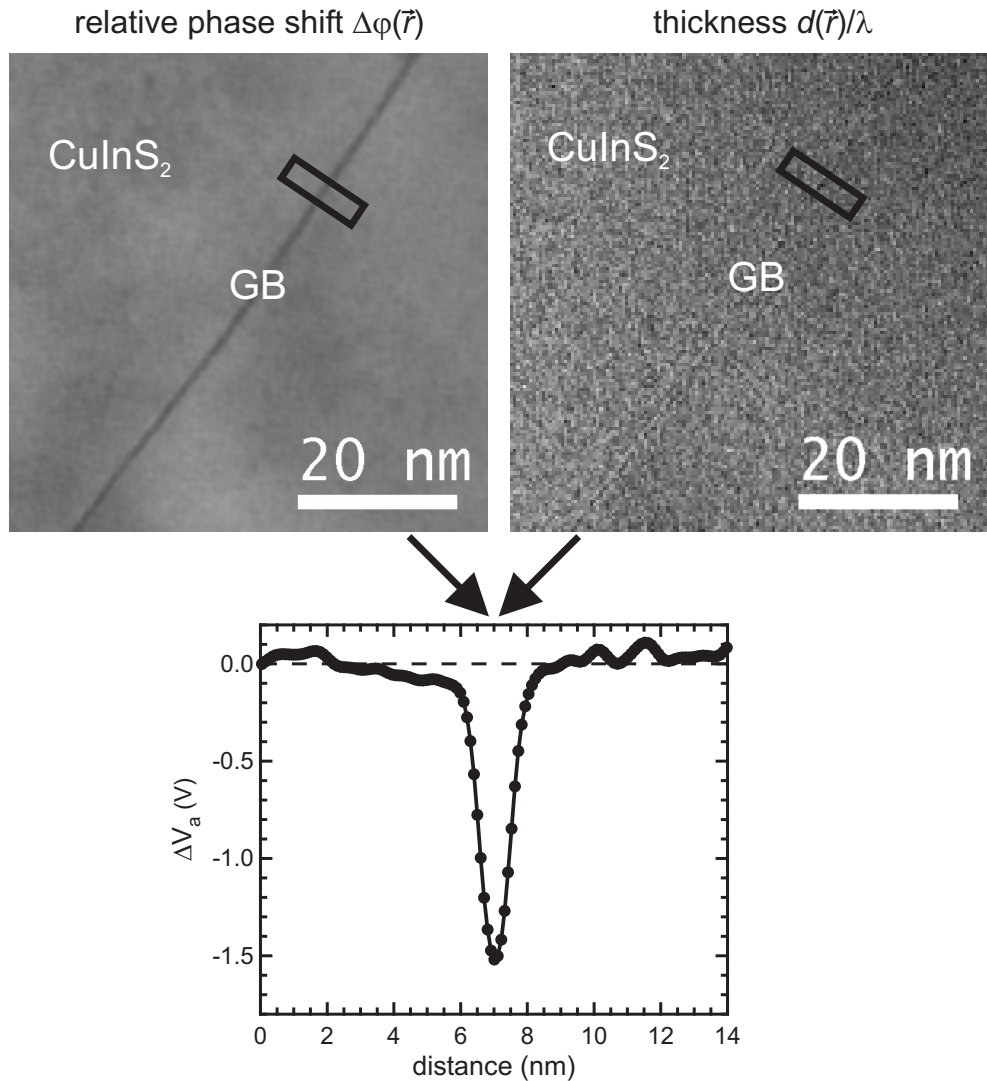


Figure 3.6: Illustration of the determination of differences in the averaged electrostatic potential $\Delta V_a(\vec{r})$, using the example of the same grain boundary (GB) within CuInS_2 as in Fig. 3.5. Individual profiles are extracted across features in the gray-value images of the relative phase shift $\Delta\varphi(\vec{r})$ and of the local specimen thickness $d(\vec{r})/\lambda$. Typically, 50–100 individual profiles contained in the black frame are averaged parallel to the feature correlated with the grain boundary. Differences in the averaged electrostatic potential $\Delta V_a(\vec{r})$ are then calculated by use of Eq. (3.24). The potential in the grain interior, several nm away from the grain boundary core, was chosen as zero point.

permittivity of the material consisting of the vacuum permittivity ϵ_0 and the relative permittivity ϵ_r .

Since the focus of this thesis is on random grain boundaries in polycrystalline thin film

solar cell absorbers, the presented results—unless mentioned otherwise—were measured on random grain boundaries with no highly symmetric configuration with respect to the orientation of the adjacent crystal lattices as well as to the shape of the interfacial area. It was assumed that the atomic configuration at the interface can not be highly symmetric if the interfacial areas of grain boundaries are curved. Since grain boundaries may exhibit a contrast in bright-field TEM images, grain boundaries with non highly symmetric interfaces were identified by a curvature of their contrast in the bright-field TEM images.

3.2.7 Electron energy-loss spectroscopy and energy-filtered imaging

The double-differential cross section $d^2\sigma/d\Omega dE$ describes the angular distribution of the beam electrons after the interaction with the specimen as a function of their energy-loss. This distribution depends strongly on the elements and the bond types within the specimen and is a fingerprint of the material or compound under investigation. In electron energy-loss spectroscopy (EELS) and energy-filtered transmission electron microscopy (EFTEM), the energy distribution of the beam electrons within a defined solid angle—after interaction with a specimen—is exploited to analyze the specimen. The measured quantity in EELS and EFTEM is the electron intensity as a function of sample position and energy-loss $I(x, y, \Delta E)$ (sometimes also of scattering angles and energy-loss $I(\phi, \theta, \Delta E)$). For an overview of the techniques, see Refs. [142–144].

In order to study the local composition at and in the vicinity of grain boundaries, EELS was performed in the scanning mode of the transmission electron microscope (STEM). Spectral images, i.e., energy-loss spectra acquired at several points within a region of interest with respect to the specimen surface, served as starting point of the compositional analysis. Only the information contained in the Cu-L_{2,3} (onset at 928 eV), the In-M_{4,5} (onset at 447 eV), and the Se-L_{2,3} (onset at 1441 eV) core-loss edges within the acquired spectra could be quantitatively evaluated [145]. An evaluation of the Ga-L_{2,3} (onset at 1113.5 eV) and the Na-K (onset at 1075 eV) core-loss edges was not possible due to overlaps with the Cu-L_{2,3} edge. If necessary, the spectra were corrected for multiple scattering effects by use of the Fourier-log method [142]. A principle component analysis (PCA) [146] was employed on the acquired spectra to reduce their noise level. The energy-loss background in the resulting spectra was then fitted in a region of interest at energies smaller than the

onset of the core-loss edges by use of a power law model and then subtracted from the spectrum, in order to obtain the element-specific intensity of the core-loss edges. The sum of the intensity (net counts) in a selected energy interval after the onset of the edges is the measure for the detection of compositional changes within a region of interest.

The determination of the averaged electrostatic potential within the specimen via the phase $\varphi(\vec{r})$ requires knowledge about the local specimen thickness $d(\vec{r})$. For that purpose, a zero-loss ($\Delta E = 0$) filtered image, for which only unscattered or quasi-elastically scattered electrons contribute, containing the region of interest, and an additional unfiltered image from the same position were acquired. Assuming that the number of scattering events per electron follows a Poisson distribution, the local specimen thickness $d(\vec{r})$ can be calculated according to Egerton [142] by

$$d(\vec{r}) = \lambda_{\text{mfp}} \ln(I_u(\vec{r})/I_0(\vec{r})), \quad (3.26)$$

where λ_{mfp} is the inelastic mean free path of the beam electrons in the specimen for a given collection angle of the spectrometer, $I_u(\vec{r})$ is the intensity distribution of the unfiltered image, and $I_0(\vec{r})$ is the intensity distribution of the zero-loss filtered image. If the collection angle of the spectrometer is known, the inelastic mean free path λ_{mfp} can be calculated by use of the Kramers-Kronig sum rule to an accuracy of within 10 % or 2 nm, whichever is larger [141].

3.2.7.1 Application of EELS and EFTEM

Due to strong contamination of the specimen surfaces with C and Si, EELS measurements by use of the Zeiss LIBRA 200FE yielded no relevant data. The microscope which was employed to determine the data shown in the present thesis was a C_s corrected NION Ultra-STEM with a Gatan ENFINA electron spectrometer at the SuperSTEM, STFC Daresbury Laboratories, Warrington, United Kingdom, operated by Dr. Bernhard Schaffer. The general procedure was to tilt the grain on one side of the grain boundaries in zone axis orientation to obtain atomic resolution. The transition between the region that exhibited atomic resolution and the region that did not was identified as the grain boundary. Spectrum images were then acquired in a region of interest across the grain boundaries. Typical acquisition times of the single spectra were about 1 s. A collection semi-angle of about 32 mrad and a convergence semi-angle of about 18.5 mrad were used for all measurements.

EFTEM in combination with Eq. (3.26) was applied in order to measure the local thickness $d(\vec{r})$ of the specimen regions for which the phase shift $\varphi(\vec{r})$ or the relative phase shift $\Delta\varphi(\vec{r})$ was determined. It was taken care that the thickness measurements were performed shortly after the image acquisition for electron holography, at the same tilt angles.

3.2.8 TEM specimen preparation

The quality of the specimen plays an important role for TEM analysis. Prerequisite for the suitability of a specimen for TEM investigations is its thickness of less than ~ 150 nm, which is necessary for a sufficient transmission of the electron beam. In addition, as little modification of the primary material as possible is desired. This modification includes surface and volume contaminants as well as elutriation of constituents. A high surface roughness can also be detrimental to quantitative analysis. Therefore, suitable specimen preparation techniques must be applied (for an overview see Refs. [147, 148]). Three different preparation methods were employed in the present work which are illustrated briefly in the following.

1. T-tool polishing method: First, two pieces of solar cells were glued together face to face, such that the ZnO layers were completely covered with glue. The glue was a Gatan G-1 epoxy glue that hardens within 2 h at an ambient temperature of 60 °C. Cross-section stripes, about 0.5 mm thick, were cut out from this stack perpendicular to the glue line. The cross-section stripes were then mechanically polished by use of a T-tool, which is similar to a Tripod. The T-tools are made of a pod with two Teflon legs that are precisely adjustable in height by micrometer screws, whereas the sample is mounted at the position of the third leg. Stabilizing and supporting Mo rings with an inner diameter of 1 mm were glued on the cross-section stripes as soon as their thickness was smaller than 10 μm , such that the glue line—and with it the cross-sections of the absorbers—ran along the diameter of the Mo rings. Carbon fibers glued on the cross-section stripes perpendicular to the glue line additionally stabilized the specimen. The final TEM specimen was obtained by subsequent Ar-ion polishing at an incidental angle of the ion beam of about 6 – 12° with respect to the specimen surface.
2. H-bar method: In contrast to the T-tool polishing method, solar cell cross-sections

cut out from a solar cell stack, were mechanically polished by use of a T-tool, until about $20\ \mu\text{m}$ thickness was reached. Mo half rings were glued on these cross-sections such that the solar cell cross-sections were flush with the full diameter of the half-rings. Finally, a Zeiss Gemini 1540 Crossbeam focused ion beam (FIB) was employed in order to thin down the cross-section further, until it was transmissive for the electron beam. Further Ar-ion milling was applied in some cases in order to reduce the specimen thickness and surface contamination as well as surface damage.

3. Pure FIB method: Lamellae of the solar cell cross-section, with a thickness in the order of $20 - 100\ \text{nm}$ were cut out of the solar cells by use of a FIB (Zeiss Gemini 1540 Crossbeam). Subsequently, a micromanipulator needle was used to extract the lamellae from the substrate and weld them to an appropriate TEM grid by use of Pt gas.

3.3 Atom probe tomography

The atom probe tomography (APT) results shown in the present work (see Sec. 4.4.1.2) were measured by O. Cojocaru-Mirédin and P.-P. Choi, Max Planck Institute for Iron Research, Düsseldorf, Germany, by use of a LEAP3000X HR atom probe. In general, APT may be applied to characterize the three-dimensional elemental distribution within solids on a subnanometer resolution [149]. In the case of semiconductors, surface atoms on a positively biased tip-shaped specimen¹ are successively ionized and field-evaporated by use of laser pulses. The field-evaporated ions are accelerated towards a position sensitive detector that records their time of flight and impact positions. The three-dimensional elemental distribution can be reconstructed from the collected data by use of an inverse point projection algorithm. In principle, atomic resolution is achievable by use of APT, however, this requires special orientations of the crystal lattice with respect to the tip of the specimen.

¹The radius of curvature of these tips is typically smaller than $100\ \text{nm}$

Chapter 4

Grain boundaries in Cu(In,Ga)Se₂ and CuInS₂ thin films studied by TEM

The results obtained by electron holography are presented and discussed in this chapter. The discussion covers possible measurement artifacts and a comparison of the results with others from similar measurements on grain boundaries in different materials. Highly symmetric $\Sigma 9$ and $\Sigma 3$ (twin) grain boundaries serve as model systems. Results and simulations on these model systems are compared with each other, as well as compared with the results obtained on random grain boundaries. The findings are then correlated with results on the local composition of grain boundaries within Cu(In,Ga)Se₂ measured by use of EELS. The measurements are then combined leading to a model for the band diagram of grain boundaries within Cu(In,Ga)Se₂ thin film solar cell absorbers, which is discussed with respect to models discussed in the literature. A summary concludes the chapter.

4.1 Averaged electrostatic potential measurements

Some of the grain boundary models described in Sec. 2.3.2 involve potential distributions owing to space charge (or excess charge) regions adjacent to grain boundaries screening the electric field of bound excess charges at their core. Such potential distributions may act as barriers or sinks for charge carriers, which, if large enough, can have a huge impact

on the electronic transport properties of the absorber and, simultaneously, the conversion efficiency of the corresponding solar cells. It may therefore be essential to study and understand the electrostatic potential at grain boundaries within the absorbers in order to improve the conversion efficiency of the solar cells.

This section gives the results on the averaged electrostatic potentials $V_a(\vec{r})$ or differences $\Delta V_a(\vec{r})$ in it at and in the vicinity of grain boundaries in Cu(In,Ga)Se₂ and CuInS₂ thin films determined by use of inline and off-axis electron holography in TEM. The section also deals with the influence of the surface properties of the TEM lamellae, as well as the influence of free charge carriers generated by the electron beam. Possible origins of the measured results are discussed.

4.1.1 Grain boundaries in Cu(In,Ga)Se₂ absorbers and their dependence on the integral composition

Electron holography in TEM was applied in the present work in order to study the averaged electrostatic potential $V_a(\vec{r})$ at and in the vicinity of grain boundaries in Cu(In,Ga)Se₂ thin-film solar cell absorbers. Dependencies of this potential on the absorber composition were studied with the help of absorbers with compositions exhibiting various $[Ga]/([In] + [Ga])$ and various $[Cu]/([In] + [Ga])$ ratios. Fig. 4.1 shows results from these absorber layers obtained by use of inline electron holography. Profiles of individual grain boundaries were extracted in each case in order to obtain statistics for each material. Fig. 4.2 shows bright-field TEM overview images and detailed views of two exemplary grain boundaries within absorbers of the Cu series to illustrate the selection of the grain boundaries (see Sec. 3.2.6). The inelastic mean free path was calculated for each composition as described in Sec. 3.2.7. For the retrieval of $\Delta V_a(\vec{r})$, it was assumed that the inelastic mean free paths do not change significantly at the grain boundary (cores). A smooth behavior of $d(\vec{r})/\lambda$ (see Eq. (3.26)) with respect to the adjacent grain interiors was found for all investigated grain boundaries, also within CuInS₂ and CuGaSe₂. The assumption therefore implies a smooth local specimen thickness at the grain boundaries with respect to the adjacent regions. It should be noted that this might not be the case in general. The mean value of the averaged electrostatic potential in the grain interiors, where no significant systematic behavior apart from fluctuations around the mean value and noise could be detected, was chosen as zero point.

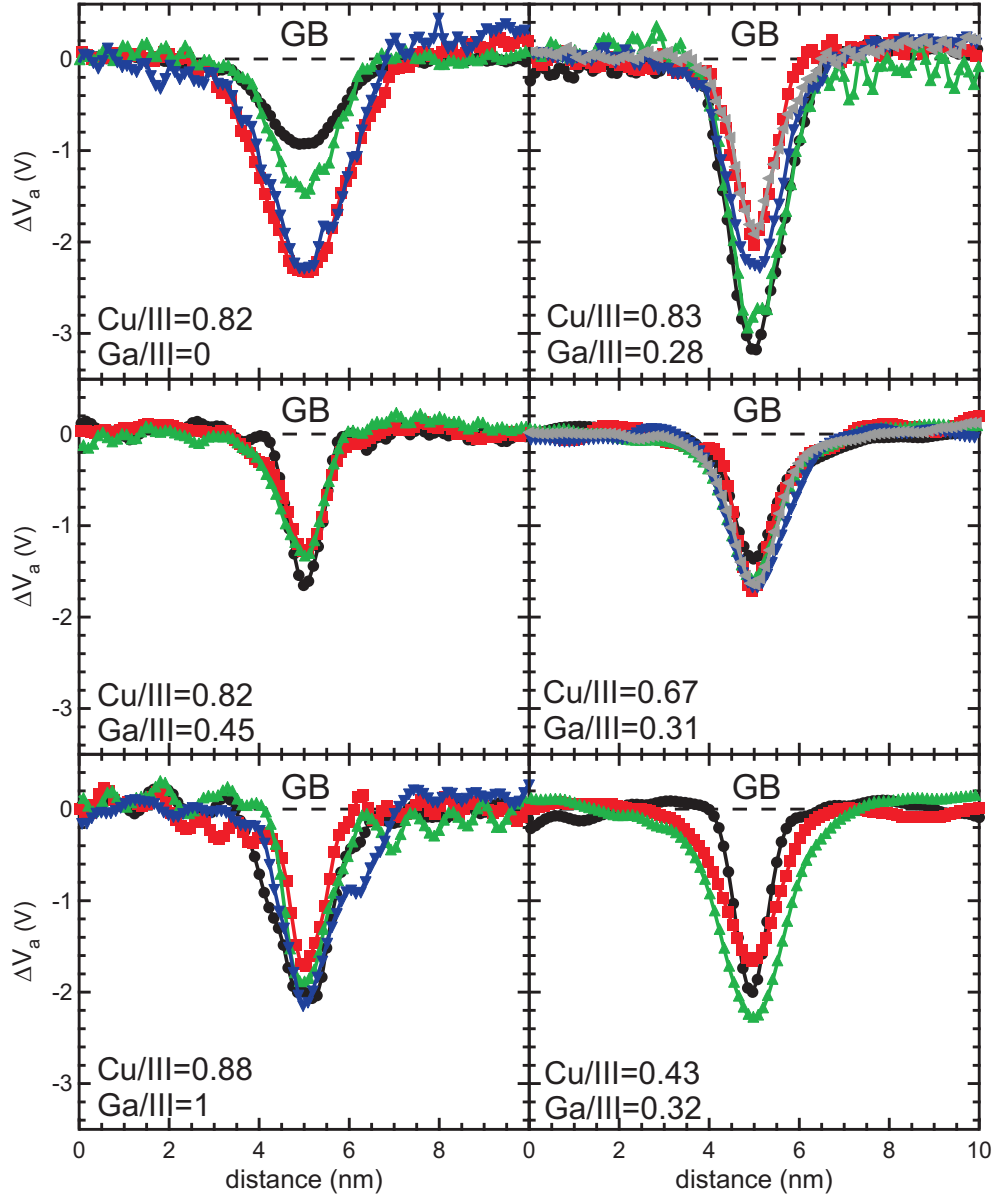


Figure 4.1: Profiles of differences in the averaged electrostatic potential $\Delta V_a(\vec{r})$ extracted across individual grain boundaries (GB) in $\text{Cu}(\text{In},\text{Ga})\text{Se}_2$ solar cell absorbers with various composition. Different colors represent individual grain boundaries. The $[\text{Ga}] / ([\text{In}] + [\text{Ga}])$ ratio was varied as 0, 0.45, 1 for an approximately constant $[\text{Cu}] / ([\text{In}] + [\text{Ga}])$ ratio of about 0.85 (Ga series). The $[\text{Cu}] / ([\text{In}] + [\text{Ga}])$ ratio was varied as 0.43, 0.67, 0.83 for an approximately constant $[\text{Ga}] / ([\text{In}] + [\text{Ga}])$ ratio of about 0.3 (Cu series).

A lowering of the averaged electrostatic potential located at the grain boundary cores was found in the case of all absorbers, independently of their compositions. This lowering of the potential will be referred to as potential wells in the following. While the full width at half minimum (FWHM) of about 1 – 2 nm is similar for all investigated grain boundaries, the depths of the potential wells vary with composition of the absorbers and from grain boundary to grain boundary, even within identical layers. The averaged electrostatic potential is dominated by small fluctuations and noise in the grain interiors. More than ~ 2 nm away from the grain boundary core, no significant deviation of the mean value $\langle \Delta V_a(\vec{r}) \rangle$ from $\langle \Delta V_a(\vec{r}) \rangle = 0$ was found. Hence, regions more than 5 nm away from the potential wells are omitted in Fig. 4.1. Note that the applied method of inline electron holography is capable of imaging spatial frequencies corresponding to distances of about 0.8 – 20 nm.

The standard deviation in the grain interior originates mainly from small fluctuations and noise in the phase shift $\Delta\varphi(\vec{r})$, which is caused by the standard deviation in the image intensity of the acquired through focal series, the image alignment in the phase reconstruction, as well as the quality of the specimen, i.e., local thickness variations, surface roughness, contamination, possible precipitates, etc. Periodic fluctuations, e.g. as found in the case of the absorber with composition of $[Cu]/([In] + [Ga]) = 0.88$ and $[Ga]/([In] + [Ga]) = 1$, may also originate from a slight defocus or other aberrations in the object wave, resulting in Fresnel fringes, which are apparent as periodic fluctuations in the potential profiles. Periodic fluctuations seem to occur predominantly if the image intensities within the through focal series are low. Owing to the worse signal-to-noise ratio of the images, the reconstruction of the object wave might be less reliable.

In the profiles shown in Fig. 4.1, the standard deviation of the averaged electrostatic potential $\sigma(\Delta V_a(\vec{r}))$ in the grain interiors, 2 – 10 nm away from the grain boundary core (not shown here), do not exceed 0.1 V. Due to the symmetry and the extraction procedure of the profiles, the rough estimate $\sigma(\Delta V_a(\vec{r})) = 0.1$ V is therefore considered as detection limit of the applied evaluation method for averaged electrostatic potentials which exhibit equipotential lines parallel to the grain boundary. It should be pointed out that the uncertainty of the value for the inelastic mean free path λ_{mfp} may lead to a systematic error of the potential well depths of up to 10 %. However, the error of the inelastic mean free path is assumed to be similar in the case of all compositions due to the similarity of the materials, which makes the potential wells comparable with each other. Tab. 4.1 shows

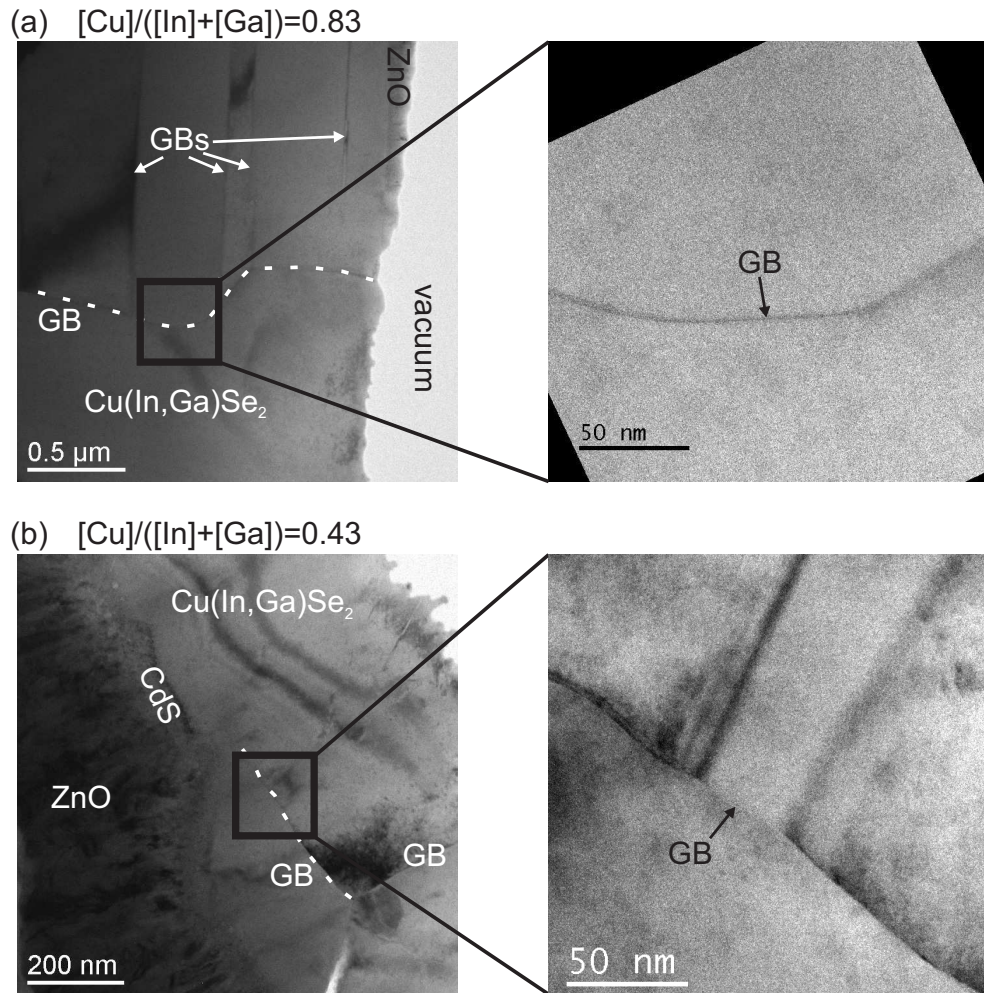


Figure 4.2: Bright-field TEM overview images and detailed view of two grain boundaries (GB) within absorbers from the Cu series. (a) A grain boundary within an absorber with a composition exhibiting $[Cu]/([In] + [Ga]) = 0.83$ and $[Ga]/([In] + [Ga]) = 0.28$. The corresponding profile of the averaged electrostatic potential is shown as the green curve in the respective graph in Fig. 4.1. (b) A grain boundary within an absorber with a composition exhibiting $[Cu]/([In] + [Ga]) = 0.43$ and $[Ga]/([In] + [Ga]) = 0.32$. The corresponding profile of the averaged electrostatic potential is shown as the black curve in the respective graph in Fig. 4.1. Both profiles were extracted at the position highlighted by the black arrow.

the mean values of the potential well depths and the corresponding standard deviations from the potential profiles shown in Fig. 4.1.

The typical specimen thicknesses at the regions of interest where the profiles in Fig. 4.1 were extracted from were about 50 nm. However, in some cases, they were as small as

Table 4.1: Mean values and standard deviations of the averaged electrostatic potential well depths found at grain boundaries in Cu(In,Ga)Se₂ absorber films with varying composition (see Fig. 4.1).

	mean potential well depth (V)	standard deviation (V)
Cu series		
[Cu]/([In] + [Ga]) = 0.83	-2.47	0.57
0.67	-1.60	0.14
0.43	-1.98	0.32
Ga series		
[Ga]/([In] + [Ga]) = 0	-1.76	0.67
0.45	-1.43	0.20
1	-1.96	0.18

about 20 nm. No correlation between the potential well depths and the specimen thickness was found in the presented results.

The widths of the potential wells are close to the spatial resolution of the applied method of about 0.8 nm. Thus, the width of the potential wells is an upper limit of the length scale on which changes in the averaged electrostatic potential actually occur. In addition, the measured potential wells only show an average value along the z axis. If the grain boundaries are not accurately tilted edge-on¹ or are not planar but run zigzag through the specimen, the measurement overestimates the actual potential well widths. For the same reason, it is assumed that the measured potential well depths represent an underestimation of the actual potential well depths present at grain boundaries rather than an overestimation. Slightly different diffraction conditions on either side may also lead to an asymmetry of the potential wells as found in some cases (see Fig. 4.1). With the help of measurements at different tilt angles, which were performed at some grain boundaries, it could be shown that asymmetric potential wells are avoided by an optimization of the tilt angles.

It was furthermore found that the potential well depths vary slightly (< 0.3 V) with respect to the position of the region of interest. Despite the fact that the investigated absorbers exhibited a Ga (or equivalently an In) concentration gradient along the distance from the back contact, no correlation between the shape of the potential wells and the distance of the corresponding grain boundaries from the back contact was found.

¹This is treated in Sec. 4.2.4 using the example of a $\Sigma 9$ grain boundary.

4.1.2 Comparison of off-axis and inline electron holography

The lower limit of spatial frequencies that can be imaged by inline electron holography corresponds to about 20 nm (see Sec. 3.2.4) and may not be large enough to obtain information on the electrostatic potential distribution that is possibly caused by a bound excess charge at grain boundaries since the corresponding extensions can be larger than 100 nm (see Fig. 2.6). Since these potential distributions affect the electrical properties of the Cu(In,Ga)Se₂ layers, it is of great interest to gain more information on that issue. In comparison with inline electron holography, off-axis electron holography in TEM is suitable for the imaging of the electrostatic potential on distances larger than 20 nm (see Sec. 3.2.3).

In order to measure the averaged electrostatic potential in a longer range and to compare the two different methods, off-axis electron holography (at medium resolution) and inline electron holography were performed at the same grain boundary within CuInSe₂. Fig. 4.3 shows profiles that have been extracted at the same position along the mentioned grain boundary. Only the change in potential $\Delta V_a(\vec{r})$ is shown in the case of the profiles that have been determined by means of off-axis electron holography, in order to show comparable results with the ones obtained by use of inline electron holography.

Now consider the profile determined by use of off-axis electron holography, which extends over a distance of 140 nm. Note that due to the high spatial coherence of the electron beam during the acquisition of off-axis electron holograms, phase information with distances of more than 140 nm should be retrievable accurately. There are fluctuations in the profile, especially at distances above ~ 70 nm. This is attributed to a high local surface roughness of the specimen and dynamical diffraction conditions that are locally met. It should be pointed out that the investigated specimens were usually strongly bent, which was apparent in a high density of bend contours in the bright-field TEM images. This fact made it difficult to determine phase shifts in regions of interest with an extension of more than hundred nm since dynamical diffraction conditions are likely to be met somewhere in this region. The standard deviation at distances below 68 nm is 0.21 V, and is assumed to be the detection limit here. Apart from the fluctuations, no systematic potential variation, that can be correlated with the presence of a space-charge or excess-charge layer adjacent to the grain boundary, was noticeable on both sides of the grain boundary.

Fig. 4.3 also shows a direct comparison of the off-axis and inline electron holography results within a region of interest extending over 24 nm around the grain boundary. Both profiles

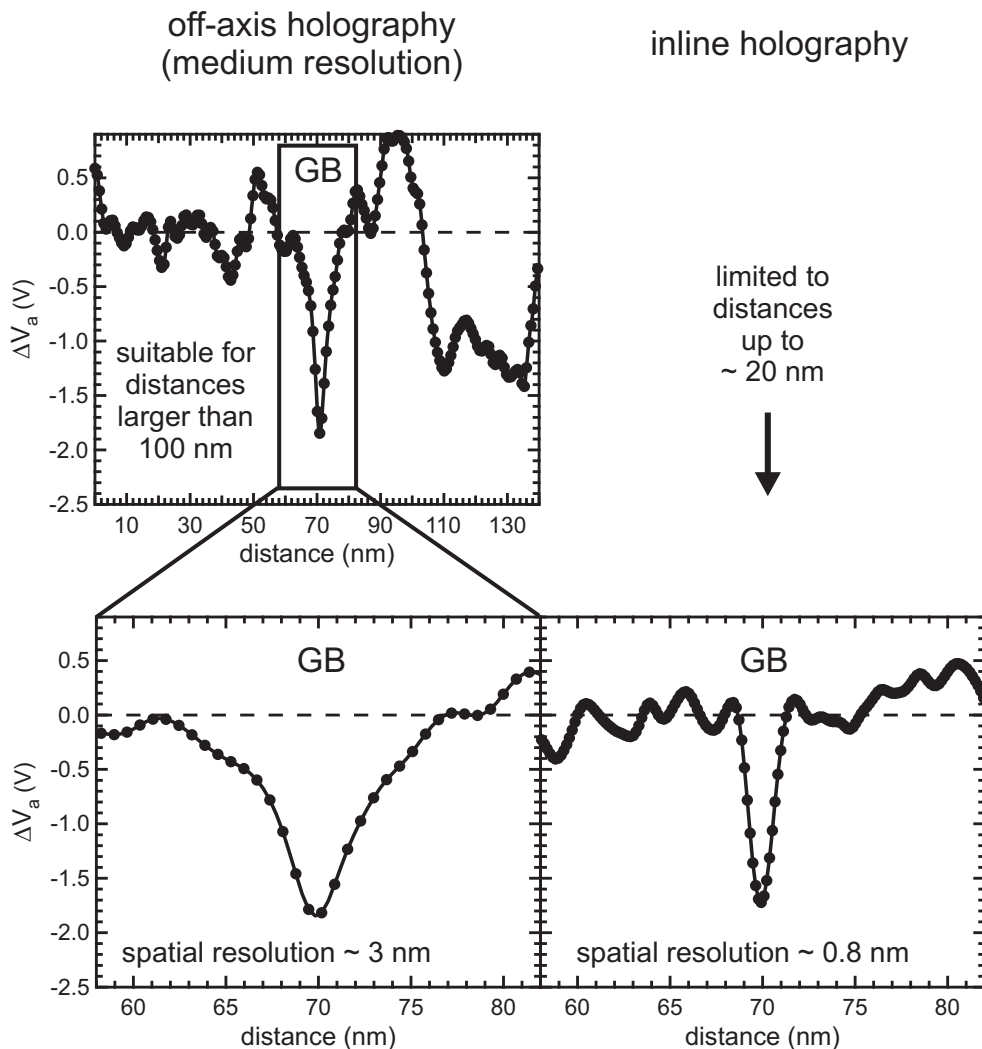


Figure 4.3: Profiles of the relative averaged electrostatic potential $\Delta V_a(\vec{r})$ that were measured by use of off-axis and inline electron holography on the same grain boundary (GB) within a CuInSe₂ thin film exhibiting $[Cu]/([In] + [Ga]) = 0.82$. The profile that was determined by use of off-axis electron holography is shown for a distance of 140 nm. A direct comparison of this profile with the profile that was determined by use of inline electron holography is shown for a region of interest with an extent of 24 nm. Both profiles exhibit potential wells with depths of ≈ 2 V at the grain boundary, which is located at a distance of 70 nm. Due to the lower spatial resolution (~ 3 nm) of the applied medium resolution off-axis electron holography, the FWHM of the potential well (~ 5 nm) is substantially wider than the FWHM detected by use of inline electron holography (1 – 2 nm). These data have been acquired in collaboration with John Sandino, Triebenberg Laboratory, Technische Universität Dresden, Dresden, Germany.

show potential wells at the grain boundary, and the potential well depths are in both cases $\approx -2\text{ V}$. The significant difference of the FWHM of the potential wells, $\sim 5\text{ nm}$ in the case of off-axis electron holography and $\sim 2\text{ nm}$ in the case of inline electron holography arise due to the lower spatial resolution of medium resolution off-axis electron holography of about $\sim 3\text{ nm}$. Because of the lower resolution, the potential well measured by means of off-axis holography is expected to correspond to the one measured by means of inline electron holography, however, smeared out. Hence, the area of the potential wells below the zero line are expected to be similar. It is therefore not clear why both profiles exhibited potential wells with a depth of $\approx -2\text{ V}$, whereas their widths differed significantly. Further investigations are required on that issue. Nevertheless, the presence of potential wells at grain boundaries could be verified by use of off-axis electron holography.

4.1.3 The mean inner potential of CuInSe₂

For the further evaluation of the potential wells, it is necessary to examine if the constraint that was assumed for the superposition of the MIP and potentials caused by a redistribution of free charge carriers (see Eq. (3.22)) is met, i.e., that $\Delta V_{\text{cr}} \ll \text{MIP}$. This requires a determination of the MIP of Cu(In,Ga)Se₂.

The MIP of CuInSe₂ was determined by use of off-axis electron holography. For this purpose, individual profiles of the phase $\varphi(\vec{r})$ were extracted from the corresponding gray-value images and averaged. The profiles were chosen such that a part of the profiles included the phase within the vacuum region and a part of the profiles included the phase within the specimen. The direction of the profiles was perpendicular to the interface between the vacuum region and the specimen in the gray-value images. Features associated with grain boundaries were not included in these profiles. Due to external electrical fields owing to charging of the specimen, the phase in the vacuum region exhibited a slope. This slope and an offset were subtracted from the phase, in order to achieve a flat phase with a value of about zero in the vacuum region. The averaged electrostatic potential was then calculated according to Eq. (3.24), for which thickness profiles were extracted from the same region of interest. The permittivity of the specimen is different from the one in vacuum. Hence, the profiles exhibited a slope in the averaged electrostatic potential within the specimen region. Subtracting the slope and adding an offset, such that the phase on the vacuum side of the vacuum/specimen interface was zero, resulted in a flat profile in the specimen region

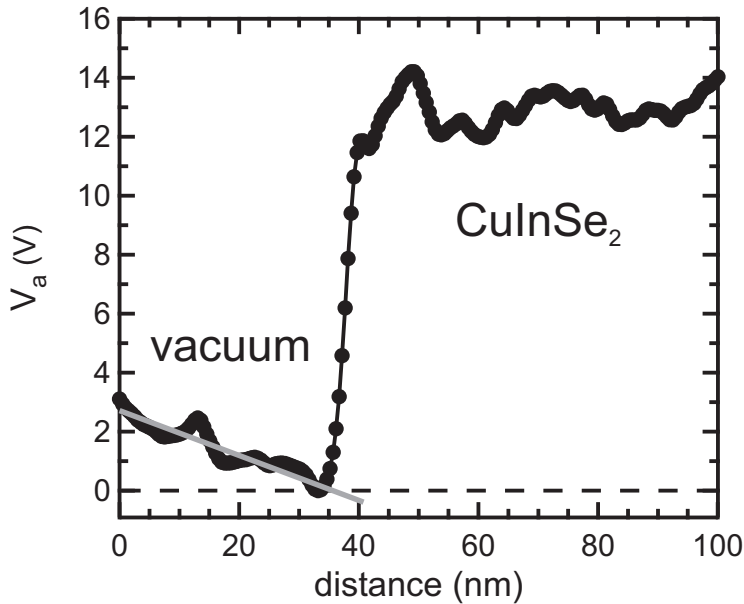


Figure 4.4: Profile of the averaged electrostatic potential extracted from a vacuum/specimen interface in order to determine the MIP of the specimen (CuInSe₂). Due to external fields, a slope had to be subtracted from the potential profile in order to achieve a flat potential in the specimen region. The potential on the vacuum side of the vacuum/specimen interface was used as zero point. The slope in the vacuum region, denoted by a thin line, is due to a different permittivity of the specimen compared with vacuum. These data have been acquired in collaboration with John Sandino, Triebenberg Laboratory, Technische Universität Dresden, Dresden, Germany.

with the absolute value of the MIP of CuInSe₂. Fig. 4.4 exemplarily shows a potential profile. The value of the MIP of CuInSe₂ averaged from four different profiles, was found to be $\text{MIP}(\text{CuInSe}_2) = (14.0 \pm 1.6) \text{ V}$.

Even if the potential wells with a depth of up to 3 V at grain boundaries are solely caused by a local change in ΔV_{cr} , the constraint $\Delta V_{\text{cr}} \ll \text{MIP}$ seems to be met satisfactorily. It was not possible yet to determine the MIP of the other investigated Cu(In,Ga)(Se,S)₂ thin films, however, it is assumed in the following that the constraint is also met in these cases.

4.1.4 Grain boundaries in CuInS₂ absorber films

Fig. 4.5 shows profiles of differences in the averaged electrostatic potential $\Delta V_a(\vec{r})$ extracted across individual grain boundaries in CuInS₂ solar cell absorbers. The results are similar to those obtained for grain boundaries in Cu(In,Ga)Se₂. I.e., potential wells with a FWHM

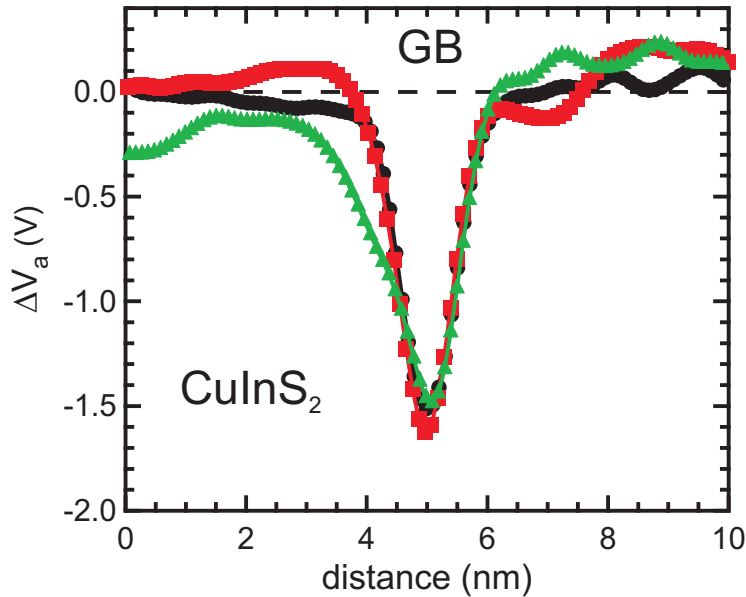


Figure 4.5: Profiles of differences in the averaged electrostatic potential $\Delta V_a(\vec{r})$ extracted across individual grain boundaries (GB) in CuInS₂ solar cell absorbers. Inline electron holography was applied in order to obtain the corresponding changes in the object wave phase $\Delta\varphi(\vec{r})$.

of 1 – 2 nm are found at the grain boundaries, while the potential shows a small standard deviation < 0.1 V in the grain interiors, where the mean value is $\langle \Delta V_a(\vec{r}) \rangle \approx 0$. The potential wells at the investigated grain boundaries exhibit a mean depth of about (-1.50 ± 0.03) V. The standard deviation of 0.03 V is small compared with the ones found for potential well depths at grain boundaries in Cu(In,Ga)Se₂ with various composition (see Tab. 4.1).

4.1.5 Single $\Sigma 9$ grain boundary in CuGaSe₂

A highly symmetric $\Sigma 9$ (111) 180° rotational twin grain boundary within a CuGaSe₂ thin film was studied for the present work by means of inline electron holography and served as model system. The CuGaSe₂ film exhibiting the single $\Sigma 9$ grain boundary was epitaxially grown on a GaAs bicrystal exhibiting the corresponding $\Sigma 9$ grain boundary. It is unclear whether the CuGaSe₂ layer is suitable as a thin film solar cell absorber. Corresponding results might therefore not be comparable with the ones obtained on polycrystalline CuGaSe₂ thin films. A bright-field TEM overview image and a gray-value phase image of the grain

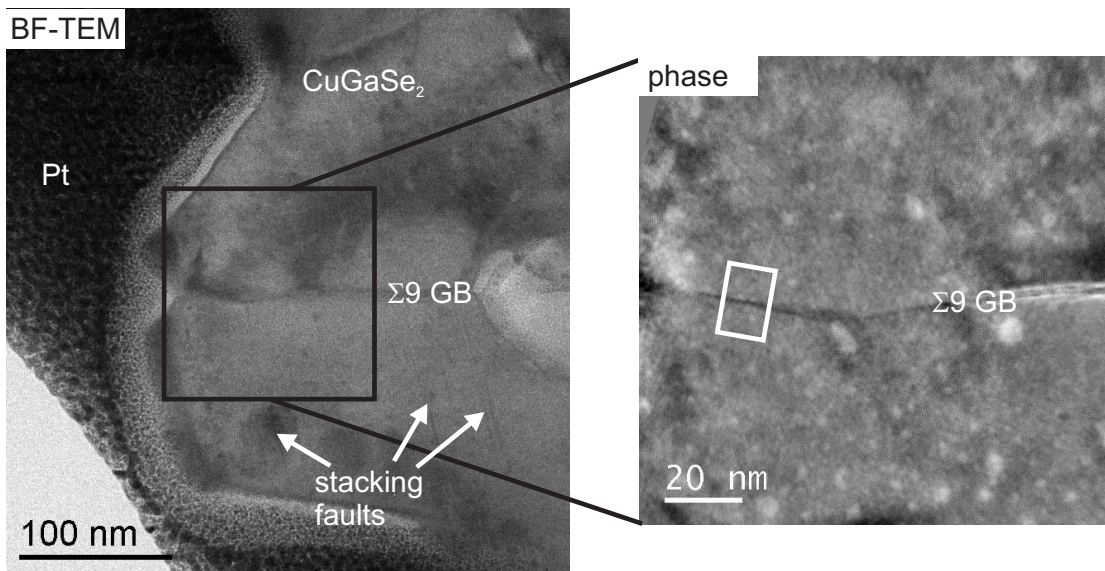


Figure 4.6: Bright-field TEM overview image of a $\Sigma 9$ (111) 180° rotational twin grain boundary ($\Sigma 9 \text{ GB}$) within a CuGaSe_2 thin film that was epitaxially grown on a GaAs bicrystal and corresponding gray-value phase image obtained by use of inline electron holography. The white frame denotes the region of interest from which the phase profiles were extracted.

boundary are shown in Fig. 4.6. Although the grain boundary is supposed to be highly symmetric, its projection is curved at some positions. The presence of stacking faults also indicates that the material might be stressed. Phase profiles extracted within the region of interest denoted by the white frame were employed to determine the averaged electrostatic potential profiles. The projection of the grain boundary in this region is straight and therefore assumed to exhibit the highest symmetry. Fig. 4.7 shows two resulting profiles of the averaged electrostatic potential extracted at two different locations across this grain boundary. As before, a potential well was found at the position of the grain boundary. While the FWHM of the potential well has about the same value as found in all previous measurements, its average depth of (-0.68 ± 0.04) V is significantly smaller.

4.1.6 Comparison of grain boundaries exhibiting different symmetries

A comparison of averaged electrostatic potential profiles extracted across three grain boundaries exhibiting different symmetries with respect to the adjacent grain interiors and the

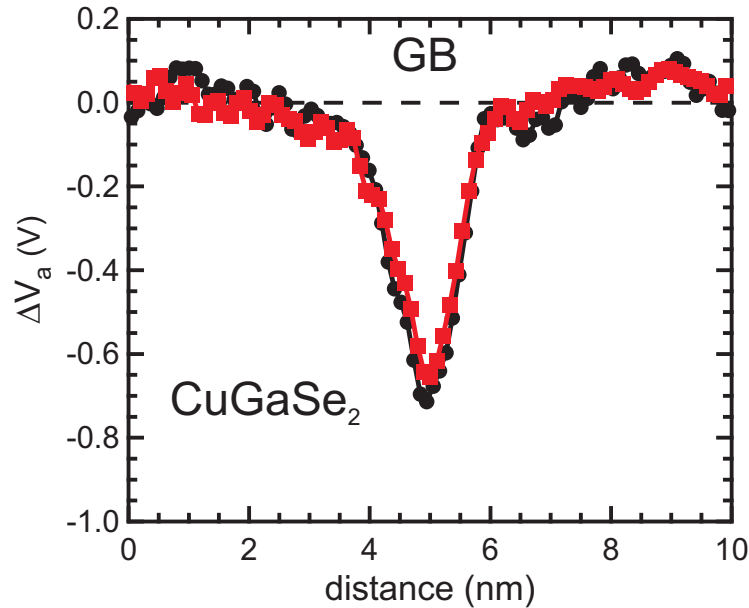


Figure 4.7: Profiles of changes in the averaged electrostatic potential $\Delta V_a(\vec{r})$ extracted across a $\Sigma 9$ grain boundary (GB) in a CuGaSe_2 thin film, which was epitaxially grown on a GaAs bicrystal exhibiting the corresponding $\Sigma 9$ grain boundary. The two profiles were extracted at two different positions, 10 nm apart from each other, within the white frame in Fig. 4.6. Inline electron holography was applied in order to obtain the corresponding changes in the phase $\Delta\varphi(\vec{r})$ of the object wave function.

plane of the grain boundary core, is shown in Fig. 4.8 to study the effect of the grain boundary symmetry. The comparison comprises a $\Sigma 3$ twin grain boundary within a $\text{Cu}(\text{In},\text{Ga})\text{Se}_2$ absorber (taken from Ref. [92]), a $\Sigma 9$ grain boundary within epitaxially grown CuGaSe_2 (see Sec. 4.1.5), and a random grain boundary within a $\text{Cu}(\text{In},\text{Ga})\text{Se}_2$ thin film exhibiting $[\text{Cu}] / ([\text{In}] + [\text{Ga}]) = 0.83$ and $[\text{Ga}] / ([\text{In}] + [\text{Ga}]) = 0.28$. The latter profile was chosen, for it exhibits the potential well depth closest to the mean value for grain boundaries within this absorber (see Tab. 4.1). Although the materials have different compositions, it seems that the potential well depth is larger, the lower the symmetry of the grain boundary is. The smallest potential well depth of about -0.2 V is found at the $\Sigma 3$ twin grain boundary, the largest depth of about -2.3 V is found at random grain boundaries. The potential well depth of -0.68 V of the $\Sigma 9$ grain boundary is in between the two extrema. The influence of symmetry on the properties of grain boundaries will be discussed in Sec. 4.4.2.6

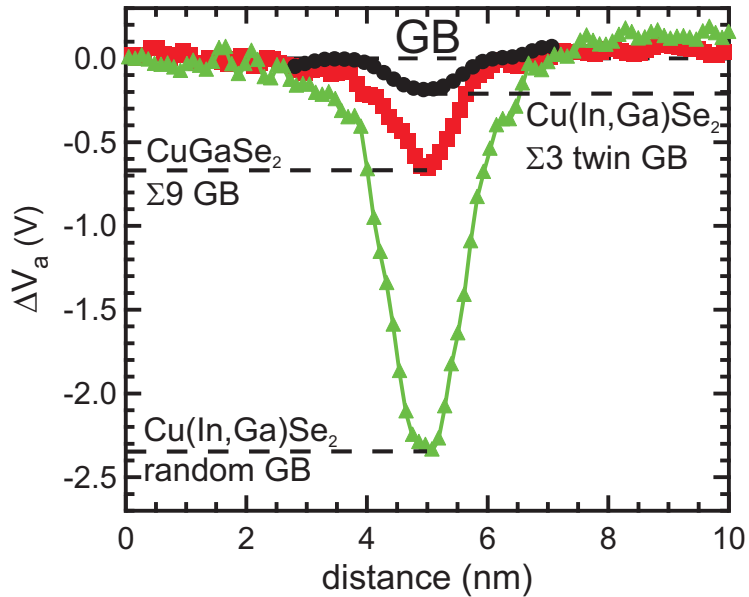


Figure 4.8: Comparison of profiles of changes in the averaged electrostatic potential $\Delta V_a(\vec{r})$ extracted across a $\Sigma 3$ twin grain boundary (GB) within a Cu(In,Ga)Se₂ absorber (taken from Ref. [92]), across a $\Sigma 9$ grain boundary within epitaxially grown CuGaSe₂, and across a random grain boundary within Cu(In,Ga)Se₂ exhibiting $[Cu]/([In] + [Ga]) = 0.83$ and $[Ga]/([In] + [Ga]) = 0.28$. The latter was already shown in Fig. 4.1 and represents the average potential well depth.

4.2 Discussion on possible origins of the measured potential distributions

Although no simple dependence of the potential well depths on the composition was found, the existence of potential wells with similar FWHM of about 1 – 2 nm at all investigated grain boundaries in Cu(In,Ga)Se₂ and CuInS₂ thin films itself is striking. Possible reasons for the existence of the potential wells are discussed in this section before a conclusion is drawn.

There are several possible origins that may cause such potential wells at grain boundaries. According to Eq. (3.22), either changes in MIP(\vec{r}) and/or changes in $\Delta V_{cr}(\vec{r})$ can be responsible for the potential wells, if perturbations due to fringing fields and surface effects, such as dipole layers, dead layers on either side of the specimen, and surface grooves are neglected. First, the perturbation of the measurement by the electron beam is estimated. Then, the possible origins of the potential wells are successively discussed. Only origins

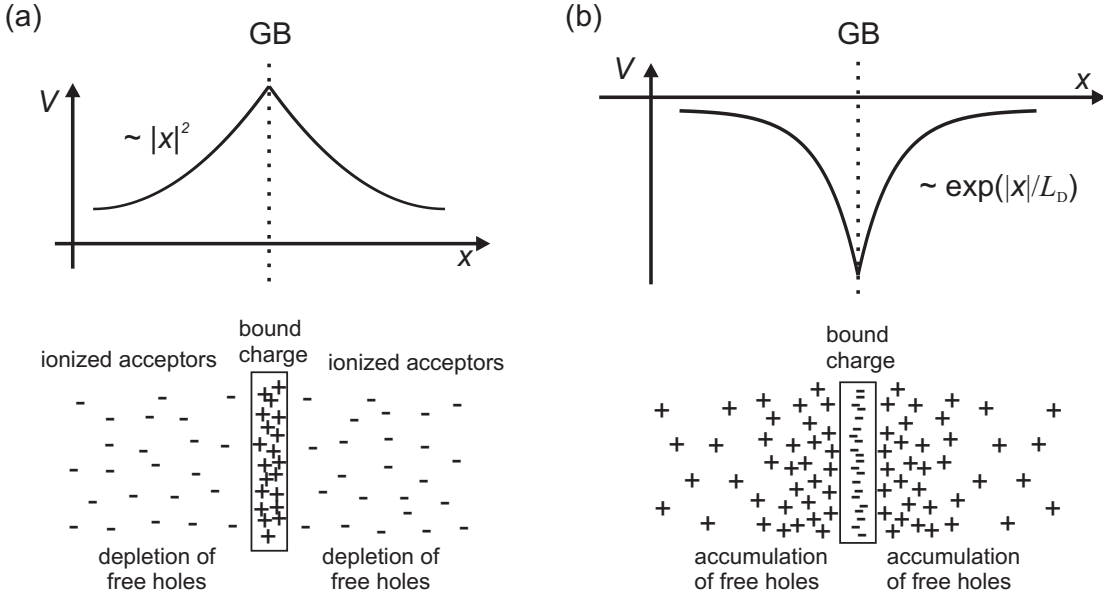


Figure 4.9: Schematic of the charge carrier densities and the corresponding one-dimensional electrostatic potential distributions if an excess charge is bound at a grain boundary within a *p*-type semiconductor. (a) If positive excess charge is bound at a grain boundary, free holes in the valence band are repelled from the grain boundary core and leave a hole depleted space charge region of ionized (negatively charged) acceptors. In the framework of the depletion approximation [150], the free hole density in the hole depleted region is assumed to be zero, resulting in a constant negative charge density. According to Poisson's equation (Eq. (3.25)), this leads to a potential distribution which increases quadratically towards the grain boundary core. This is discussed in Sec. 4.2.1.3. (b) If negative excess charge is bound at a grain boundary, the free holes are attracted towards the core. In the case of quasi-neutrality (i.e., the potential wells are small compared with kT , where k is the Boltzmann constant and T the temperature), the increase of the free hole density increases exponentially towards the grain boundary core [151], leading to an exponentially increasing potential (see Eq. (3.25)). This case is discussed in Sec. 4.2.1.2 and Sec. 4.2.1.3.

with a symmetric configuration are taken into account, since the measured potential wells are in a good approximation symmetric with respect to the grain boundary. Systematic measurement artifacts due to fringing fields around the specimen, dead layers, and surface grooves are neglected at first. They are then discussed in Sec. 4.2.5.

4.2.1 Redistribution of free charge carriers at grain boundaries

If a grain boundary is considered a plane containing bound excess charges at its core, space charge or excess charge layers—depending on the polarity of the charge at the grain boundary core and on the doping of the grain interior—would symmetrically form on either side of the grain boundary². According to Poisson's equation (Eq. (3.25)), these charged layers may cause electrostatic potential variations $\Delta V_{\text{cr}}(\vec{r})$ at and in the vicinity of the grain boundary. Fig. 4.9 illustrates the situation and the corresponding one dimensional potential distribution in the case of positive and negative bound excess charge at a grain boundary within a *p*-type semiconductor. Such potential distributions may contribute or even cause the potential wells that were found by use of electron holography. In this section, possible contributions of $\Delta V_{\text{cr}}(\vec{r})$ to $\Delta V_a(\vec{r})$ (see Eq. (3.23)) are studied by effectively neglecting any changes $\Delta \text{MIP}(\vec{r})$ in the MIP.

At first, the generation of free charge carriers by the electron beam is estimated, for it may affect the potential distribution in the vicinity of grain boundaries during the measurement. It is then studied, if a redistribution of free charge carriers gives a significant contribution to the measured potential wells. Finally, potential wells and barriers below the detection limit of the applied method are discussed.

4.2.1.1 Generation of free charge carriers by the electron beam

An electron beam impinging on a semiconductor is known to perturb the equilibrium state by exciting electrons from electronic states within the valence band to electronic states within the conduction band [152]. This process is called generation of free charge carriers, for it increases the number of mobile electrons and holes within both bands. It has to be considered that such an increase of the local free charge-carrier density, including minority and majority charge carriers, may alter the potential distribution, which is subject to the measurement, substantially. A detailed evaluation of the averaged electrostatic potential distributions across grain boundaries therefore requires an estimation of the generation of free charge carriers within the specimen by the electron beam.

While passing through matter, electrons with a certain kinetic energy exchange energy with the matter. In average, this results in a deceleration of the electrons. The average energy loss dE per unit path length dx of the electrons (with a certain kinetic energy) in

²This is only true, if the adjacent grains exhibit the same doping densities

matter is given by the stopping power $-dE/dx$. The theoretical concept of the stopping power for electrons with kinetic energies above 10 keV and its evaluation was derived by Bethe in 1930 [153], in the framework of the non-relativistic scattering theory developed by Born [154]. Due to the complexity and the large number of involved scattering processes, it is not possible to evaluate the stopping power of a solid by theory alone. Instead, suitable methods combining theoretical considerations and experimental input are applied. In the following, the relativistic collision stopping power of CuInSe₂, CuGaSe₂, and CuInS₂ for 200 keV electrons is evaluated on the basis of the work of Seltzer et al. [155], where energy loss due to bremsstrahlung is neglected. This is a valid simplification since no significant contribution to the stopping power owing to bremsstrahlung is expected for 200 keV electrons [156]. The main task for the determination of the collision stopping power is the accurate evaluation of the mean excitation energy I of the particular compound Cu(In,Ga)(Se,S)₂.

According to Seltzer et al. [155], the electron collision stopping power of a medium, in units of MeV/cm, is given by

$$-\frac{dE}{dx} = \frac{0.153536 \rho Z}{\beta^2 A} B(T), \quad (4.1)$$

where ρ in units of g/cm³ is the mass density of CuInSe₂, β the velocity in units of the velocity of light, Z and A are atomic number and weight of the medium, T the kinetic energy of the electron, and $B(T)$ the stopping number. The stopping number

$$B(T) = \ln(\tau^2(\tau + 2)/2) + (1 + \tau^2/8 - (2\tau + 1)\ln 2)/(\tau + 1)^2 - 2\ln(I/m_0c^2) - \delta \quad (4.2)$$

depends on the kinetic energy in units of the rest mass $\tau = T/m_0c^2$, I , and a density-effect correction δ due to the dielectric polarization of the medium by the electrons [157, 158]. δ itself depends on I , τ , the plasma frequency of the medium ω_p and its phase. The stopping power of compounds may be estimated by application of the additivity rule [155, 159], which states that

$$\langle I \rangle = \exp \left(\left(\sum_j w_j (Z_j/A_j) \ln I_j \right) / \sum_j w_j (Z_j/A_j) \right), \quad (4.3)$$

where w_j , Z_j , A_j , and I_j are the weight fraction, atomic number, atomic weight and mean excitation energy of the j th constituent of the compound. With the values of I_j tabulated in Ref. [155] and corresponding errors, the stopping power of CuInSe₂ can now be calculated as

$$-\frac{dE}{dx} = (1.01 \pm 0.02) \text{ eV/nm}. \quad (4.4)$$

The density $\rho = 5.803 \text{ g/cm}^3$ was estimated by use of the lattice constants of the unit cell [17] and the weight of the atoms within the unit cell. The stopping powers of CuGaSe₂ and CuInS₂ are $(1.14 \pm 0.02) \text{ eV/nm}$ and $(1.23 \pm 0.02) \text{ eV/nm}$ respectively. The mass densities were calculated from lattice constants given in Refs. [18, 19]. The average energy loss of the beam electrons due to the interaction with a TEM specimen is negligible compared with their kinetic energy since the specimens have a total thickness of typically no more than 100 nm. It is therefore assumed that the local stopping power of the beam electrons within the specimen can be approximated by the initial stopping power given in Eq. (4.4). An average energy $E_{eh} = 2.1E_g + 1.3 \text{ eV}$ of a beam electron is needed to generate a free electron-hole pair in a semiconductor [152], where E_g is the band-gap energy (see Sec. 2.2.2). If the electron current-density j_e of the incident electron beam and the mean lifetimes $\tau_{e,h}$ of the generated free electrons and holes in the semiconductor is known, the mean densities of free electrons and holes in the semiconductor generated by the electron beam may be approximated by

$$n_{\text{gen}} = j_e \left(-\frac{dE}{dx} \right) \frac{\tau_e}{E_{eh}} \quad (4.5)$$

$$p_{\text{gen}} = j_e \left(-\frac{dE}{dx} \right) \frac{\tau_h}{E_{eh}}. \quad (4.6)$$

Lifetimes of minority carriers of about $\tau_e = 10 \text{ ns}$ have been detected in CuInSe₂ [160]. It is assumed here that the lifetimes τ_h of generated holes are in the same order of magnitude. By use of the highest electron current density that was applied during the acquisition of inline electron holography, $j_e \approx 3000 \text{ nm}^{-2}\text{s}^{-1}$, Eq. (4.6) yields $n_{\text{gen}} = p_{\text{gen}} \approx 8.6 \times 10^{15} \text{ cm}^{-3}$ in the case of CuInSe₂. If similar lifetimes are assumed for CuGaSe₂, this yields $n_{\text{gen}} = p_{\text{gen}} \approx 7.1 \times 10^{15} \text{ cm}^{-3}$. The carrier lifetimes in CuInS₂ absorbers are significantly smaller and do not exceed $\tau_{e,h} = 1 \text{ ns}$ [161]. The upper limit of the electron beam induced free

Table 4.2: Stopping power $-\frac{dE}{dx}$, estimated mean carrier lifetimes τ_e , τ_h , and upper limit n_{gen} , p_{gen} of the electron beam induced free charge-carrier density for an electron current density of $j_e \approx 3000 \text{ nm}^{-2}\text{s}^{-1}$ in the case of CuInSe₂, CuGaSe₂, and CuInS₂.

	$-\frac{dE}{dx}$ (eVnm ⁻¹)	τ_e , τ_h (ns)	n_{gen} , p_{gen} (cm ⁻³)
CuInSe ₂	1.01 ± 0.02	10	8.6×10^{15}
CuGaSe ₂	1.14 ± 0.02	10	7.1×10^{15}
CuInS ₂	1.23 ± 0.02	1	0.8×10^{15}

charge carrier density in CuInS₂ is then given by $n_{\text{gen}} = p_{\text{gen}} \approx 0.8 \times 10^{15} \text{ cm}^{-3}$. Tab. 4.2 shows the stopping power $-\frac{dE}{dx}$, the mean carrier lifetimes τ_e , τ_h and the upper limit of the electron beam induced free charge-carrier density n_{gen} , p_{gen} for the different materials. In the case of CuInSe₂ and CuGaSe₂, the values n_{gen} , p_{gen} are in the same order of magnitude as the doping density, in the case of CuInS₂, they are about two orders of magnitude smaller (see Tab. 4.3). In the following, these values are applied to estimate the possible influence of a redistribution of free charge carriers within the electronic bands on the averaged electrostatic potential $\Delta V_a(\vec{r})$. It should be pointed out that the actual induced free charge carrier density depends on the actual electron current density of the electron beam. This estimation corresponds to the upper limit of the applied electron current densities.

4.2.1.2 Redistribution of free charge carriers at grain boundaries as origin of potential wells

A redistribution of free charge carriers in the vicinity of charged grain boundaries is a possible origin of the measured potential wells. This issue is now illuminated. In order to estimate the contribution of a redistribution of free charge carriers to the potential wells, the MIP is assumed to be constant in the region of interest across the grain boundary, i.e., the composition as well as the atomic density do not change (see Eq. (3.21)). The potential wells measured by use of electron holography would then be caused by a change in $\Delta V_{\text{cr}}(\vec{r})$ alone.

Then, according to Poisson's equation (Eq. (3.25)), the positive curvature at the bottom of the potential wells implies that negative charge is located at the grain boundary core, which is screened by positively charged layers on either side. The positive charge layers would

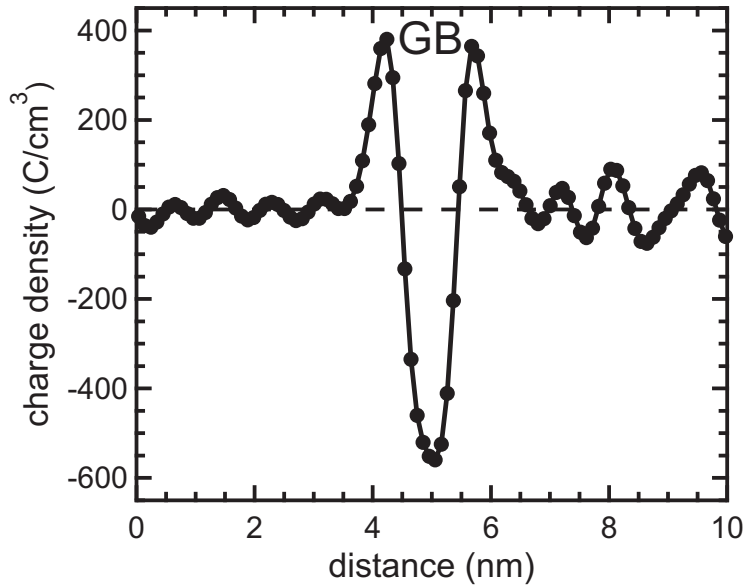


Figure 4.10: The charge density determined from the potential well measured at a grain boundary in CuInS₂, which is shown as the black curve in Fig. 4.5, by use of Poisson's equation under the assumption of a constant MIP at the grain boundary. A relative permittivity of $\epsilon_r = 10.2$ was assumed for CuInS₂ [162]. The configuration in which negative charge located at the grain boundary is screened by an excess charge layer of free holes possibly explains the existence of the measured potential wells. The strong fluctuations in the grain interiors arise due to the computation of the second derivative of the averaged electrostatic potential profile, which amplifies the fluctuations and noise in the potential profile.

arise from an accumulation of free holes, which are majority charge carriers within the grain interiors of polycrystalline Cu(In,Ga)(Se,S)₂ thin films (see Fig. 4.9). This is illustrated in Fig. 4.10, which shows the excess charge density calculated from the potential well shown as the black curve in Fig. 4.5, by use of Poisson's equation and by assuming a constant MIP at the grain boundary. A relative permittivity of $\epsilon_r^{\text{CuInS}_2} = 10.2$ was assumed for CuInS₂ [162].

In a doped semiconductor, the redistribution of free charge carriers in the electronic bands, owing to an electric field generated by an isolated excess charge, depends in a complicated manner on the physical properties of the semiconductor and its temperature. Under certain assumptions, the simplified model of an isolated negatively charged plane at the surface of a homogeneously *p*-doped semiconductor can be computed in the framework of the continuum model in order to estimate resulting potential distributions within the Cu(In,Ga)(Se,S)₂

Table 4.3: Representative doping densities N_A [25, 26], relative permittivities ϵ_r [162, 163], and calculated Debye lengths L_D of CuInSe₂ and CuInS₂.

	N_A (cm ⁻³)	ϵ_r	L_D (nm)
CuInSe ₂	1×10^{16}	11.3	40
CuInS ₂	1×10^{17}	10.2	12

thin films. The continuum model requires that the typical length scale on which changes in the potential occur, i.e., screening lengths, are larger than atomic distances³.

Analytical estimation of typical screening lengths under the assumption of quasi-neutrality

The one-dimensional potential $V(x)$ in the semiconductor, where the x axis is oriented perpendicularly to the charged plane, can be calculated analytically, if only the majority carrier density is considered and quasi-neutrality is assumed, i.e., $\Delta V(x)_{\max} \ll kT$, where $\Delta V(x)_{\max}$ is the maximum potential difference, k the Boltzmann constant, and T the temperature. The position of the charged plane is chosen as $x = 0$, and the zero point of $V(x)$ is chosen far away from the charged plane, where $V(x)$ is flat (see Fig. 4.9). It is further assumed that the Maxwell-Boltzmann distribution approximates the energetic distribution of free holes. The potential $V(x)$ close to the charged plane can then be described by an exponential function [151]

$$V(x) = -V(x = 0) \exp(-|x|/L_D), \quad (4.7)$$

where $L_D = \sqrt{\epsilon_r kT/e^2 N_A}$ is the so called Debye length, and N_A is the doping density. Tab. 4.3 shows calculated values of L_D for CuInSe₂ (which is representative for all Cu(In,Ga)Se₂ absorbers) and CuInS₂ thin film solar cell absorbers. The parameters N_A and ϵ_r were taken from Refs. [25, 26, 162, 163].

In contrast to the Debye lengths given in Tab. 4.3, the typical distance from the grain boundary core at which the modulus of the averaged electrostatic potential falls to $1/e$ times the modulus of the potential well depth is about 1 nm in the measurements (see

³This model might not necessarily be applicable since the FWHM of the measured potential wells is in the order of the interatomic distances

Fig. 4.1). Therefore, the experimentally observed attenuation of the potential well occurs on a length scale, which is at least one order of magnitude lower than expected from the calculated Debye lengths. The estimation given above therefore indicates that the potential wells measured at grain boundaries in Cu(In,Ga)Se₂ and CuInS₂ can not be caused solely by a redistribution of free holes within the valence band screening the electric field of a negatively charged grain-boundary core.

Estimation of potential distributions by use of numerical simulations

For a more precise estimation, the generation of free charge carriers is considered and the constraint of quasi-neutrality is omitted. Fig. 4.11(a) shows numerically simulated changes in the averaged electrostatic potential profiles across grain boundaries in CuInSe₂ and CuInS₂ with and without considering the generation of a free charge carrier density of $1 \times 10^{16} \text{ cm}^{-3}$ by the electron beam, under the assumption of a constant MIP at the grain boundaries.

The one-dimensional simulations were performed by use of the computer program SCAPS [164]. SCAPS numerically solves the one-dimensional continuity equation and Poisson's equation for a given initial problem. It does that on the basis of the electronic band diagram, where the occupation of the electronic states is determined by the effective density of states and the probability of occupation of these states [165], which is approximated by the Maxwell-Boltzmann statistics⁴. Any band discontinuities at the grain boundaries were neglected for the simulations, since they can only be evoked by a change in the local structure, which is related with a change in the MIP. Then, the averaged electrostatic potential shown in Fig. 4.11(a) is proportional to $-E_c/e$ and $-E_v/e$ shown in Fig. 4.11(b). For the simulations shown in Fig. 4.11, an excess charge density of $e \cdot 1 \times 10^{12} \text{ cm}^{-2}$ was assumed to be bound at the grain boundaries. The excess charge was implemented through an areal density of acceptors of $1 \times 10^{12} \text{ cm}^{-2}$ with an energetic level just above the valence-band edge and well below the Fermi level. This ensured that all acceptors were ionized in the framework of this simulation and thus charged. The doping densities and permittivities given in Tab. 4.3 were considered for the grain interiors. Mean charge-carrier lifetimes in the grain interiors of 10 ns were assumed. The upper limit of the generation rate of free charge carriers by the electron beam $1 \times 10^{24} \text{ s}^{-1} \text{ cm}^{-3}$, was chosen such that the

⁴The Maxwell-Boltzmann statistics is a good approximation of the Fermi-Dirac statistics for electronic states that are far away from the Fermi level.

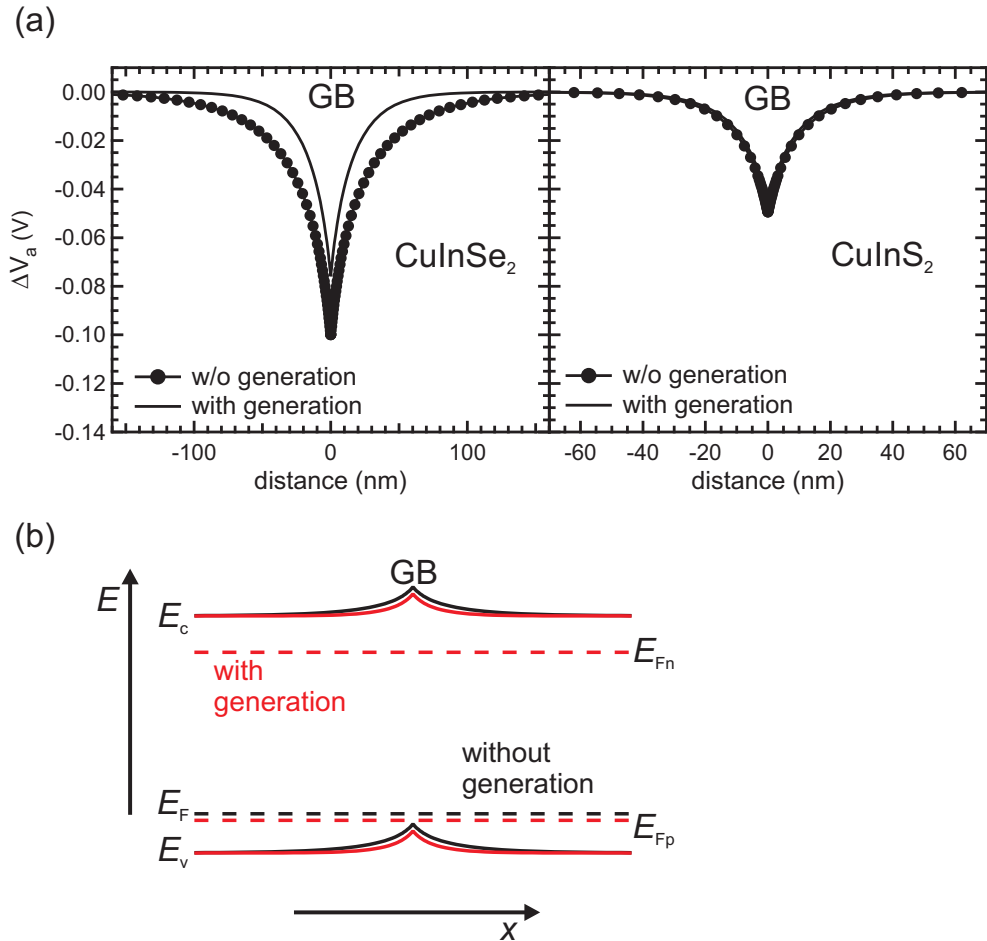


Figure 4.11: (a) Simulated averaged electrostatic potential profiles across grain boundaries in CuInSe_2 and CuInS_2 , for a constant MIP at the grain boundaries at $T = 300\text{ K}$. An excess charge density of $-e \cdot 1 \times 10^{12} \text{ cm}^{-2}$ was applied at the grain boundaries. Free charge carrier lifetimes, doping densities in the grain interiors and the generation of free charge carriers have been chosen in accordance with Tab. 4.3 and Tab. 4.2. The mean free charge carrier densities generated by the electron beam, if considered, was $1 \times 10^{16} \text{ cm}^{-3}$. (b) Schematic of the corresponding electronic band diagrams, which have been simulated by use of SCAPS to determine the averaged electrostatic potential shown in (a). The latter is proportional to $-E_c/e$. E_{Fn} and E_{Fp} denote the quasi Fermi levels for electrons and holes.

average density of generated free charge carriers was $1 \times 10^{16} \text{ cm}^{-3}$, in accordance with Tab. 4.2. Since the induced free charge-carrier densities are smaller in CuInS_2 (see Tab. 4.2), the free charge-carrier density in the simulation serves as an upper limit. Note that the dimensions of the potential wells also depend on the effective densities of states N_v , N_c

in the valence and conduction band. They were chosen as $N_c = N_v = 2 \times 10^{18} \text{ cm}^{-3}$. An enhanced recombination of free charge carriers at the grain boundary was neglected for this simulation.

As a result of the generation of free charge carriers by the electron beam, the probability of occupation of electronic states can not be described by one Fermi distribution anymore, but requires the formalism of quasi Fermi distributions [5], one quasi Fermi distribution for holes E_{Fp} and one for electrons E_{Fn} . Note that, with the applied set of parameters, an excess charge density higher than about $e \cdot 1 \times 10^{12} \text{ cm}^{-2}$ led to an intersection of the valence band and the Fermi level (or the quasi Fermi level of holes) at the grain boundary (see Fig. 4.11(b)). This means that the grain boundary becomes a conductor. However, this situation can not be simulated correctly, for the Maxwell-Boltzmann statistics is not a suitable approximation anymore and the screening depends strongly on the exact density of states in the valence band. Hence, the simulations are not reliable anymore. However, a metallic behavior of grain boundaries within CuInSe₂ and CuInS₂ thin films has not been found, neither in equilibrium nor under illumination. It is therefore assumed that the corresponding lowering of the averaged electrostatic potential at grain boundaries is smaller than the energy difference between the Fermi level and the valence-band maximum. This difference may be few hundred meV in the investigated semiconductors. This is illustrated in Fig. 4.11(a). For a bound excess charge density of $e \cdot 1 \times 10^{12} \text{ cm}^{-2}$ at the grain boundary, the resulting potential-well depths are at most -0.11 V , which is negligible compared with the typically measured depths of $-(1 - 3) \text{ V}$. Even if the distance between the Fermi level and the valence-band maximum is a few hundred meV, this can not lead to potential well depths of a few V.

It can be seen from Fig. 4.11 that even if the generation of free charge carriers is taken into account, the screening lengths, i.e., the distance on which the modulus of the averaged electrostatic potential falls to $1/e$ of its maximum, in CuInSe₂ and CuInS₂ are larger than 1 nm. In the case of CuInS₂, the screening length is about 10 nm, regardless whether free charge-carrier generation was considered or not, and in the case of CuInSe₂ it is 18 nm and 24 nm with and without considering the generation of free charge carriers. A comparison with the previous estimation shows that the assumption of quasi-neutrality was a tolerable approximation, also in the case of CuInSe₂, which has a smaller doping density compared with CuInS₂. The length scales, on which a redistribution of free charge carriers screens the electric field of a bound excess charge at a grain boundary, was found to be larger

than 10 nm for all considered cases. Since this corresponds to a few unit cell lengths, the continuum model is assumed to be applicable for the previous estimations.

By increasing the doping density in the grain interiors, it is possible to simulate smaller screening lengths, however, this leads to a reduction of the potential-well depths at the same time. In addition, the Fermi level moves closer to the valence-band maximum leaving even less tolerance for an upward bending of the bands. Hence, it is not possible to simulate the shape of the potential distributions as they were measured.

In summary, it is very unlikely that a local redistribution of free charge carriers in the grain interiors, screening the electric field caused by a negative excess charge bound at the grain boundary cores, contributes significantly to the width and the depth of the measured potential wells.

4.2.1.3 Potential barriers or wells below the detection limit

Excess charges bound at grain boundaries give rise to adjacent space-charge or excess charge layers (see Fig. 4.9), which were found to have a significant impact on the electrical properties of a polycrystalline material [79]. For the grain boundary models presented in Sec. 2.3.2 comprise space charge regions, it is of great interest to know the magnitude of the associated bending of the bands in the electronic band diagram. This issue is discussed in the following.

Besides negative excess charge at grain boundaries (see Sec. 4.2.1.2), a negative space-charge region screening the electric field of a positive excess charge bound at the grain boundary core is a possible scenario, but would result in a potential barrier and thus, is not compatible with the results. However, it can not be excluded from the presented results that a corresponding potential barrier (or well) smaller than the detection limit of the method is present and superimposes the measured potential wells. The magnitude of such a potential barrier (or well) is now estimated. This is done with and without consideration of the estimated free charge carrier density induced by the electron beam (Tab. 4.3) since the actual values are expected to be somewhere in between, depending on the actually applied electron current density of the beam. The following estimation will be of use in Sec. 4.2.2, where the electrostatic contribution to the strain that may be caused by corresponding potential distributions below the detection limit is estimated.

Potential barriers below the detection limit without consideration of free charge carrier generation by the electron beam

At first, the generation of free charge carriers by the electron beam is neglected. According to the depletion approximation for space-charge layers [150, 166], the density of free holes in the depletion layer is zero and the potential increases with the square of the distance x towards the grain boundary, which is located at $x = 0$ (see also Fig. 4.9). If the zero point of the potential is chosen far away from the grain boundary, the potential is given by

$$V(x) = a(|x| - w)^2, \quad (4.8)$$

where $a = eN_A/2\epsilon$, and w is the space-charge region width on one side of the grain boundary. Due to overall charge neutrality, the width is given by

$$w = \frac{N_i}{2N_A}, \quad (4.9)$$

where N_i is the bound interfacial charge carrier density. The strongest potential increase is therefore expected close to the grain boundary. A potential barrier should be detectable by means of inline electron holography if the increase in potential in a $l_{\text{eff}} = 20$ nm wide region at the grain boundary core (this distance corresponds to the smallest retrievable spatial frequency) exceeds $V_{l_{\text{eff}}} = 0.1$ V, which was found as the detection limit. According to Eq. (4.8), this leads to a minimum detectable potential barrier

$$V_{\min} = \frac{e(V_{l_{\text{eff}}}/a + l_{\text{eff}}^2)^2 N_A}{8\epsilon l_{\text{eff}}^2}. \quad (4.10)$$

In the case of CuInSe₂ ($N_A = 1 \times 10^{16}$ cm⁻³, $\epsilon_r = 11.3$) a potential barrier should be detectable if the total potential barrier is higher than $V_{\min} \approx 0.83$ V. By solving Eq. (4.8) for N_i at $x = 0$, it can be seen that this potential barrier corresponds to a bound charge-carrier density at the grain boundary of $N_i = 6.5 \times 10^{11}$ cm⁻². The values V_{\min} and N_i , also for CuInS₂, are summarized in Tab. 4.4.

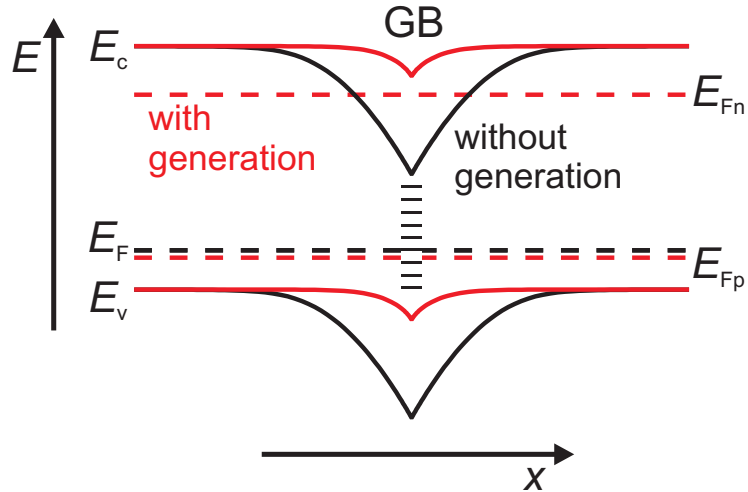


Figure 4.12: Electronic band diagram illustrating the screening of the electric field, which is caused by positive excess charges bound at a grain boundary (GB). Apart from a constant value, the electrostatic potential is proportional to $-e \cdot E_c$. Black color denotes the case, for which the generation of free charge carriers is neglected and red color denotes the case, for which the generation of free charge carriers is considered. In the latter, E_{Fn} and E_{Fp} denote the quasi Fermi levels for electrons and holes. The excess charge density at the grain boundary is the same in both cases. Electronic defect states within the band gap at the grain boundary are denoted by dashes. The probability of occupation of the defect states between the quasi Fermi levels is governed by the kinetics of the generation and recombination processes [5, 167].

Potential barriers below the detection limit with consideration of free charge carrier generation by the electron beam

It has to be considered that the electron beam may perturb the potential distribution to be measured. An accumulation of free electrons, generated by the electron beam, may screen a positive excess charge bound at the grain boundaries more effectively than space charge. Apart from the polarity, this situation is similar to the screening of a negative bound excess charge at a grain boundary by free holes shown in Fig. 4.9. In addition, a generation of free charge carriers by the electron beam affects the probability of occupation of the electronic states within the valence and conduction band via the quasi Fermi levels. In this case, the occupation of electronic defect states between the two quasi Fermi levels is governed by the kinetics of the non radiative recombination and generation of free charge carriers [167]. Hence, the bound excess charge density N_i , which is present during the measurement, is not necessarily the same as in equilibrium. An electronic band diagram in

Fig. 4.12 illustrates the situation. In analogy to the case of negative excess charge bound at a grain boundary (see Sec. 4.2.1.2), it has to be taken care that the conduction-band minimum does not intersect the quasi Fermi level of electrons since this would lead to a conductive behavior of the grain boundary. For the estimations below, it is assumed that the conduction-band minimum and the valence-band maximum do not intersect any Fermi or quasi Fermi level.

The estimations are again based on the assumption of quasi-neutrality. This seems justified since no significant potential distribution was detected in a 20 nm wide region at the grain boundaries in all potential profiles determined by use of inline electron holography.

Suppose the situation during the measurement with consideration of free charge carrier generation by the electron beam. It is assumed that all generated free charge carriers are mobile enough to take part in the redistribution of free charge carriers screening the electric field of the bound grain boundary charge before they recombine. The charge distribution close to the grain boundary is therefore not affected by the mean lifetime of the free charge carriers. If screening due to space charge is effectively neglected, the attenuation of the averaged electrostatic potential due to the screening of the positive excess charge at the grain boundary by generated free electrons can then be described with the help of an exponential function and the Debye length L_D (see Eq. (4.7)). As estimated in Sec. 4.2.1.1, the generated free electron density in CuInSe₂ absorbers (which again is a representative for all Cu(In,Ga)Se₂ absorbers) is not expected to exceed a density of $1 \times 10^{16} \text{ cm}^{-3}$. In CuInS₂, the electron beam induced free charge-carrier density is expected to be smaller than $1 \times 10^{15} \text{ cm}^{-3}$. These free charge carrier densities determine the Debye lengths L_D^{eb} modified by the electron beam. They are given in Tab. 4.4. Note that these Debye lengths are lower limits, since the applied free charge-carrier densities are upper limits.

Potential barriers, for which the increase of the averaged electrostatic potential within a distance of $l_{\text{eff}} = 20 \text{ nm}$ from the grain boundary core is smaller than the detection limit of $V_{l_{\text{eff}}} = 0.1 \text{ V}$ are not detectable. For an exponential increase, this is the case if the total potential barrier is not larger than (see Eq. (4.7))

$$V_{\min}^{\text{eb}} = \frac{V_{l_{\text{eff}}}}{1 - \exp(-l_{\text{eff}}/L_D^{\text{eb}})}. \quad (4.11)$$

By use of Poisson's equation and the condition of charge neutrality, the corresponding interfacial charge density at the grain boundary core can then be calculated by

Table 4.4: Debye length, L_D^{eb} modified due to the generation of free charge carriers by the electron beam, the corresponding minimum detectable potential barrier height or potential well depth V_{min}^{eb} , and bound areal charge carrier density N_i^{eb} at the grain boundary for the two cases of charge of positive and negative polarity at the grain boundary. The shown Debye lengths are lower limits and hence the resulting $|V_{min}^{eb}|$ upper limits. V_{min} and N_i are the corresponding values if the generation of free charge carriers by the electron beam is neglected.

	CuInSe ₂		CuInS ₂	
polarity	positive	negative	positive	negative
L_D^{eb} (nm)	40	28	121	12
V_{min}^{eb} (V)	0.25	-0.20	0.66	-0.12
N_i^{eb} (cm ⁻²)	7.9×10^{11}	8.8×10^{11}	6.1×10^{11}	1.2×10^{12}
V_{min} (V)	0.83	-0.25	0.13	-0.12
N_i (cm ⁻²)	6.5×10^{11}	7.9×10^{11}	7.6×10^{11} cm ⁻²	1.2×10^{12}

$$N_i^{eb} = \int_0^\infty \frac{2\epsilon V_{min}^{eb}}{e L_D^{eb}{}^2} \exp(-x/L_D^{eb}) dx. \quad (4.12)$$

Corresponding values for CuInSe₂ and CuInS₂ are given in Tab. 4.4.

Potential wells below the detection limit with and without consideration of free charge carrier generation by the electron beam

The same estimations can be performed in the case of negative excess charge bound at grain boundaries, whose electric field is screened by free charge carriers. Apart from a switch in polarity, this situation can be treated analogously. Only in this case, the free charge carrier density is either given by the free charge carrier density originating from the doping (see Tab. 4.3), or the sum of the free charge carrier density originating from the doping and the one induced by the electron beam. L_D^{eb} , V_{min}^{eb} , and N_i^{eb} and the values of V_{min} , and N_i without consideration of the generation of free charge carriers are given in Tab. 4.4.

The smaller the free charge carrier density in the grain interior, the smaller the values of N_i that are compatible with the measurement results. This can be seen in Fig. 4.13, where the minimum detectable bound grain-boundary charge-carrier density N_i is plotted versus the Debye length for different values of V_{eff} and l_{eff} . The values of both parameters were estimated for the performed measurements, however, depend in general on the exact

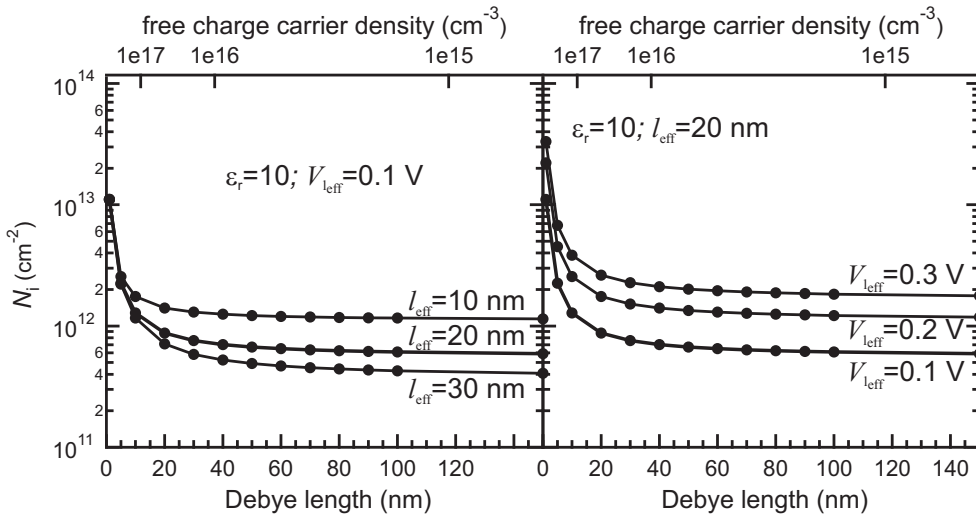


Figure 4.13: Minimum detectable bound grain boundary charge-carrier density N_i as function of the Debye length L_D or, equivalently, the free charge carrier density for a constant relative permittivity of $\epsilon_r = 10$, if the screening through space charge is neglected. The left graph shows a variation of $l_{\text{eff}} = 10, 20, 30 \text{ nm}$ for a constant $|V_{\text{eff}}| = 0.1 \text{ V}$, the right graph a variation of $|V_{\text{eff}}| = 0.1, 0.2, 0.3 \text{ V}$ for constant $l_{\text{eff}} = 20 \text{ nm}$. Note that this estimation is applicable for positive or negative charges at the grain boundary.

measurement conditions, i.e., maximum defocus value, image acquisition time, specimen roughness, etc. The figure is therefore useful to estimate the detection limit of N_i with respect to a change of these parameters. Fig. 4.13 also states that even if V_{eff} and l_{eff} are varied as 0.1, 0.2, 0.3 V and as 10, 20, 30 nm respectively, N_i is not expected to exceed $1 \times 10^{12} \text{ cm}^{-2}$ significantly, as long as the free charge carrier density is $1 \times 10^{17} \text{ cm}^{-3}$ or smaller. Below $1 \times 10^{16} \text{ cm}^{-3}$, N_i is almost independent of the free charge carrier density. Note that N_i is independent on the polarity of the bound charge density. Fig. 4.13 also implies that either V_{eff} has to be reduced significantly or l_{eff} has to be increased, in order to reduce the detection limit below $N_i = 1 \times 10^{11} \text{ cm}^{-2}$.

Tab. 4.4 compares the values of $V_{\text{min}}^{\text{eb}}$ with the corresponding values V_{min} if the generation of free charge carriers by the electron beam is not taken into account. Note that V_{min} is smaller than $V_{\text{min}}^{\text{eb}}$ in the case of CuInS₂ with positively charged grain boundaries since the high density of negatively charged acceptors, $N_A = 1 \times 10^{17} \text{ cm}^{-3}$, screens the electric field of the bound grain boundary charge more effectively than the smaller generated free charge carrier density of $1 \times 10^{15} \text{ cm}^{-3}$. The previous assumption that the screening by a space charge region can be neglected compared with the screening by free charge carriers

is therefore not applicable in this case. The screening with and without consideration of the generation of free charge carriers by the electron beam is then governed by an adjacent space charge region. This has to be considered also in Fig. 4.13, which is only valid if the doping density N_A is smaller than the free charge carrier density.

For the sake of completeness, it should be noted that potential barriers and wells that were numerically simulated, with the parameters given in Sec. 4.2.1.2, for a bound excess charge carrier density of $N_i = 1 \times 10^{12} \text{ cm}^{-2}$ at grain boundaries are smaller than the detection limit. This can already be seen in Fig. 4.11(a).

In summary, potential barriers or wells with total heights or depths between the values V_{\min}^{eb} and V_{\min} given in Tab. 4.4 are compatible with the presented results. Unfortunately, this estimation is only valid during the measurement since the bound excess charge density at grain boundaries may change significantly under electron beam irradiation. Only if the perturbation of the electron beam is negligible, e.g. at very low electron current densities of the incident electron beam, the values V_{\min} (see Tab. 4.4) give an upper estimate of potential barrier heights or well depths that are present at grain boundaries in equilibrium. This can be transferred to the band bending of conduction and valence band by multiplication with $-e$. Nevertheless, this estimation is helpful for the following estimation on the contribution to a strain that may be caused by potential barriers or wells below the detection limit in Sec. 4.2.2. Such a strain can affect the MIP and hence contribute to the measured potential wells.

4.2.2 Electrostatic contribution to the strain at grain boundaries

Apart from $\Delta V_{\text{cr}}(\vec{r})$, a possible contribution to the measured potential wells at grain boundaries is a local change in $\text{MIP}(\vec{r})$. It is clear from Eq. (3.21) that this can either be evoked by a (local) modification of *vol*, i.e., local distortions owing to stress, or by a modification of the local composition, which affects the local Coulomb potential $V(\vec{r}_{3d})$ and to some extent *vol*. This section covers the electrostatic contribution of space-charge or excess charge layers below the detection limit to a strain that may be present at grain boundaries, i.e., a local modification in *vol*. In order to study the effect of changes in $\text{MIP}(\vec{r})$ on $\Delta V_a(\vec{r})$, any free charge carrier redistribution causing a measurable contribution to $\Delta V_a(\vec{r})$ is neglected in the following, hence $\Delta V_{\text{cr}}(\vec{r}) \approx 0$.

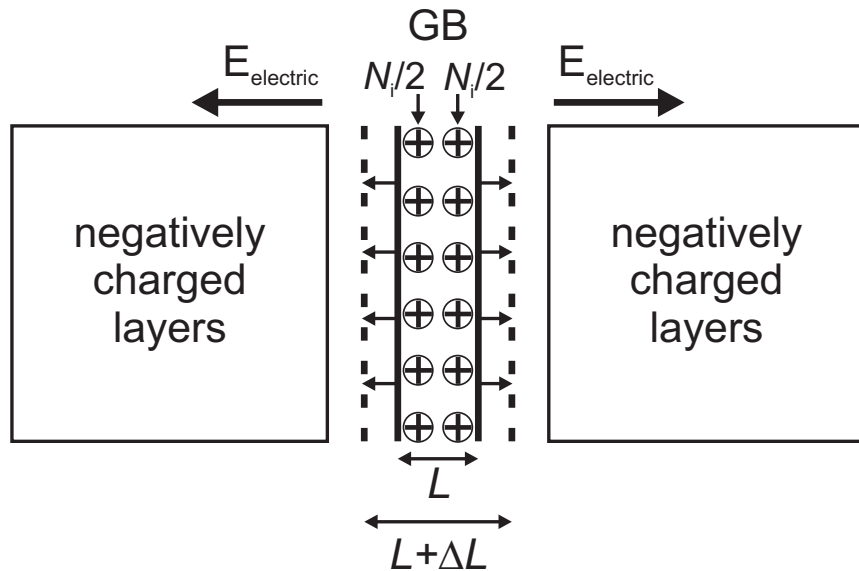


Figure 4.14: Simplified model of a strain at a grain boundary (GB) caused by the attraction of positive excess charges bound at the grain boundary core and adjacent negatively charged layers, which are spatially fixed. In this model, it is assumed that each half of the bound charge carrier density at the grain boundary is attracted to one direction and that the two halves are spatially separated by a lattice constant L . Due to the overall charge neutrality, the projected charge carrier density of each one of the negatively charged layers must be equal to $N_i/2$. In general, the excess charge at the grain boundary may be spatially distributed and not localized to two planes.

Estimation of the strain which is required to induce the measured potential wells

First, the strain which would be necessary to explain the measured potential wells is estimated. For that purpose, consider the illustration in Fig. 4.14. Suppose the MIP is constant in the grain interiors more than ~ 2 nm away from the grain boundary core, and the occupation of the respective lattice sites (composition) does not change at the grain boundary. It is further assumed that the grain boundary is a planar defect parallel to the incident electron beam. Due to the symmetry, one may assume that any local distortion of the unit cell of the crystal lattice parallel to the plane of the grain boundary is negligible or zero in average. Then, a local change in the unit-cell volume caused by an elongation along the x axis, normal to the plane of the grain boundary, would according to Eq. (3.21) result in a decrease of the local MIP(\vec{r}). The origin of such an elongation may be a strain normal to the plane of the grain boundary, which is defined by $\kappa = \Delta L/L$, where ΔL is

the local change in the lattice constant L perpendicular to the plane of the grain boundary. The local MIP at the grain boundary can now be expressed by

$$\text{MIP}_{\text{gb}} = \text{MIP}_{\text{gi}} + \Delta V_{\text{a,max}} = \frac{L}{L + \Delta L} \text{MIP}_{\text{gi}}, \quad (4.13)$$

where MIP_{gi} is the MIP in the grain interiors, and $\Delta V_{\text{a,max}}$ the measured potential well depth at the grain boundary. The local strain of the crystal lattice normal to the plane of the grain boundary, which is necessary to explain the measured potential well depth, can then be estimated to be

$$\kappa = -\frac{\Delta V_{\text{a,max}}}{\text{MIP}_{\text{gi}} + \Delta V_{\text{a,max}}}. \quad (4.14)$$

Hence, a potential well depth of about $\Delta V_{\text{a,max}} = -1.76 \text{ V}$ and $\text{MIP}_{\text{gi}} = 14.0 \text{ V}$, as found in the case of CuInSe_2 , would necessitate a strain of $\kappa = 0.14$.

Estimation of the strain which may be caused by potential distributions below the detection limit

Space-charge or excess-charge layers adjacent to a bound charge of opposite polarity give rise to strain, since charges of opposite polarity attract each other (see Fig. 4.14). The strain that can be induced by such a constellation is estimated in the following and compared with the estimation above. Suppose the grain-boundary can be well described by the model in Fig. 4.14, i.e., there is a bound charge density eN_i at its core and space charge or excess charge layers attenuate the electrostatic potential on either side. As a result, there is an electrostatic force acting on the bound charges at the grain boundary pulling them to the charged layers of opposite polarity on either side of the grain boundary. The force per area on the bound charge density is the stress $\sigma_{\text{el}}(0)$, which strains the lattice at the grain boundary core depending on the stiffness of the lattice, i.e., its Young's modulus Y . If the model in Fig. 4.14 is considered for $\Delta L \ll L$, i.e., the displacements of the lattice planes are small, Hooke's law [168] may be applied to express the strain by

$$\kappa(0) = \frac{\sigma_{\text{el}}(0)}{Y} = \frac{eN_i|E_{\text{electric}}(0)|}{Y}, \quad (4.15)$$

where $E_{\text{electric}}(0)$ is the electric field at $x = 0$. Note that the attraction of each half of N_i to one side accounts for half of this strain.

Estimation of the strain which may be caused by a space charge region below the detection limit

First, the free charge carrier generation by the electron beam is neglected. In the case of a positive bound charge at the grain boundary, a negative space-charge region screens the resulting potential according to Eq. (4.8). The electric field at $x = 0$ coming from negative x values is given by $E_{\text{electric}}(0) = -\nabla_r V_a(\vec{r})|_{x=0^-} = -2aw$. The modulus of this value is equal to the modulus of the electric field at $x = 0$ coming from positive x values. By use of Eq. (4.9), this yields

$$\kappa(0) = \frac{e^2 N_i^2}{2Y\epsilon}. \quad (4.16)$$

In Sec. 4.2.1.3, it was concluded that a potential barrier smaller than the detection limit of inline electron holography may be present at grain boundaries within CuInSe₂ and CuInS₂. The corresponding bound charge carrier density at the grain boundary was estimated to be smaller than $N_i < 1 \times 10^{12} \text{ cm}^{-2}$ (see Tab. 4.4). Applying Young's modulus $Y = 6.49 \times 10^{10} \text{ Nm}^{-2}$ [169] of CuInSe₂ for both materials, results in a strain of $\kappa(0) < 2 \times 10^{-7}$. This is several orders of magnitude smaller than $\kappa = 0.14$, which is required to explain the potential-well depths (see Eq. (4.14)). Even a bound charge carrier density of $1 \times 10^{14} \text{ cm}^{-2}$ at the grain boundary core results in a strain of less than $\kappa(0) < 0.002$.

Estimation of the strain which may be caused by an accumulation of free charge carriers at a charged grain boundary

In the case of an excess charge bound at a grain boundary, an excess charge layer of free charge carriers of opposite polarity may screen the resulting potential according to Eq. (4.7). Then, the strain is given by

$$\kappa(0) = \frac{eN_i V_{\min}}{YL_D}. \quad (4.17)$$

Even if the generation of free charge carriers by the electron beam is included ($V_{\min} = V_{\min}^{\text{eb}}$), Eq. (4.17) with the values from Tab. 4.4 results in $\kappa(0) = 1.5 \times 10^{-7}$ in the case of CuInSe₂ ($L_D^{\text{eb}} = 28 \text{ nm}$), and $\kappa(0) = 3 \times 10^{-7}$ in the case of CuInS₂ ($L_D^{\text{eb}} = 12 \text{ nm}$). Again, this is much smaller than required. If the generation of free charge carriers is considered in the case of a positive charge density at the grain boundary, the contribution to the strain is

similarly small.

If the condition of quasi-neutrality is omitted, $|E_{\text{electric}}(0)|$ can be determined from the slope of the potential distributions that were numerically simulated for the estimation given in Sec. 4.2.1.2. For $N_i = 1 \times 10^{12} \text{ cm}^{-2}$, it is found that $|E_{\text{electric}}(0)| = 5.7 \times 10^6 \text{ Vm}^{-1}$ in the case of CuInSe₂ and $|E_{\text{electric}}(0)| = 5.9 \times 10^6 \text{ Vm}^{-1}$ in the case of CuInS₂. This leads to corresponding strains of $\kappa(0) \approx 1 \times 10^{-6}$ (CuInSe₂) and $\kappa(0) \approx 1 \times 10^{-6}$ (CuInS₂). These values are also much smaller than the strain required to induce potential wells with a depth of a few V.

The values of the strain computed for potential distributions below the detection limit are all equal or smaller than 10^{-6} . The previous assumption $\Delta L \ll L$ (see Eq. (4.15)) seems therefore justified. It is therefore concluded that the electrostatic contribution to the strain does not have a significant impact on the measured potential wells at grain boundaries. Note, however, that strain caused by local lattice distortions on a distance of few atomic layers from the grain boundary core can not be ruled out from this estimation. DFT calculation are required to estimate this contribution to the strain.

4.2.3 Local change in composition and ionicity at grain boundaries

A change in the local composition at grain boundaries may also be responsible for or contribute to the experimentally detected potential wells. This issue is discussed in the following.

The MIP of a crystalline material can be roughly estimated by use of the formula [170]

$$\text{MIP} = \frac{\hbar^2}{2\pi me\Omega} \sum_j n_j f_j^{\text{el}}(0), \quad (4.18)$$

where Ω is the volume of the unit cell, n_j is the number of atoms or ions of type j within the unit cell, and $f_j^{\text{el}}(0)$ are the respective atomic or ionic scattering factors in forward direction. An approximation of the MIP by use of Eq. (4.18) neglects any charge redistributions of electrons due to bonding between atoms or ions. However, Eq. (4.18) will be applied in the following in order to estimate the MIP of the investigated absorber materials as well as compositional changes at grain boundaries. Even if the estimated values of the MIPs are not accurate, trends in the change of the MIP upon compositional

Table 4.5: Electron scattering factors in forward direction $f^{\text{el}}(0)$ for the neutral atoms Cu, In, Ga, Se, S, Na, O, and corresponding ions according to Refs. [171, 172], in units of nm. The scattering factors of Se²⁻ and S²⁻ were not found in the literature.

	neutral atom	ion
Cu and Cu ⁺	0.629	0.329
In and In ³⁺	1.06	0.430
Ga and Ga ³⁺	0.714	0.243
Se	0.727	
S	0.516	
Na and Na ⁺	0.474	0.113
O and O ²⁻	0.198	0.410

changes are assumed to be reflected correctly.

Required atomic and ionic scattering factors in forward direction can be found in Refs. [170–174]. The scattering factors relevant for this work are given in Tab. 4.5. In general, the atoms in a crystal show a degree of ionicity ζ between the neutral atom and the ion. The corresponding scattering factors can be calculated according to [172]

$$f^{\text{el}}(0) = (1 - \zeta)f_{\text{neutral}}^{\text{el}}(0) + \zeta f_{\text{ion}}^{\text{el}}(0), \quad (4.19)$$

where $f_{\text{neutral}}^{\text{el}}(0)$, and $f_{\text{ion}}^{\text{el}}(0)$ are the scattering factors of the neutral atom and the corresponding ion.

Tab. 4.6 shows MIPs of CuInSe₂, CuGaSe₂, CuIn₃Se₅, CuGa₃Se₅, and CuInS₂ calculated by use of Eq. (4.18) with the scattering factors of neutral atoms. The required volumes Ω were calculated by use of the lattice constants given in Refs. [17–19, 175, 176] and are also applied in the following. The estimated value of the MIP of CuInSe₂, 15.51, is in agreement with the measured value of (14.0 ± 1.6) V.

Considering the potential wells, there are several ways according to Eq. (4.18) to induce a reduction of the MIP by a change in composition. The most prominent ones are vacancies of any kind, i.e., reducing the number of atoms in the unit cell. A substitution of atoms or ions for respective atoms or ions with smaller $f_{\text{el}}(0)$ also reduces the MIP. However, it has to be taken care of the fact that the unit cell volume may change with a significant amount of substitutions. Instead of trying to take account of all local changes in composition that may cause the potential wells, the matter will be discussed in detail in Sec. 4.4 with respect to the measurements on local composition changes at grain boundaries. It is clear from

Table 4.6: MIPs of the phases CuInSe₂, CuGaSe₂, CuIn₃Se₅, CuGa₃Se₅, and CuInS₂ calculated by use of the electron scattering factors for neutral atoms given in Tab. 4.5. The volumes of the unit cells Ω were determined from the lattice constants given in Refs. [17–19, 175, 177].

	MIP V
CuInSe ₂	15.51
CuGaSe ₂	15.40
CuIn ₃ Se ₅	14.91
CuGa ₃ Se ₅	14.77
CuInS ₂	15.38

Tab. 4.6, however, that the depth of the measured potential wells at grain boundaries of up to 3 V can not be explained by the presence of one of the other considered phases since all their MIPs are similar. Please note that a direct correlation between the measured changes in the averaged electrostatic potential at grain boundaries and an estimated change in composition by use of Eq. (4.18) is a simplification. This is because Eq. (4.18) involves the unit-cell volume Ω , whereas the changes in the potential may occur on length scales smaller than the unit cell size. This correlation is only justified if the values of the measured changes in the averaged electrostatic potential correspond to a value that is averaged over many atoms parallel to the plane of the grain boundary representing the local composition.

The large differences in the scattering factors of neutral atoms and ions indicate that a local change in ionicity of the atomic bonds at grain boundaries may be responsible for the presence of the potential wells. Indeed, a potential difference of $\Delta\text{MIP} = 1.48$ V is induced according to Eq. (4.18), if e.g. the ionic character of Cu changes from neutral to fully ionic. However, it has to be taken care that the net charge of a unit cell must be neutral. Unfortunately, the initial ionicity of the bonds within the perfect crystal is unknown.

The question is why such a distinct change in ionicity may occur. This is expected, if the composition changes and elements with different electronegativity are present and involved in the atomic bonding or if the atomic bonds are strained or compressed. A contribution of a local change in ionicity at grain boundaries to the measured potential wells is therefore possible and can not be ruled out. This issue is discussed in Sec. 4.4.1.3 with the help of electron energy-loss spectra.

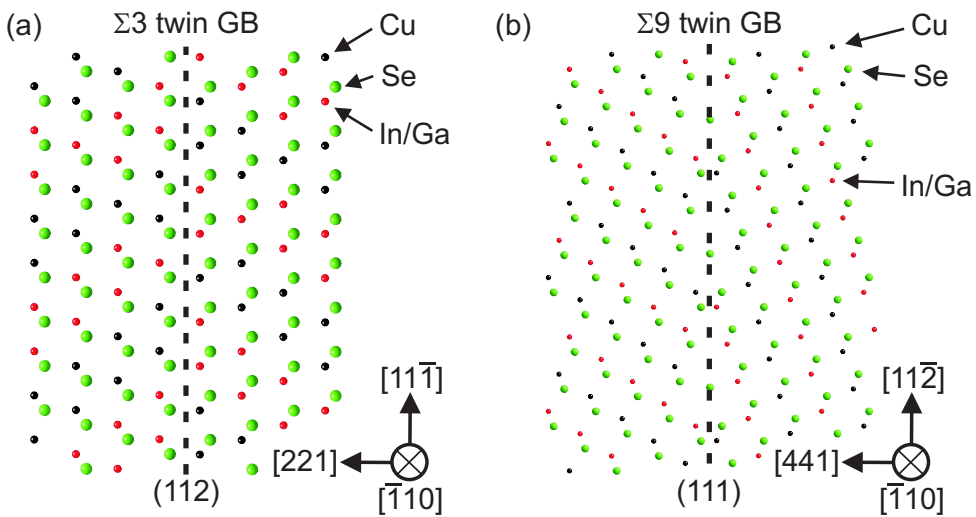


Figure 4.15: Models of the constellation of a Σ_3 (112) 180° rotational twin grain boundary (GB) (a) and a Σ_9 (111) 180° rotational twin boundary (b) in Cu(In,Ga)Se₂ based on geometrical considerations and symmetry.

4.2.4 Effect of grain boundary geometry investigated by simulations

In this section, the possible influence of the grain boundary geometry on the averaged electrostatic potential is estimated. At a grain boundary, where two grains meet, the periodicity of the lattice is disturbed. In general, there are two possible scenarios, how the crystal lattice may look like at the interface. In the first scenario, the local crystal structure at the grain boundary is described by simple geometrical considerations. The grain boundary structure is given by the contact of the surfaces of both adjacent crystal lattices, with respect to the lowest possible total energy achievable. In the second, much more complicated scenario, the lattice at and close to the interface reconstructs with respect to the composition and the bond lengths until the involved atoms occupy sites leading to the energetically most favorable configuration. This approach considers the interaction between all involved atoms self consistently. Typically, DFT calculations are employed to solve these specific problems. Unfortunately, there is no simple access to model a possible reconstruction in the case of random grain boundaries, since a defined structure is required as a starting point for the calculations.

In this section, the former consideration is treated for two special cases. Fig. 4.15 shows

models of a $\Sigma 3$ (112) 180° rotational twin boundary and a $\Sigma 9$ (111) 180° rotational twin boundary in Cu(In,Ga)Se₂ that have been discussed and investigated in the literature [84, 178]. The general assumption underlying these models is that the crystal lattices of both adjacent grains do not overlap, i.e., that there is one plane that can be considered to terminate both adjacent grain lattices. The $\Sigma 3$ grain boundary is coherent, i.e., its composition does not change across the grain boundary with respect to the nearest neighbors of the adjacent atoms. Such grain boundaries have been found by Krejci et al. [71] in epitaxially grown CuInSe₂ and are assumed to be the most frequent type of $\Sigma 3$ grain boundaries within CuInSe₂ [178, 179]. For this model, the bond lengths across the grain boundary were assumed to be equal to the corresponding bond lengths within the perfect lattice, which, however, is not necessarily the case in general.

The grains adjacent to the $\Sigma 9$ grain boundary exhibit the same orientation relationship as it is the case for the $\Sigma 9$ grain boundary in CuGaSe₂ that has been investigated earlier in this thesis (see Sec. 4.1.5). The shown configuration serves therefore as a model system, which can be employed for simulations of the averaged electrostatic potential for comparison with the experimental results. The distance between the two grains was adjusted such that the Se atoms at the grain boundary core (initially belonging to the right grain) exhibit the same bond lengths to the nearest neighboring atoms on either side. The closest distance between the cations and the Se atoms across the grain boundary was chosen to match the corresponding bond length in the perfect lattice. Note that the two lattices do not overlap and coincide only with the Se atoms at the grain boundary core. The effective result is a smaller local atom density at the grain boundary.

In order to study the averaged electrostatic potential on the basis of the geometrical consideration, three dimensional supercells of both grain boundaries were constructed.

The supercell of the $\Sigma 3$ (112) 180° rotational twin boundary comprised ~ 5500 atoms and exhibited dimensions of 7.7 nm in [221] direction, 3.9 nm in [1̄10] direction, and 3.9 nm in [11̄1] direction. The supercell of the $\Sigma 9$ (111) 180° rotational twin boundary comprised ~ 2300 atoms and exhibited dimensions of 4.5 nm in [441] direction, 2.8 nm in [1̄10] direction, and 3.7 nm in [11̄2] direction. These supercells served as input for multislice simulations [147] performed by use of JEMS [180]. The required electron scattering factors were taken from Refs. [171, 172, 181]. Note that the scattering factors of neutral atoms were applied, since the ionic scattering factors of Se²⁻ and S²⁻ are not available in the literature. However, a comparison of the estimated MIP by use of neutral scattering

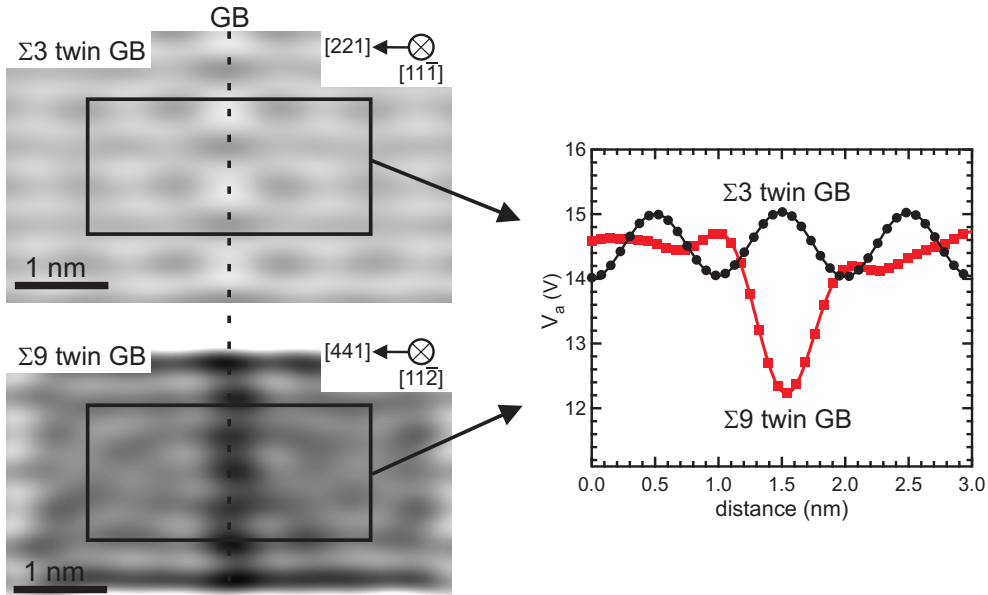


Figure 4.16: Gray-value phase images obtained by multislice simulations of supercells containing the $\Sigma 3$ and $\Sigma 9$ twin grain boundaries (GB) shown in Fig. 4.15 for CuInSe₂. The same low pass filter was applied on the simulated phase distributions as it was for the reconstruction of the measured phase images. Extracted profiles of the averaged electrostatic potential across the grain boundaries averaged over the highlighted regions of interest are shown on the right.

factors and experimental results showed satisfactory agreement (see Sec. 4.2.3), leading to the assumption that neutral scattering factors are a good approximation. The lattice constants of the unit cells were already discussed in Sec. 4.2.3. The averaged electrostatic potential was then extracted from the phase distributions of the simulated object wave functions as described in Sec. 3.2.6. Fig. 4.16 shows the calculated gray-value images of the phase distributions in the case of CuInSe₂. The same spatial frequencies that were filtered out by the low-pass filter during the reconstruction of the object wave function by use of inline electron holography (see Sec. 3.2.4), which corresponds to spatial frequencies higher than the objective aperture radius ($\sim 1.2 \text{ nm}^{-1}$), were also filtered out here, to make the calculation comparable with the experimental results. Due to the absence of any free charge carriers in the models, the absolute value of the averaged electrostatic potential corresponds to the MIP in both cases.

The profile of the averaged electrostatic potential across the $\Sigma 3$ grain boundary in Fig. 4.16 shows an oscillation. This oscillation arises from the fact that the crystal lattice is tilted in

zone axis orientation, where the atomic columns are parallel to the incident electron beam. In addition, the local thickness fluctuates slightly, owing to the fact that the top and the bottom of the model are terminated by planes that are not parallel to the lattice planes (see Fig. 4.15). In contrast, the specimen was not tilted in a zone axis configuration for the measurements, which led to an averaging of the potential from the atomic columns and the space in between. Moreover, the total specimen thickness was much larger reducing the effect of similar thickness fluctuations on the potential. The oscillations exhibit a mean value of approximately 14.5 V and continue to either side. No significant change of the oscillation is present at the grain boundary. This is a consequence of the coherence of the grain boundary, i.e., the composition averaged over the shown region of interest as well as the bond lengths do not change across the grain boundary compared with the grain interior.

Further simulations were performed on mirror symmetric $\Sigma 3$ reflectional twin boundaries, for which two anion or cation terminated (112) surfaces face each other across the grain boundary. A structural model of the latter is shown in Fig. 4.24. Similar to the $\Sigma 3$ (112) 180° rotational twin boundary investigated here, an oscillation of the averaged electrostatic potential was found due to the zone axis configuration. However, no significant change of this behavior was found at the grain boundary in either case.

In contrast, a distinct potential well with a depth of about 2.5 V and a FWHM of about 0.5 nm is present at the $\Sigma 9$ grain boundary. Its origin is the smaller local density of atoms at the grain boundary core, which is allowed by the symmetry. Deviations from a flat potential away from the grain boundaries can be explained by slight thickness variations of the supercell along the [11 $\bar{2}$] direction that was chosen for the simulation, see Fig. 4.15, and the zone axis orientation. Nevertheless, the MIP average value in the grain interior, more than 0.5 nm away from the grain boundary core, of about 14.5 V is similar to the mean value found in the case of the $\Sigma 3$ grain boundary. The values are not the exact same as estimated by use of Eq. (4.18) (15.51 V). A reason might be that the supercell dimension is not a multiple of the unit cell dimension. However, the values agree well with the measured value of (14.0 ± 1.6) V, see Sec. 4.1.1.

Fig. 4.17 shows the direct comparison of the potential profile that was measured at the $\Sigma 9$ grain boundary in CuGaSe₂ (see Fig. 4.7) and the one that was obtained from multislice simulations on the $\Sigma 9$ grain boundary model for CuGaSe₂. It can be seen that the simulated potential well is about three times deeper and exhibits about half the width of the measured

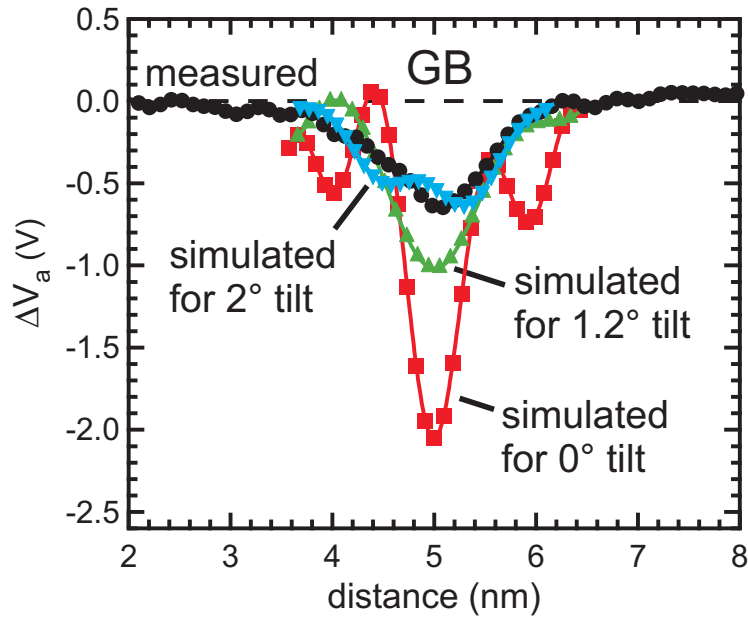


Figure 4.17: Comparison of the potential well that was measured at a $\Sigma 9$ grain boundary (GB) within CuGaSe₂ (see Sec. 4.1.5) and the potential well that was determined by multislice simulations on a supercell model of the $\Sigma 9$ grain boundary shown in Fig. 4.15(b), for which the incident electron beam was assumed to be parallel to the [11̄2] direction. The green (blue) curve shows the simulated potential profile of the $\Sigma 9$ grain boundary, if a specimen thickness of 47 nm and a tilt of $\alpha_t = 1.2^\circ$ (2°) around the [1̄10] axis is assumed.

potential well. However, a slight deviation from the perfect edge-on configuration of the $\Sigma 9$ grain boundary, with respect to the electron beam, during the measurement can have a huge impact on the width of the potential well. For a specimen thickness of about 47 nm, as it was found from the thickness measurement, a tilt of about $\alpha_t = \sin^{-1}(1 \text{ nm}/47 \text{ nm}) \approx 1.2^\circ$ around the [1̄10] axis is sufficient, to broaden the potential well to a width of about 1 nm. The simulated potential profile of the $\Sigma 9$ grain boundary for a specimen thickness of 47 nm (this corresponds to a stack of 12 supercells) and tilts of $\alpha_t = 1.2^\circ$ and $\alpha_t = 2^\circ$ around the [1̄10] axis are shown in Fig. 4.17.

The potential well which is present at the $\alpha_t = 1.2^\circ$ tilted grain boundary has about the same FWHM as the measured one, however, is about one and a half times as deep. The potential well which is present at the $\alpha_t = 2^\circ$ tilted grain boundary is a bit wider but has almost the same depth as the measured one. The grain boundary geometry in combination with a slight tilt of less than 2° from the edge-on orientation are therefore able to explain the measured potential well shape satisfactorily. In the case of the $\Sigma 9$ grain boundary, this

means that the contribution of geometry to the MIP is large enough to account solely for the potential distribution which was found experimentally.

Other symmetric constellations of the $\Sigma 9$ (111) 180° rotational twin boundary, for which the bond lengths across the grain boundary are not smaller than in the perfect crystal lattice, are not considered at this point, because the atom densities at the grain boundaries are smaller in these models, and the discrepancy between simulation and measurement is larger.

This example also shows that a slight misalignment of the grain boundary with respect to the edge-on orientation during the electron holography measurement can have a huge impact on the shape of the measured potential wells. However, the area above the potential wells seems to be almost invariant up to this misalignment. Since all measured potential wells exhibited a similar width, greater than the spatial resolution of the method, it is assumed that the depths of the measured potential wells shown in this thesis are comparable with each other.

4.2.5 Possible measurement artifacts

So far, any systematic artifacts or errors have been neglected. This issue is discussed in the following. Measurement artifacts may arise from:

- **Fringing fields:** Errors may be induced by electrostatic fields that extend from the specimen into the vacuum region on either side of the specimen and contribute to the measured phase shift in the object wave function. This issue has been discussed by Pozzi [182] and Dunin-Borkowski et al. [183]. However, both authors conclude that a contribution from such electrostatic fringing fields is small if the specimen thickness is much larger than the length scale on which a change in potential occurs. The regions of interest analyzed in the present work exhibited specimen thicknesses of at least 20 nm, and typically even close to 50 nm. This is at least an order of magnitude larger than the width of the measured potential wells. The effect of electrostatic fringing fields on the measured phase shift is thus expected to be small. Although the contribution of fringing fields to the measured phase shift was found to increase with the permittivity ϵ_r of the specimen, the effect manifests itself in an offset which is added to the phase shift, rather than a deformation of the measured potential profile [183]. Such an offset is of no importance here since only relative

phase shifts are measured across grain boundaries. If there are considerable space or excess charge layers at the grain boundaries, which are not detectable with the applied methods, their extension is much wider than the specimen thickness and the width of the potential wells. In the 1–2 nm wide region, where a change in potential is found, this would rather lead to an offset to the averaged electrostatic potential than a deformation of the shape of the potential distribution.

- **Dead layers:** Another possible error might be introduced by dead layers with thickness d_0 on top of either side of the specimen. These are layers which are significantly distorted owing to the specimen preparation and which may therefore not contribute to the potential $V_{\text{cr}}(\vec{r})$ caused by any free charge carrier redistribution. This, as a result, reduces the effective thickness of the specimen in which charge redistribution may occur to $d_{\text{eff}}(\vec{r}) = d(\vec{r}) - 2d_0(\vec{r})$. As a consequence, the phase shift in the object wave function is not given by

$$\varphi(\vec{r}) = \sigma(U)(\text{MIP}(\vec{r})d(\vec{r}) + \Delta V_{\text{cr}}(\vec{r})d(\vec{r})) \quad (4.20)$$

anymore (see Eq. (3.22) and Eq. (3.4)), but by [184]

$$\varphi(\vec{r}) = \sigma(U)(\text{MIP}(\vec{r})d(\vec{r}) + \Delta V_{\text{cr}}(\vec{r})(d(\vec{r}) - 2d_0(\vec{r}))). \quad (4.21)$$

If a change in $\Delta V_{\text{cr}}(\vec{r})$ contributes to a phase shift, the measured phase shift $\varphi(\vec{r})$ should decrease with decreasing total specimen thickness since the contribution of $\Delta V_{\text{cr}}(\vec{r})$ becomes less significant. This means that if a change in $\Delta V_{\text{cr}}(\vec{r})$ gives a major contribution to the potential wells measured at grain boundaries in Cu(In,Ga)(Se,S)₂, the contribution to $\Delta V_a(\vec{r})$ should decrease with decreasing specimen thickness, and with it the potential well depths. Such an effect was not found in this work. A substantial contribution of dead layers is therefore assumed to be negligible.

- **Dipole layers:** The presence of a dipole layer on both surfaces of the TEM lamella is also possible. However, a dipole layer with the same dipole moment everywhere on both surfaces, also at the grain boundary, affects the averaged electrostatic potential only insofar as that a constant value, i.e., the average of both resulting dipole potentials along the z axis, is added to the averaged electrostatic potential. This again

is irrelevant for the changes in the averaged electrostatic potential presented here, however, may affect its absolute value significantly. Nevertheless, a locally changing surface dipole moment may deteriorate the measurements.

- **Surface grooves:** The Ar-ion polishing process during the specimen preparation may lead to a preferential etching at grain boundaries, giving rise to surface grooves where grain boundaries meet the TEM lamella surface (see Fig. 4.18(a)). Since such surface grooves reduce the specimen thickness, measurements—assuming a constant specimen thickness—would yield a smaller averaged electrostatic potential at the grain boundaries than actually present. Assuming a 50 nm thick TEM lamella of CuInSe₂, with a MIP of about 14.0 V, $s_{sg} = 3.5$ nm deep surface grooves on either side of the TEM lamella would appear in the measurement as a local reduction of the averaged electrostatic potential. This corresponds to a local reduction of the specimen thickness by 14 %. The reduction in the potential can be estimated by $MIP(1 - (d - 2s_{sg})/d) = 2$ V. Such surface grooves, 3.5 nm deep and 1.5 nm wide, could therefore explain the dimensions of the measured potential wells at grain boundaries. This situation is illustrated in Fig. 4.18(b). However, the proportions of these surface grooves seem unrealistic, especially with respect to the incident angle of the Ar-ion beam of less than 9 °.

It was mentioned earlier that no significant features within the acquired d/λ_{mfp} maps could be correlated with grain boundaries. Since the inelastic mean free paths—for the applied collection angle—of pure Cu (133 nm), In (116 nm), Ga (131 nm), or Se (128 nm) specimens differ at most by 7.2 % from the inelastic mean free path of CuInSe₂ (125 nm), a thickness reduction of 14 % caused by surface grooves would conflict with the smooth d/λ_{mfp} behavior, even if significant changes in the local composition were considered. A possible reduction in the local atom density, as discussed in Sec. 4.2.4, would result in a higher λ_{mfp} , and would even require a higher local specimen thickness d at grain boundaries to explain the smooth behavior of d/λ_{mfp} .

In addition, if surface grooves are present at all investigated grain boundaries, their depths and widths should be similar in average, independent of the total specimen thickness. Their contribution to the potential wells would therefore decrease with increasing specimen thickness. However, no correlation between the specimen thick-

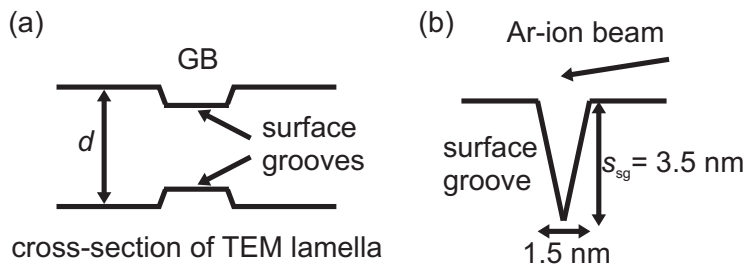


Figure 4.18: Schematic of a TEM lamella cross section with surface grooves on either side (a), and the dimensions of surface grooves that may cause potential wells similar to the measured ones (b).

ness and the potential-well depth was found. Surface grooves are therefore assumed to contribute to the measured potential wells only to a minor extent. However, an investigation of the topography of the TEM specimens at grain boundaries by use of scanning tunneling microscopy (STM) or atomic force microscopy (AFM) may shed light on that issue.

Due to the random orientation of grain boundaries and the small grain sizes, it was not possible to perform tilt series, with tilt axis along a vector contained in the grain boundary with constant z value. With such a tilt series, it is possible to determine the specimen thickness at the grain boundary [185].

4.3 Comparison with studies on grain boundaries in other materials

Potential profiles across grain boundaries or interfaces in other materials have been studied in the past in a similar way like in the present work by use of Fresnel contrast analysis as well as by inline and off-axis electron holography. In Fresnel contrast analysis, intensity profiles of images within a through focal series across interfaces are extracted and compared with simulations in order to determine local changes in the averaged electrostatic potential [133]. The unambiguous interpretation of the potential profiles was not possible in most cases. A summary of the previous studies is given in the following.

Kara et al. [132] employed Fresnel contrast analysis to investigate grain boundaries in mullite ($3\text{Al}_2\text{O}_3 \cdot 2\text{SiO}_2$). They found averaged electrostatic potential wells being present at

two different types of grain boundaries. One grain boundary exhibited a glassy film between the two adjacent grains in contrast to the other that exhibited a crystalline grain boundary. They attributed a local change in composition, which they found by use of STEM-EDX, to be responsible for the 5 V deep potential well at the grain boundary exhibiting the glassy film. They were not able to detect local changes in composition at the crystalline grain boundary. Excluding a local change in the ionicity and a local strain at the grain boundary by use of rough estimations, they concluded that a bound charge density at the grain boundary and a corresponding layer of free charge carriers must be responsible for the potential well depth of about 1.5 V they measured.

Ravikumar et al. [186–189] studied pristine bicrystals and polycrystalline SrTiO₃, i.e., without extrinsic doping, and grain boundaries in Mn doped polycrystalline SrTiO₃ by use of off-axis electron holography. The grain boundaries in the undoped material exhibited smaller phase shifts than the grain boundaries in the Mn doped material. Therefore, they assumed that a reduced MIP causes the potential wells at grain boundaries in undoped SrTiO₃, whereas an additional negative bound charge at the grain boundary and corresponding positive excess charge layers on either side, are responsible for the deeper potential wells in Mn doped SrTiO₃.

In contrast, Mao et al. [190] concluded that space charge or excess charge layers conterminous to charged 24° [001] tilt grain boundaries in undoped and Nb doped SrTiO₃ can not be the main contribution to the potential wells (0.3 – 1.6 V deep and 1 – 2 nm wide) they detected by use of Fresnel contrast analysis. However, combining the Fresnel contrast analysis with high resolution TEM, EELS, and STEM-EDX they were not able to identify the origin of the potential wells unambiguously.

Similar measurements were performed by Koch [185]. He compared averaged electrostatic potential profiles across a $\Sigma 13$ grain boundary in a nominally undoped SrTiO₃ bicrystal, determined by use of the same inline electron holography method as applied in this thesis, with impedance spectroscopy data. While the averaged electrostatic potential profiles show a potential well, with a depth of about –680 mV and a FWHM of about 2 nm width, being present at the grain boundary, the impedance spectroscopy results indicate the presence of a potential barrier at the grain boundary with a barrier height of about 500 mV and a FWHM of more than 100 nm. This finding suggests that two length scales must be considered. One on which possible space or excess charge layers determine the potential (100 nm) and one on which the local crystal configuration at the grain boundary determines

the potential (~ 1 nm). Interestingly, the gray-value images of the averaged electrostatic potential determined by use of inline electron holography showed patches of increased potential (about 150 mV higher compared with the potential more than 20 nm away from the grain boundary) close to the grain boundary and parallel to its core. This finding is consistent with a much wider potential barrier, considering the lower limit of spatial frequencies that can be imaged with this method (which corresponds to a distance of l_{eff} of a few tens of nm). This indicates the capability of this technique to image such wide potential barriers. Such an increased potential close to the grain boundaries could not be found at grain boundaries in Cu(In,Ga)Se₂ and CuInS₂.

One common feature of the described investigations and the results presented in this thesis is the lowering of the electrostatic potential, which has been found to be present at all grain boundaries. This raises the question whether this lowering is a generic feature of grain boundaries. A smaller atom density due to the lattice distortion or due to the grain boundary geometry (see Sec. 4.2.4), for example, may at least in part account for the potential wells.

4.4 Correlation between the potential wells and a local change in composition

The evaluation in the previous section showed that a very probable explanation for the existence of the measured potential wells is a local change in composition at the grain boundaries. This issue is further examined in the following with the help of the Cu series, for which the local composition at grain boundaries was measured. The spatial extent of the observed averaged electrostatic potential wells suggests that a possible local change in composition may occur in a region closer than ~ 1 nm from the grain boundary cores. A sufficient spatial resolution of the measurement technique is therefore required. This section presents results from the local changes in composition which have been measured by use of STEM-EELS and atom probe tomography to correlate them with the potential wells.

4.4.1 Experimental results

The EELS results which are presented in the following were measured on TEM specimens that were prepared by the H-bar and the FIB method (see Sec. 3.2.8) only. With both methods, it was possible to avoid problems in the acquisition and in the evaluation of EEL spectra due to a contamination of the specimen surface by C from the epoxy glue. The EELS measurements were performed by Dr. Bernhard Schaffer, SuperSTEM, STFC Daresbury Laboratories, Warrington, United Kingdom.

4.4.1.1 Averaged electrostatic potential and EELS profiles from the identical grain boundary within Cu(In,Ga)Se₂

Fig. 4.19 shows elemental profiles of the elements Cu (Cu-L_{2,3} edge), Se (Se-L_{2,3} edge), In (In-M_{4,5} edge), and O (O-K edge) which were extracted from an EEL spectrum image acquired across a grain boundary within a Cu(In,Ga)Se₂ absorber exhibiting the ratios [Cu]/([In] + [Ga]) = 0.83 and [Ga]/([In] + [Ga]) = 0.28. The averaged electrostatic potential profile extracted across the same grain boundary is shown below. The potential well depth at this specific grain boundary was found as -1.9 V. Signals from the elements Ga, and Na could not be evaluated due to their unfavorable position in the EEL spectrum (see Sec. 3.2.7). The Na-K edge and the Ga-L_{2,3} edge are very close to the onset of the Cu-L_{2,3}. The EELS signals indicate the presence of a local change in composition at the grain boundary with a spatial extent similar to that of the potential wells. A clear signal decrease at the grain boundary is found in case of Se. In contrast, the In and O signals show a distinct increase at the grain boundary. The Cu signal is ambiguous. While the lowest signal is located at the grain boundary core, the highest signal is found at a distance of about 1 nm on either side of the grain boundary. The high mobility of Cu in Cu(In,Ga)Se₂ [191] may account for this observation. A thermal activation of Cu diffusion by electron-beam irradiation is possible, and could lead to a distortion of the signal. It should also be noted that damage of the specimen due to electron beam irradiation was visible in the STEM-HAADF image after the acquisition of the spectrum image. However, this result was confirmed by elemental profiles that were determined from EEL spectrum images acquired at slightly different positions at the same grain boundary.

It was further found that a significant amount of C is present within the specimen, however, confined to local patches. Electron beam irradiation induced contamination of the specimen

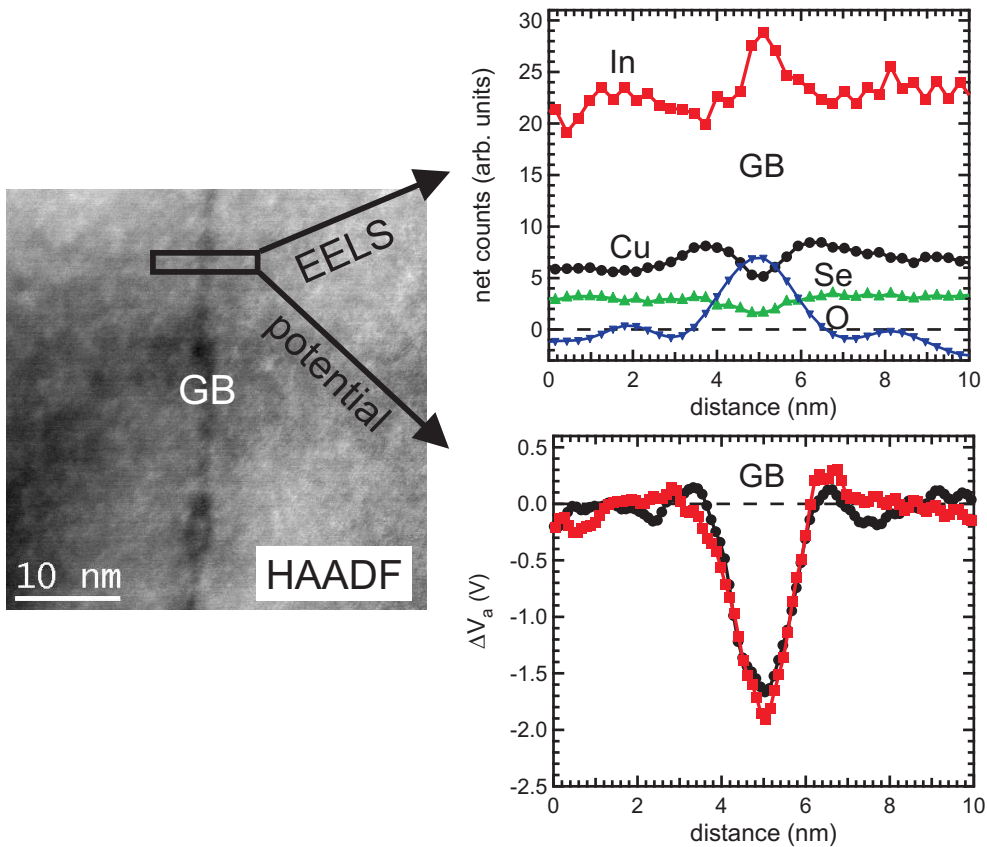


Figure 4.19: Elemental distribution profiles of the elements Cu (Cu-L_{2,3} edge), Se (Se-L_{2,3} edge), In (In-M_{4,5} edge), and O (O-K edge) extracted from an EEL spectrum image acquired across a grain boundary (GB) within a Cu(In,Ga)Se₂ absorber exhibiting $[Cu]/([In] + [Ga]) = 0.83$ and $[Ga]/([In] + [Ga]) = 0.28$. The profile was extracted from the highlighted region in the STEM high angle annular dark field (HAADF) image on the left side. The averaged electrostatic potential profile determined at the same grain boundary is shown below. The investigated specimen was prepared by use of the H-bar method, see Sec. 3.2.8.

surface with C, a 2 min plasma-cleaning procedure before the EELS measurements or the H-bar preparation method of the specimen may account for this. The EELS signal profiles shown in Fig. 4.19 were extracted across a region where the carbon signal was smallest. It should be mentioned that the In and the Cu signal showed an anticorrelated behavior in all extracted profiles.

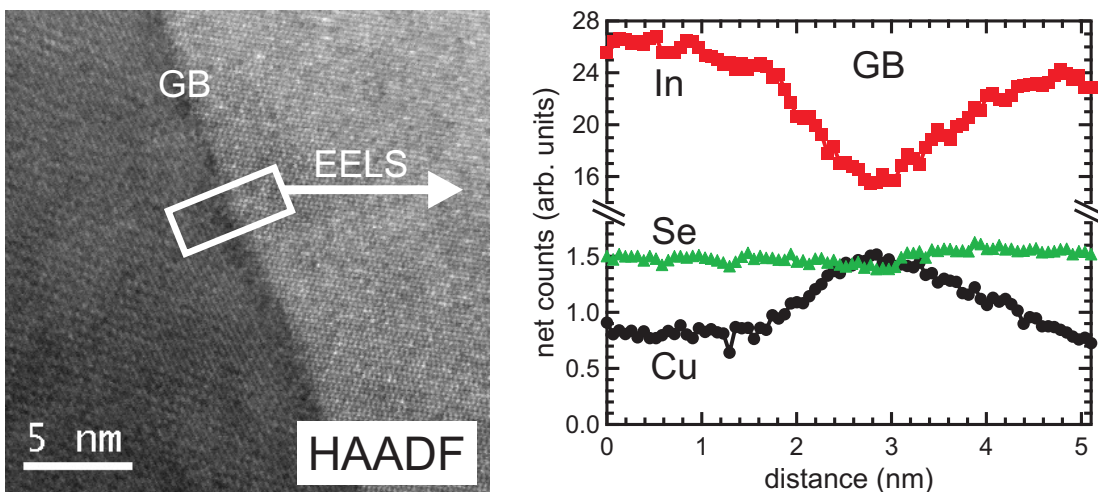


Figure 4.20: Elemental distribution profiles of Cu (Cu-L_{2,3} edge), Se (Se-L_{2,3} edge), and In (In-M_{4,5} edge) extracted from an EEL spectrum image acquired across a grain boundary (GB) within a Cu(In,Ga)Se₂ absorber exhibiting [Cu]/([In] + [Ga]) = 0.43 and [Ga]/([In] + [Ga]) = 0.32, which is shown in the STEM-HAADF image on the left. No traces of O or C were found. The specimen was prepared by use of the pure FIB method.

4.4.1.2 Dependence of local changes in composition on the integral Cu concentration of the absorber

Elemental distribution profiles of the elements Cu (Cu-L_{2,3} edge), Se (Se-L_{2,3} edge), and In (In-M_{4,5} edge), which were extracted from an EEL spectrum image acquired across a grain boundary within a Cu(In,Ga)Se₂ absorber exhibiting [Cu]/([In] + [Ga]) = 0.43 and [Ga]/([In] + [Ga]) = 0.32 are shown in Fig. 4.20. In contrast to the results on grain boundaries within the absorber exhibiting [Cu]/([In] + [Ga]) = 0.83, the Cu signal increases towards the grain boundary, while the In signal decreases. However, the spatial extension of the change in composition is similarly 1 – 2 nm. The Cu and In signals are likewise anticorrelated, which was confirmed by further EELS measurements (not shown here). The Se signal indicated no significant change in the Se composition at grain boundaries. It was not possible yet to measure the averaged electrostatic potential profile across this specific grain boundary. However, averaged electrostatic potential profiles across other grain boundaries within the same sample are available (see Fig. 4.1). It should be pointed out that no traces of O or C were found in this specimen.

Unfortunately, EELS measurements across grain boundaries within absorbers exhibiting [Cu]/([In] + [Ga]) = 0.67 are not yet available. However, compositional measurements

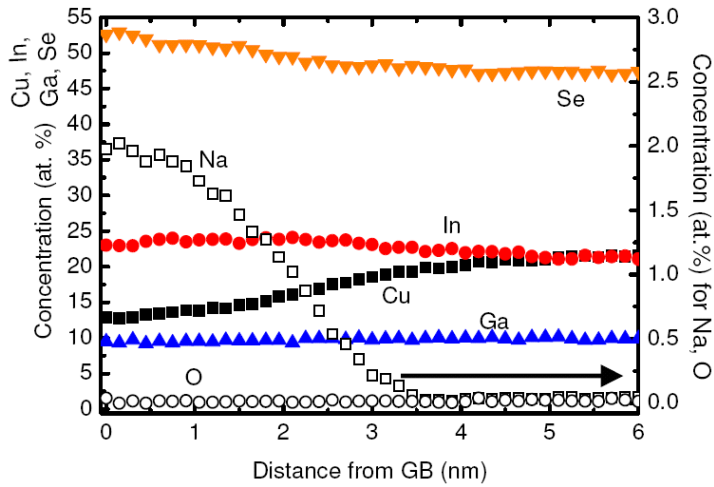


Figure 4.21: Elemental distribution profiles in the vicinity of a grain boundary within a Cu(In,Ga)Se₂ absorber exhibiting $[Cu]/([In] + [Ga]) = 0.43$, which were determined by means of atom probe tomography. The profiles are illustrated as proximity histogram [192], where the grain boundary core is located at distance = 0. By courtesy of O. Cojocaru-Mirédin and P.-P. Choi, Max Planck Institute for Iron Research, Düsseldorf, Germany.

were performed by means of atom probe tomography (see Sec. 3.3). Fig. 4.21 shows profiles extracted from a proximity histogram [192] of a grain boundary within the very same absorber material. It should be mentioned that the grain boundary was not identified by an analysis of the lattice orientation on either side but by the assumption that a local change in composition may only occur at grain boundaries. The Na concentration increases significantly towards the grain boundary core. A smaller relative increase in concentration is found for In and Se. As measured at a grain boundary in the absorber exhibiting $[Cu]/([In] + [Ga]) = 0.83$, the Cu signal is reduced at the grain boundary core. However, no maximum of the Cu signal was found about a nm away from the core as it was found for the grain boundary within the Cu(In,Ga)Se₂ absorber exhibiting $[Cu]/([In] + [Ga]) = 0.83$. No trace of O was detected at this grain boundary.

Fig. 4.22 gives an overview of the averaged electrostatic potential profiles that were measured at grain boundaries within Cu(In,Ga)Se₂ absorbers exhibiting compositions with different $[Cu]/([In] + [Ga])$ ratios and the corresponding profiles of the local composition. A major difference between the different compositional profiles is the O increase at the grain boundary in the standard absorber ($[Cu]/([In] + [Ga]) = 0.83$). However, it is likely that the local O increase at this grain boundary was introduced by the plasma-cleaning

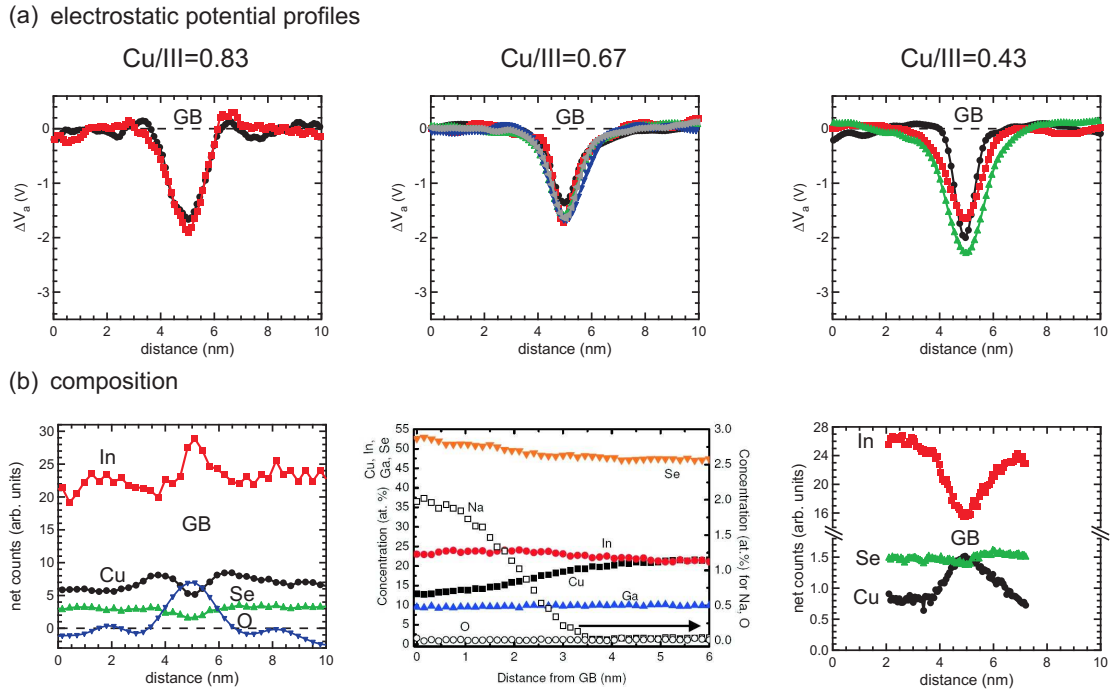


Figure 4.22: Correlation of the measured averaged electrostatic potential profiles across grain boundaries (GB) within absorber exhibiting different $[\text{Cu}]/([\text{In}] + [\text{Ga}])$ ratios (a) and the corresponding profiles of the local composition measured by use of EELS or APT (b). Please note that the results belong to the very same grain boundary only in the case of $[\text{Cu}]/([\text{In}] + [\text{Ga}]) = 0.83$.

treatment of the TEM specimen prior to the EELS measurements, since no traces of O were found in the other two samples ($[\text{Cu}]/([\text{In}] + [\text{Ga}]) = 0.43$ and 0.67) that were not plasma-cleaned. The plasma-cleaning procedure should therefore be avoided in future investigations.

No change in the local composition at grain boundaries was detected in an analogous investigation of the local composition by means of STEM-EDX performed at a Zeiss LIBRA 200FE. The main reason might be the low count rate of X-ray photons, even for the highest beam intensities, for which the spatial resolution was smaller than 2 nm. In addition, strong electron beam induced contamination of the TEM surface was observed which can lead to a significant deterioration of the measurements.

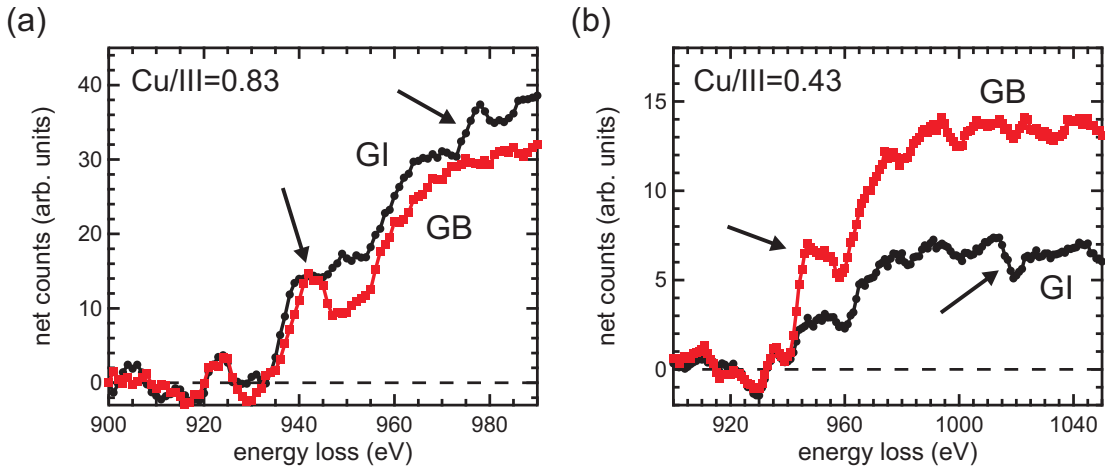


Figure 4.23: Comparison of the Cu-L_{2,3} core-loss edge fine structure in electron energy-loss spectra acquired at the grain boundary (GB) and at the grain interior (GI), in the case of the absorber with a composition of $[\text{Cu}] / ([\text{In}] + [\text{Ga}]) = 0.83$ (a) and the absorber with a composition exhibiting $[\text{Cu}] / ([\text{In}] + [\text{Ga}]) = 0.43$ (b). The energy-loss background has been subtracted as described in Sec. 3.2.7. The black arrows highlight pronounced differences in the spectra.

4.4.1.3 Fine structure of core loss edges in the electron energy-loss spectra

The fine structure and the extended fine structure of core-loss edges in electron energy-loss spectra reflect the influence of the surrounding atoms on the electronic states of the atom under investigation [142]. If the electronic states of an atom are affected by a change in the atomic environment, e.g. at a grain boundary, the fine structure is likely to change. Such a change in the electronic states may also influence the ionicity, i.e., the ionic character of atomic bonds. This is briefly studied in the following.

Fig. 4.23 shows the Cu-L_{2,3} core-loss edge fine structure in electron energy-loss spectra acquired at the grain boundary and in the grain interior in the case of the two investigated absorbers with compositions of $[\text{Cu}] / ([\text{In}] + [\text{Ga}]) = 0.83$ and $[\text{Cu}] / ([\text{In}] + [\text{Ga}]) = 0.43$. Although the spectra exhibit different intensities, representing the elemental concentrations, pronounced differences, highlighted by arrows, are noticeable. These differences indicate local changes in the atomic environment of Cu atoms at grain boundaries, which might be correlated with a local change in ionicity or in the bond lengths, as discussed in Sec. 4.2.3. Such a change in ionicity may as well contribute to the lowering of the averaged electrostatic potential at grain boundaries. A detailed evaluation of this fine structure was

not possible within the scope of this work.

4.4.2 Discussion on local compositional changes, their origins and impacts

In the following, the finding of potential wells at grain boundaries and correlated changes in composition in absorbers of the Cu series are combined. Potential well depths are estimated by use of Eq. (4.18) with respect to the local changes in composition that were measured by use of EELS. Three possible causes for the presence of compositional changes at grain boundaries are proposed and discussed. The transfer to the Ga series and CuInS₂ absorbers is addressed. Finally, the impact on the electrical properties of grain boundaries is briefly discussed.

4.4.2.1 Estimation of potential well depths with respect to the local composition

From the EELS and APT results on the Cu series in Figs. 4.19, 4.20, and 4.21, one can estimate the local change in composition at grain boundaries for the elements Cu, Se, and In. The average level of the EELS signal in the grain interior more than 2 nm away from the grain boundary core is assumed to correspond to the atomic concentrations according to the total integral composition shown in Tab. 3.1. It is assumed in the following that the EELS signal of one element is linearly dependent on its atomic concentration. Generally, this linear relation only holds for very thin specimens, with thicknesses below $0.3\lambda_{\text{mfp}}$, for which multiple scattering can be neglected [144]. This is about the order of the thicknesses of the regions of interest from which the results were obtained. It is therefore presumed that the linear relation is a good approximation. Therefore, the ratio between the net counts at the grain boundary and the net counts in the grain interior corresponds to the ratio between the concentration c_{gb} of the respective element (in at.%) at the grain boundary and the concentration c_{gi} in the grain interior.

Tab. 4.7 shows the ratio $c_{\text{gb}}/c_{\text{gi}}$ for each measured element and corresponding changes in the ΔMIP according to Eq. (4.18) for a constant unit cell volume, and by use of the neutral electron scattering factors (see Tab. 4.5). The numbers in brackets are the corresponding values if the scattering factors of the respective ions are applied. The last two rows show the total estimated change $\Delta\text{MIP}^{\text{tot}}$ and the corresponding measured potential well depths.

Table 4.7: Ratios $c_{\text{gb}}/c_{\text{gi}}$ of the atomic concentrations c_{gi} in the grain interior and the atomic concentrations c_{gb} at the grain boundary of the elements Cu, In, and Se from Figs. 4.19, 4.20, 4.21. Corresponding changes in the MIP are denoted by ΔMIP . For this estimation, the unit cell volume of CuInSe₂ was applied, and it was assumed that every lattice site is occupied in the unit cell according to the integral composition in Tab. 3.1. The last two rows show the total change in the MIP for which the changes caused by the individual elements were summed up and the corresponding measured potential well depths. In the case of $[\text{Cu}]/([\text{In}] + [\text{Ga}]) = 0.83$, the latter was obtained at the grain boundary at which electron holography and EELS were performed (see Tab. 4.19). In the other two cases $[\text{Cu}]/([\text{In}] + [\text{Ga}]) = 0.67$ and $[\text{Cu}]/([\text{In}] + [\text{Ga}]) = 0.43$, the values were taken from Tab. 4.1.

	$\frac{[\text{Cu}]}{[\text{In}]+[\text{Ga}]} = 0.83$		$\frac{[\text{Cu}]}{[\text{In}]+[\text{Ga}]} = 0.67$		$\frac{[\text{Cu}]}{[\text{In}]+[\text{Ga}]} = 0.43$	
	$c_{\text{gb}}/c_{\text{gi}}$	ΔMIP (V)	$c_{\text{gb}}/c_{\text{gi}}$	ΔMIP (V)	$c_{\text{gb}}/c_{\text{gi}}$	ΔMIP (V)
Cu	0.85	-0.42 (-0.22)	0.59	-0.98 (-0.51)	1.88	1.51 (0.78)
In	1.20	0.80 (0.33)	0	0	0.59	-1.87 (-0.76)
Se	0.5	-3.69	1.05	0.38	0.93	-0.54
all elements		-3.31		-0.6		-0.90
experiment		-1.9 ± 0.1		-1.60 ± 0.14		-1.98 ± 0.32

A change in the Ga concentration is not considered since the corresponding signal could not be evaluated by use of EELS and the APT measurement showed no change of the Ga concentration at the grain boundary core. The unit cell volume of CuInSe₂ was applied for the estimations given in Tab. 4.7. This leads to an underestimation of the changes in the averaged electrostatic potentials by about 4 %, since a substitution of $\sim 30\%$ In atoms for Ga atoms leads to a $\sim 4\%$ smaller unit cell volume. The different Cu concentrations of the three different absorber layers are assumed to have a negligible effect on the unit cell volume since the lattice constants of CuInSe₂ and CuIn₃Se₅ are similar [17, 177].

It can be seen that the estimated change in the averaged electrostatic potential due to a change in the local composition, which was determined by use of EELS and APT measurements, is in the same order of magnitude as the experimentally determined potential well depths in Tab. 4.1. Even the trend that the mean potential well depths of grain boundaries within absorbers exhibiting $[\text{Cu}]/([\text{In}] + [\text{Ga}]) = 0.67$ are smaller than the ones in the other absorbers is qualitatively reproduced.

Deviations may occur due to the presence of Ga, Na, and O, which were not considered

here. However, due to their relatively small integral concentration, and their small electron scattering factors, their effect is expected to be smaller compared with compositional changes of Cu, In, and Se. A strong dependency on the exact measurement position as well as on the grain-boundary type may also explain the deviations. A slight misalignment of the grain boundaries with respect to the edge-on configuration in the EELS measurement would modify the profiles of the local composition in a similar manner as the potential wells, see Fig. 4.17. In this case, the detected changes in composition at the grain boundary would be smaller than it is actual the case but occur in a wider region. This would yield an underestimation of the potential well depths. However, this can not explain the finding that the estimated potential well depth in the case of the standard absorber ($[Cu]/([In] + [Ga]) = 0.83$) is deeper than the measured one at the same grain boundary. A preferential damage of the grain boundaries (surface grooves) caused by the plasma-cleaning treatment before the EELS measurements and after the inline electron holography measurements or a substitution of Se for O may account for this. In the measurement, surface grooves would appear as a reduced concentration of all elements, also in the case of Se, which is the main contribution to the estimated potential well depth of -3.31 V in Tab. 4.7.

However, one may speculate that a local change in composition is not the only cause for the measured potential wells. Local lattice distortions resulting in different atomic densities at grain boundaries compared with the perfect crystal lattice and different ionicities of the atomic bonds may be present at grain boundaries and contribute as well to the potential wells.

4.4.2.2 Estimation of potential well depths with respect to defect complexes and phase changes

Previous studies on grain boundaries suggest that only a small downward bending of the electronic bands, below 350 meV , is present at grain boundaries [26, 107–110]. At or close to equilibrium, the bound excess charge density at grain boundaries is therefore expected to be well below⁵ $1 \times 10^{12}\text{ cm}^{-2}$. Hence, less than one net charge carrier is located at every $1/1000$ atom at the interface. Therefore, significant excess of few at.% of a negatively charged defect, e.g. a Cu vacancy V_{Cu}^- , at a grain boundary requires a balancing positively

⁵A downward bending of the bands in equilibrium of 830 meV corresponds to a bound excess charge density at the grain boundary of about $6.5 \times 10^{11}\text{ cm}^{-2}$, see Tab. 4.4.

Table 4.8: The atomic concentrations in the grain interior and at the grain boundary estimated from the ratios $c_{\text{gb}}/c_{\text{gi}}$ given in Tab. 4.7 and the integral composition of the Cu(In,Ga)Se₂ absorbers of the Cu series given in Tab. 3.1.

	$\frac{[\text{Cu}]}{[\text{In}]+[\text{Ga}]} = 0.83$		$\frac{[\text{Cu}]}{[\text{In}]+[\text{Ga}]} = 0.67$		$\frac{[\text{Cu}]}{[\text{In}]+[\text{Ga}]} = 0.43$	
	c_{gi} (at.%)	c_{gb} (at.%)	c_{gi} (at.%)	c_{gb} (at.%)	c_{gi} (at.%)	c_{gb} (at.%)
Cu	22	19	19	11	14	26
In	19	23	20	20	22	13
Ga	8	—	9	9	10	—
Se	51	26	52	55	54	50

charged defect. Note that V_{Cu}^- , V_{In}^{3-} and V_{Se}^{2+} denote vacancy defects of the respective element, as defined in Sec. 2.2.3, whereas the notation $\text{III}_{\text{Cu}}^{2+}$ denotes an antisite defect. Since the simple model of ionic bonds is only an approximation, the actual ionic character of the atomic bonds restricts the possible compositional changes. Note that the ionic character of the atomic bonds may also change at grain boundaries due to the distortion of the bond lengths.

It is assumed that the defect complexes $(2V_{\text{Cu}}^- + \text{III}_{\text{Cu}}^{2+})$ and $(2V_{\text{Cu}}^- + V_{\text{Se}}^{2+})$, from which at least the former complex is believed to have a very small enthalpy of formation in Cu(In,Ga)Se₂ [29], only exhibit a small net charge, much smaller than $\pm e$. Both defect complexes are therefore promising candidates for basic units to induce a change in composition but, at the same time, cause only a minor amount of net charge at grain boundaries. It is now estimated whether the changes in composition can be described by adding or removing units of the described defect complexes to or from the grain boundaries. In this context, the presence of the Cu(In,Ga)₃Se₅ phase at grain boundaries within the absorber with an integral composition close to the Cu(In,Ga)Se₂ phase and vice versa is discussed. Tab. 4.8 shows c_{gi} and c_{gb} estimated from the ratios $c_{\text{gb}}/c_{\text{gi}}$ given in Tab. 4.7 and the integral compositions of the Cu(In,Ga)Se₂ absorbers of the Cu series given in Tab. 3.1. In the case of the absorber with a composition of $[\text{Cu}] / ([\text{In}] + [\text{Ga}]) = 0.83$, the Cu and In concentrations both change to about the same extent but are anticorrelated. The change in the Se concentration is about eight times higher. This change in composition can therefore not be explained by an addition or removal of units of both defect complexes, even if the Ga concentration changes significantly at the grain boundary. However, the sum of the

Cu, In, and Se concentrations is way below 100 at.%. The plasma cleaning procedure prior to this measurement may have led to a deterioration of the results. The presence of phases other than Cu(In,Ga)Se₂ and Cu(In,Ga)₃Se₅ at the grain boundary can not be excluded. The change in composition at grain boundaries within the absorber layer exhibiting a ratio [Cu]/([In] + [Ga]) = 0.67, can similarly not be explained satisfactorily by an addition or removal of both defect complexes since only the Cu concentration changes significantly at the grain boundary.

In the case of the absorber layer with [Cu]/([In] + [Ga]) = 0.43, it is also hard to explain the changes in composition based on the presence or absence of the defect complexes at first sight. However, if a slightly reduced specimen thickness at the grain boundary is assumed, i.e., surface grooves, this may account for the 4 at.% reduced Se concentration and would also lead to an underestimation of the Cu and In concentration by about 2 at.% each. The corresponding grain boundary composition would be $c_{gb}^{Cu} \approx 28$ at.%, $c_{gb}^{In} \approx 15$ at.%, $c_{gb}^{Se} \approx 54$ at.%, and consequently $c_{gb}^{Ga} \approx 7$ at.%, if other elements are not considered. The change in composition with respect to the corresponding c_{gi} can then be explained by an addition or removal of the defect complex ($2V_{Cu}^- + III_{Cu}^{2+}$). The composition is furthermore close to the composition of the Cu(In,Ga)Se₂ phase. In Tab. 4.6, however, it was estimated that the MIP of the Cu(In,Ga)Se₂ phase is higher than the one of the Cu(In,Ga)₃Se₅ phase, which is in conflict with the measured of averaged electrostatic potential wells.

4.4.2.3 Estimation of potential well depths with respect to impurity atoms

Now, the effect of impurities on the measured potential wells is estimated by use of Eq. (4.18) and the scattering factors given in Tab. 4.5. The most prominent impurities which are discussed in the context of segregation at grain boundaries are oxygen (O), and sodium (Na) (see Sec. 2.3). Traces of both elements were found in the presented results. Supposing that Na preferably occupies the Cu lattice sites and O the Se lattice site due to their isovalent character, a substitution of Cu for Na or a substitution of Se for O would lead to a reduction of the MIP (see Tab. 4.5). However, if the lattice constants do not change significantly, a total substitution of neutral Cu for neutral Na reduces the MIP by only 0.76 V in the case of CuInSe₂, and even less in the case of CuIn₃Se₅. If both elements are fully ionized, the MIP decrease is 1.07 V and still smaller than the depth of the measured potential wells. A change in the Na concentration by 2 at.%, as found in Fig. 4.21,

thus results in a negligible change in the MIP. In contrast, a substitution of 30 % Se for O already yields a MIP reduction of 2 V in the case of neutral atoms. It is worth noting that the atoms of the isovalent pairs O and Se, as well as Na and Cu have different electronegativities. Hence, a substitution may result in the formation of a significant bound charge density.

In summary, it is not very likely that the potential wells are caused by Na occupying Cu sites at the grain boundary. A more likely explanation for the potential wells would be a local substitution of Se by O. However, O was only found at one grain boundary and may not in general account for a reduction of the MIP by a substitution of Se. In addition, Na (Na^+) and O (O^{2-}) exhibit different electronegativities than Cu, In, Ga, and Se. These impurities may therefore be involved in balancing the charge at grain boundaries, which is caused by lattice distortions as well as by local changes in composition (see Sec. 4.4.2.2).

4.4.2.4 Possible origins of the measured change in composition

A local change in composition of the elements Cu, In, and Se in accordance with the EELS and APT results is able to explain the FWHMs of the measured potential wells and the order of magnitude of their depths, whereas the contribution of Na and O impurities is expected to be less significant. However, the impurities may be involved in compensating bound grain boundary charges. This issue is discussed in Sec. 4.4.2.3. Together with the evaluation in Sec. 4.2 this suggests that a change in composition makes a dominant contribution to the measured potential wells. This leaves the question why such a local change in composition is present at grain boundaries. Three possibilities are discussed below.

Grain boundary geometry as origin of the measured change in composition

One possible explanation for the detected local changes in composition by means of STEM-EELS is based on geometrical considerations. For the following gedankenexperiment, suppose that the grain boundary is formed by the contact of the surfaces of two adjacent crystal lattices, as discussed in Sec. 4.2.4. Fig. 4.24 shows two schematics of a mirror symmetric $\Sigma 3$ (112) reflectional twin boundary in CuInSe₂ for two different orientations as an example. A cylinder with radius r is assumed to represent the volume from which the STEM-EELS signal is obtained. Depending on the probe size diameter $2r$ of the electron

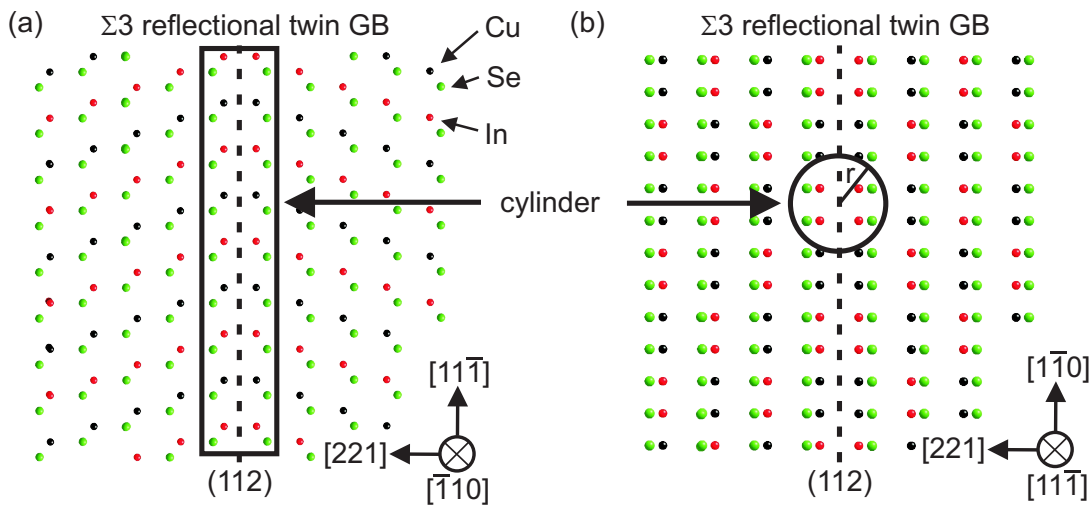


Figure 4.24: Schematic of a $\Sigma 3$ (112) reflectional twin boundary exhibiting mirror symmetry. The projection of the lattice is shown in $[1\bar{1}0]$ direction (a) and $[11\bar{1}]$ direction (b). The cylinder is assumed to represent the volume from which the information about the local composition is obtained by use of STEM-EELS with a probe size diameter $2r$ of the electron beam.

beam, a compositional profile acquired by use of EELS would yield different results. This is illustrated in Fig. 4.25. The figure shows net counts corresponding to the number of atoms whose lattice position is contained in a cylinder with radius r , placed at different distances from the grain boundary. The data were extracted from a supercell of the $\Sigma 3$ (112) reflectional twin boundary. The supercell comprised ~ 5500 atoms and exhibited dimensions of 7.7 nm in [221] direction, 3.9 nm in $[1\bar{1}0]$ direction, and 3.9 nm in $[11\bar{1}]$ direction. The presented net counts are averages extracted along two different paths. One path contained the two In atomic columns opposing each other across the grain boundary and one path contained the two Cu atomic columns. The curves were also slightly smoothed by use of a binomial filter to compensate for strong fluctuations in the signal arising from the digital distribution of the atoms in combination with the sharp boundaries of the cylinder. Note that the situation is much more complicated in an actual measurement. The signal is not obtained from a cylinder with sharp boundaries, but depends on the electron current density distribution of the electron beam (probe), the applied convergence and collection angles of the microscopic system [142], the thickness of and the total wavefunction of the specimen.

If the radius of the cylinder is much smaller than the smallest interatomic distance, the

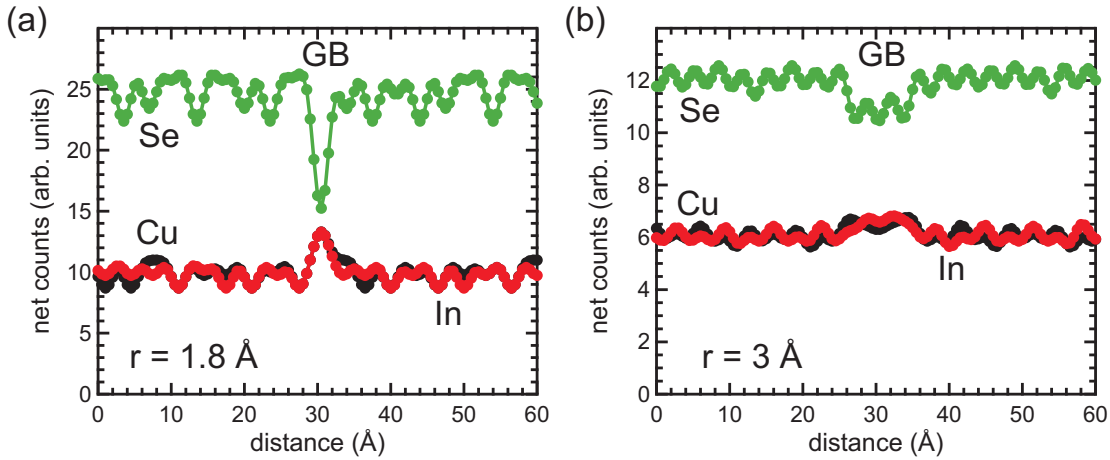


Figure 4.25: Simulation of the local composition across the $\Sigma 3$ (112) reflectional twin boundary in Fig. 4.24. The shown net counts correspond to the number of atoms whose center is contained in a cylinder with radius 1.8 \AA (a) and radius 3 \AA (b) placed at different distances from the grain boundary.

signal represents the composition of the atomic columns, provided these are contained in the cylinder, and is zero in between. The signal in Fig. 4.25(a) was obtained by use of a cylinder with a radius similar to the interatomic distance (1.8 \AA). The curve now represents the average composition of few atomic columns. The Cu and In signals show an increase at the grain boundary, because the local Cu and In atomic densities with respect to the size of the cylinder are increased. The larger the radius, the more the signal smears out. This can be seen in Fig. 4.25(b), which shows the net counts for a cylinder with a radius of 3 \AA . No local increase of the In and Cu signal at the grain boundary can be found in this case. The dip of the Se signal at the grain boundary will also vanish if the radius is further increased. Of course, the orientation of the model system also affects the results of the measurement. However, a misalignment from the edge-on configuration would lead to a spatially broadened signal with a reduced change in the atomic composition at the grain boundary, similarly to the case of the potential wells discussed in Sec. 4.2.4.

This example shows that a local change in composition, which is apparent in the EELS signal, can be explained by geometrical considerations in which a grain boundary consists of two grain surfaces facing each other.

The STEM-EELS results presented in this work were obtained at random grain boundaries without high symmetry and the applied probe size of the electron beam was in the order of the interatomic distance (see Sec. 3.2.7.1 for details on the EELS measurements). In

all compositional profiles obtained by use of STEM-EELS, the In signal and the Cu signal showed an anticorrelated behavior at the grain boundaries, independent of the integral composition of the investigated $\text{Cu}(\text{In},\text{Ga})\text{Se}_2$ thin film. According to this gedankenexperiment, a change in the composition at the grain boundary compared with the grain interior can only be evoked if the stacking sequence changes at the grain boundary. Two grain surfaces terminated at an In rich and Cu deficient plane facing each other across the grain boundary are sufficient to explain an increase of the In signal and a decrease of the Cu signal, as it was found for grain boundaries within the $\text{Cu}(\text{In},\text{Ga})\text{Se}_2$ film with $[\text{Cu}] / ([\text{In}] + [\text{Ga}]) = 0.83$. Vice versa, two grain surfaces terminated at a Cu rich and In deficient plane facing each other across the grain boundary are required to explain the decrease in the In signal and the increase in the Cu signal, which was found to be present at grain boundaries within the $\text{Cu}(\text{In},\text{Ga})\text{Se}_2$ layer exhibiting $[\text{Cu}] / ([\text{In}] + [\text{Ga}]) = 0.43$.

In the CuInSe_2 crystal structure, only the $\{101\}$ family of lattice planes may be considered (out of the low index planes) for such a termination at a plane exhibiting either a Cu rich and In deficient composition or vice versa. Only few, highly symmetric grain boundary models in which two such terminated planes face each other are thinkable. In contrast, the vast majority of low index lattice planes contain In and Cu atoms to same parts. It is therefore unlikely that all investigated random grain boundaries exhibited the described configuration, especially since they generally featured a curvature in their projection. A high symmetry of the investigated random grain boundaries is also unprobable. While one grain was always tilted in a low-index zone axis orientation to obtain atomic resolution for the STEM-EELS measurement, the opposing grains did not exhibit atomic resolution, indicating to be tilted in a high-index zone axis.

With the example of the $\Sigma 3$ (112) reflectional twin boundary in Fig. 4.24, one may argue that a compositional profile across the grain boundary along the path where two Cu (In) atom columns oppose each other, leads to a local increase in the Cu (In) signal and a decrease in the In (Cu) signal. However, the STEM-EELS measurements were performed at regions of interest with an extension of more than one unit cell in parallel to the grain boundary projection. The averaging over this region of interest would result in an increase in both, the Cu and In signal, as shown in Fig. 4.25.

In summary, it is unlikely that local changes in composition, which were measured to be present at random grain boundaries by means of STEM-EELS, originate merely from a geometrical assembly of two crystal lattices.

Minimization of the grain boundary free energy as origin of the measured change in composition

The lattice distortions at a grain boundary may give rise to a local reconstruction of the adjacent lattices to an energetically more favorable configuration. This includes a local reconstruction of the bond lengths as well as a local reconstruction of the composition. Both types of reconstruction may appear as a local change in composition depending on the resolution of the analyzing method and may explain the finding of potential wells.

From a theoretical point of view, such reconstructions are very complex to treat. The bond lengths, the formation of defects, the presence of impurities, as well as resulting excess charges in the environment of the grain boundary are mutually dependent. The problem has to be solved self-consistently from a suitable starting point. One approach to solve this problem are DFT calculations on an initially defined structure. However, this is not possible for random grain boundaries, since the starting point of the local structure is not known. In the case of the $\Sigma 9$ grain boundary that has been investigated in this work, a possible starting point would be the model in Fig. 4.15. Corresponding DFT calculations are already in progress but will not be discussed in the present work.

Defect segregation as origin of the measured change in composition

Another possible explanation for the experimental finding that the local composition is different at the grain boundary, compared with the bulk, is defect segregation. In equilibrium, the minimization of the interfacial free energy of a grain boundary and its environment can be considered as driving force for defect segregation to the grain boundary. In non-equilibrium segregations, e.g. occurring during growth of a polycrystalline material, the diffusion of defects and defect complexes plays an important role [194].

A prerequisite for the following argumentation is the considered absorbers exhibit a composition somewhere on or close to the quasi-binary cut In₂Se₃-Cu₂Se of the phase diagram of the ternary system Cu-In-Se (see Fig. 2.4). Consider a *p*-type Cu(In,Ga)Se₂ thin film similar to the one of the standard absorber ($[Cu]/([In] + [Ga]) = 0.83$, see Tab. 3.1). From the phase diagram in Fig. 2.4, it is obvious that the Cu(In,Ga)Se₂ phase is the dominant one. The most probable defects in the thin films with such a composition are V_{Cu}⁻, In_{Cu}²⁺ [29], and probably V_{Se}²⁺ [27] (see Sec. 2.2.3 for the notation of the defects). Moreover, the phase Cu(In,Ga)₃Se₅ possibly coexists [32]. Ga is not considered at this point since no

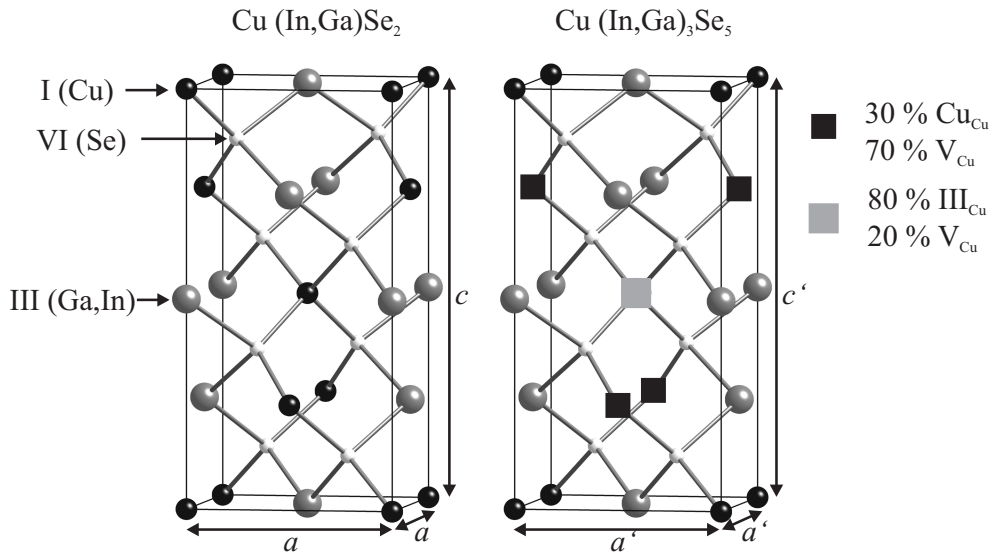


Figure 4.26: Schematics of the unit cell of the Cu_{(In,Ga)Se₂} phase and a model of the unit cell of the Cu_{(In,Ga)₃Se₅} phase according to Zhang et al. [29, 193]. In their model, the Cu_{(In,Ga)₃Se₅} phase can be obtained from the Cu_{(In,Ga)Se₂} phase by removing four units of the defect complex (2V_{Cu}⁻ + III_{Cu}²⁺) from five unit cells of the Cu_{(In,Ga)Se₂} phase. This leads to a structure, in which atomic positions are statistically "occupied" by cations or vacancies. These positions are highlighted by squares. Note that this is only one of few models [177].

changes in the Ga composition could be detected in the present work. Therefore, V_{Cu}⁻, In²⁺_{Cu} antisite defects, V_{Se}²⁺, and corresponding defect complexes can be considered as solute defects in the Cu_{(In,Ga)Se₂} phase. This is illustrated in Fig. 4.26 with the help of a unit cell of the Cu_{(In,Ga)Se₂} phase and a model of the unit cell of the Cu_{(In,Ga)₃Se₅} phase. These defects may segregate at grain boundaries, either in equilibrium to minimize the interfacial free energy of the grain boundaries and its environment, or during growth, where the diffusion of the defects may be enhanced. This would lead to an increase of the local In concentration and a decrease of the local Cu and Se concentrations, as found in the corresponding measurements.

Now, considering the *p*-type absorber exhibiting $[Cu]/([In] + [Ga]) = 0.43$ (see Tab. 3.1), the phase diagram (Fig. 2.4) states clearly that the Cu_{(In,Ga)₃Se₅} phase is the dominating phase and the Cu_{(In,Ga)Se₂} phase coexists. V_{In}³⁻, Cu_{In}²⁻ (also with respect to In already occupying the Cu lattice sites), V_{Se}²⁺, and corresponding defect complexes are solute "defects" in the phase Cu_{(In,Ga)₃Se₅} perturbing its defined statistical occupation of the atomic po-

sitions (see Fig. 4.26). A segregation of these "defects" to grain boundaries may yield a local increase in the Cu concentration, as well as a local decrease in the In and Se concentrations. This has been found to be the case in the corresponding measurement (see Fig. 4.20). The measured Se concentration, however, did not change significantly.

If the integral Cu content in the absorber is between these two cases discussed above, e.g. $[Cu]/([In] + [Ga]) = 0.67$, the phase Cu(In,Ga)Se₂ and the phase Cu(In,Ga)₃Se₅ coexist to similar fractions. Defects with respect to a dominant phase can not be defined in this case. The driving force to improve the purity of the dominating phase may thus be less pronounced as in the case, where one phase dominates over the other. Likewise, it is thinkable that the defects of both phases may segregate to grain boundaries neutralizing each other. The number of segregated defects of the locally dominating phase would then outbalance the number of segregated defects of the other phase to some extent. This may be an explanation for the results on the local composition at a grain boundary within the absorber exhibiting $[Cu]/([In] + [Ga]) = 0.67$ by means of APT, where only the Cu concentration was found to change significantly at the grain boundary, and the finding that the averaged electrostatic potential wells exhibited the smallest depths of all absorbers in the Cu series.

4.4.2.5 Transfer to Ga series and CuInS₂

Unfortunately, no measurements on the local composition across grain boundaries within the Ga series are available, yet. All Cu(In,Ga)Se₂ layers from the Ga series exhibit almost the same integral Cu and Se concentrations as the standard absorber $[Cu]/([In] + [Ga]) = 0.83$ of the Cu series (see Tab. 3.1). One may assume that the behavior of the Cu and Se concentration at the grain boundaries is similar to that found at grain boundaries within the absorber of the Cu series with $[Cu]/([In] + [Ga]) = 0.83$, i.e., the concentration of both elements is reduced. Likewise, the In concentration is expected to be increased at the grain boundaries in both In containing absorbers. However, it can not be estimated whether the Ga concentration is also increased at the grain boundary. The STEM-EELS measurements on grain boundaries within the standard absorber of the Cu series suggest that the potential wells are mainly caused by a Se deficiency. Referring to this finding, the measurements on the electrostatic potential do not aid in the current discussion since all grain boundaries within absorbers with different integral Ga concentration exhibited

similar potential well depths.

Although the standard absorber in the Cu series ($[Cu]/([In] + [Ga]) = 0.83$) exhibits a Ga concentration gradient normal to the substrate, where the concentration changes by about 10 at.%, no dependency of the potential well depths on the distance of the corresponding grain boundary from the substrate was found. This indicates that a substitution of In for Ga, or vice versa, has no significant impact on the potential well depths. Ga and In may therefore behave similar with respect to the local composition at grain boundaries. This is supported by the APT measurements on grain boundaries within the absorber with $[Cu]/([In] + [Ga]) = 0.67$, where no significant change was found for both, the In and the Ga concentration (see Fig. 4.21).

No measurements on the local composition at grain boundaries in CuInS_2 have been performed so far. A major difference of the investigated CuInS_2 absorbers (Fig. 4.5) compared with the $\text{Cu}(\text{In},\text{Ga})\text{Se}_2$ absorbers is that their integral composition exhibits a ratio $[Cu]/([In] + [Ga])$ closer to 1 and that the growth of the layer is different. A simple transfer of the experimental results on $\text{Cu}(\text{In},\text{Ga})\text{Se}_2$ especially with respect to the local Cu and In composition at grain boundaries is therefore not possible at this point. Further measurements on the local composition at grain boundaries within both materials are necessary.

4.4.2.6 Impact of the grain boundary symmetry

The results on the averaged electrostatic potential at grain boundaries exhibiting different geometries was shown in Sec. 4.1.6. Potential wells have been found to be present at a $\Sigma 3$, a $\Sigma 9$, and a random grain boundary. However, the potential well depths increase with decreasing symmetry from the $\Sigma 3$ grain boundary, exhibiting the highest symmetry, to the random grain boundary, exhibiting the lowest symmetry. The results give rise to the assumption that the local lattice perturbations at grain boundaries increase with decreasing symmetry. According to the simulations on structural models of $\Sigma 3$ twin boundaries in Sec. 4.2.4, the geometrical assembly of two grains can not explain the presence of a potential well that has actually been measured at a $\Sigma 3$ grain boundary [92]. Analogous simulations on a simple structural model of a $\Sigma 9$ grain boundary yielded a slightly more pronounced potential well than measured. Since the redistribution of free charge carriers was excluded as sole origin for the potential wells, this indicates that local changes in composition may as well contribute to the potential wells in both cases.

The significant changes in composition measured at a random grain boundary within the standard absorber of the Cu series give rise to the presence of potential wells with a depth of more than 3 V (see Tab. 4.7). This is much deeper than the measured potential well depths at the $\Sigma 9$ and especially at the $\Sigma 3$ grain boundary. This indicates that a grain boundary exhibiting a lower symmetry involves a more distinct change in composition than a grain boundary exhibiting a higher symmetry. The degree of a local compositional change seems to depend on the symmetry of the grain boundary.

From another point of view, a grain boundary exhibiting a high symmetry already gives rise to less compositional changes in the local crystal lattice than one exhibiting a lower symmetry. For example, the free energy of the $\Sigma 3$ (112) 180° rotational twin boundary in Fig. 4.15 is expected to be close to the free energy of the perfect lattice since the distortions of the bond lengths across the grain boundary are small. Hence, the driving force for a local change in composition is small. In contrast, at least some atomic bonds across the $\Sigma 9$ (111) 180° rotational twin boundary in Fig. 4.15 must be distorted, since the distance between nearest neighbors (across the grain boundary) changes with position. The minimization of the free energy of the distorted crystal is then the driving force for a local change in composition at and close to the grain boundary.

4.5 Grain boundary model

The aim of this section is to combine the previous findings in order to propose a model for the electrical properties of grain boundaries within Cu(In,Ga)Se₂ and related thin film absorbers with respect to the electronic band diagram.

Unfortunately, it is not generally possible to determine the electronic band structure, comprising two electronic bands, based on only one quantity, the averaged electrostatic potential. Only if changes in the averaged electrostatic potential are caused by a redistribution of free charge carriers, the band bending of the valence and conduction band is proportional to the $-e \Delta V_a(\vec{r})$ (see Sec. 4.2.1.2). Since a redistribution of free charge carriers owing to a bound grain boundary excess charge was excluded as origin of the measured potential wells, the potential distribution can not be transferred directly to the electronic band diagram by a simple corresponding local band bending. A change in the local crystal structure and consequently on the band-gap energy, including shifts of the bands, seem probable.

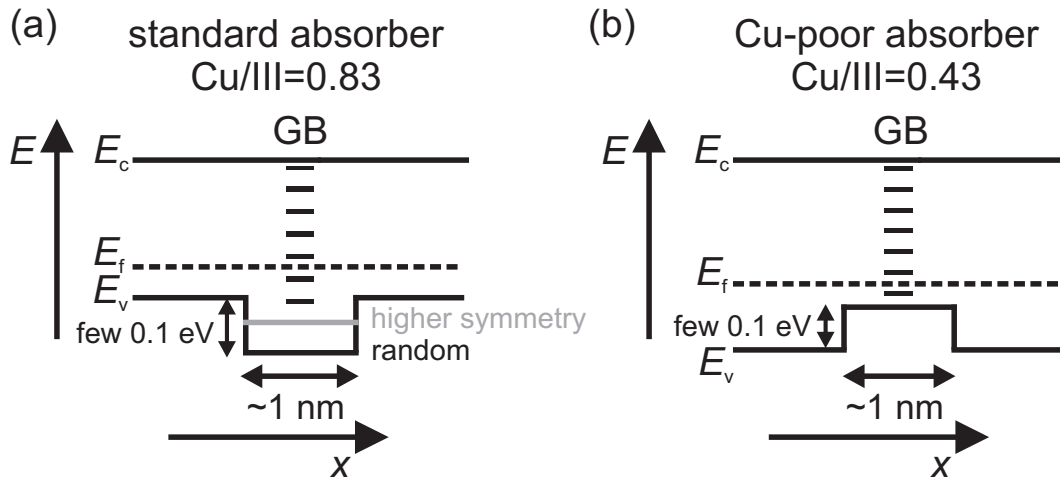


Figure 4.27: Schematics of the local electronic band diagram (in equilibrium) at grain boundaries in the standard absorber ($[Cu]/([In] + [Ga]) = 0.83$) (a) and the absorber exhibiting $[Cu]/([In] + [Ga]) = 0.43$ (b). A possible defect distribution within the band gap is denoted by a sequence of dashes. The band bendings in the vicinity of the shown details can not be estimated based on the presented results and are disregarded here. The chosen positions of the Fermi level in the band gaps correspond to the case without band bending.

First, the compositional changes at grain boundaries are considered. At grain boundaries within the standard $\text{Cu}(\text{In},\text{Ga})\text{Se}_2$ absorber ($[Cu]/([In] + [Ga]) = 0.83$), a decrease of the Cu and Se concentrations, as well as an increase of the In concentration was found. The change in composition occurs in a region of about 1 nm at the grain boundary. According to Zhang et al. [29] and Persson et al. [33, 34], a local decrease in the Cu concentration and a local increase of the In concentration in $\text{Cu}(\text{In},\text{Ga})\text{Se}_2$ is accompanied by a modification of the electronic band diagram, i.e., the valence-band maximum is shifted to lower energies (see Fig. 2.5). Fig. 4.27(a) shows the corresponding schematics. The less significant impact on the conduction band edge is neglected at this point to keep the model simple. Note that any effect of the strongly reduced Se concentration can not be considered here since no corresponding DFT calculations are currently available in the literature. There are, however, indications that the strong decrease of the Se concentration of about 50 % is due to a preferential damage of the grain boundary during a plasma cleaning procedure before the measurement. This may have led to a substitution of Se for the isovalent O, which was also found to be present. In contrast, no O and no significant change in

the Se concentration was found at grain boundaries within the other two specimens of the Cu series. It is therefore assumed, at this point, that the actual decrease of the Se concentration at grain boundaries is not as pronounced as detected. This assumption justifies the proposed model.

In contrast, grain boundaries in absorbers with a very Cu poor and In rich composition ($[Cu]/([In] + [Ga]) = 0.43$, see Tab. 3.1) exhibited a Cu enrichment and an In depletion, likewise in a region of about 1 nm at the grain boundary, while the Se concentration did not change significantly. Regarding the In and Cu concentration, the situation is inverse to grain boundaries within the standard absorbers. It is therefore proposed that the valence-band maximum within this absorber is lower compared with the standard absorber, and that it is shifted to higher energies at grain boundaries. A schematics of this model is depicted in Fig. 4.27(b).

If the integral composition of the absorber is in between both extremes, the valence-band offsets may be less distinct and either positive or negative, depending on the exact composition. Note that this model neglects strain and a change in the ionicity of the atomic bonds, which may be present at grain boundaries in addition to changes in composition.

Next, the effect of the grain boundary symmetry is considered. It was shown in Sec. 4.1.6 and Sec. 4.4.2.6 that the symmetry of grain boundaries in Cu(In,Ga)Se₂ thin films with composition close to the standard absorber affects the depths of the corresponding averaged electrostatic potential wells and, very likely, the degree of the local change in composition. Local changes in composition and hence the valence-band offset at grain boundaries are expected to be less significant if their symmetry is higher. This is depicted in Fig. 4.27(a).

Now, the effect of bound grain boundary charge is addressed. Most of the previous studies suggest a slight downward bending of the electronic bands towards the grain boundaries in Cu(In,Ga)Se₂ and CuInS₂ absorbers in equilibrium, which corresponds to the presence of potential barriers. Owing to the perturbation of the potential distribution by the electron beam during the inline electron holography measurements, it was not possible to estimate an upper limit for a bound charge carrier density—in terms of charged defects—which is possibly present at grain boundaries in equilibrium (see Sec. 4.2.1.3). Even if the electron current density of the electron beam is adjusted to a minimum and the semiconductor is close to equilibrium, potential barriers of about 0.83 V (Cu(In,Ga)Se₂) and 0.13 V (CuInS₂) are below the detection limit (see Tab. 4.4). These values are larger than the ones of at most 0.35 V (Cu(In,Ga)Se₂) [107–110] and 0.06 V (CuInS₂) [26] discussed in the literature,

and do not confine them. The presence of potential wells below the detection limit could likewise not be ruled out. The band bending of the valence and conduction band is therefore not illustrated in Fig. 4.27.

In conclusion, the model for grain boundaries within the standard absorber of the Cu series ($[\text{Cu}] / ([\text{In}] + [\text{Ga}]) = 0.83$) is compatible with the model of space charge and an additional neutral tunneling barrier at grain boundaries (see Sec. 2.3.2.4) as well as with the model of the simple valence band offset (see Sec. 2.3.2.2). However, assuming that an energetic defect distribution within the band gap is present at random grain boundaries, which is probable due to the local perturbation of the perfect crystal lattice, the absence of bound excess charge seems unrealistic. This would require a very special defect distribution such that the Fermi level has the same energetic distance to the conduction band at the grain boundary and in the grain interior. The model of benign grain boundaries (see Sec. 2.3.2.1) seems to be too simple to be applicable for random grain boundaries, since it is based on DFT calculations on a highly symmetric $\Sigma 3$ grain boundary, for which only lattice relaxation but no compositional change was allowed. Similarly, the Seto model (see Sec. 2.3.2.3), which only considers a redistribution of free charge carriers, is supposed to be too simple with respect to the changes in composition and the lowering of the averaged electrostatic potential that were found at grain boundaries in the present work. The model proposed in the case of a very Cu poor absorber ($[\text{Cu}] / ([\text{In}] + [\text{Ga}]) = 0.43$), with a composition close to the phase $\text{Cu}(\text{In},\text{Ga})_3\text{Se}_5$, is based on the same concept, i.e., a local change in composition influences the band-gap energy. However, this is the first grain boundary model to be proposed for such absorbers.

The impact of the grain boundary model on the corresponding solar cells is now briefly discussed. Grain boundaries exhibiting an electronic defect distribution within the band gap give rise to a higher net recombination rate of free charge carriers compared with the grain interior under illumination, thus leading to a decrease of the conversion efficiency of the corresponding solar cell. Two-dimensional device simulations on $\text{Cu}(\text{In},\text{Ga})\text{Se}_2$ solar cells including grain boundaries showed that a valence-band shift of a few hundred meV to lower energies may reduce the recombination rate at grain boundaries, leading to an improvement of the conversion efficiency [82, 195]. This is since such a valence-band offset at grain boundaries reduces the local free hole density within the valence band, leaving less available states for the free electrons within the conduction band. The degree of the beneficial effect, however, depends on the balance of the offset value, its spatial width, the

properties of the defect distribution, as well as the orientation of the grain boundaries [195]. Valence-band offsets at grain boundaries parallel to the substrate act as a hole transport barrier (see Fig. 4.27(a)) and, if too large, hinder the current transport significantly. If the offset or its width is too small, free holes may either be thermionically emitted above the barrier or tunnel through the barrier, leaving the recombination rate unaffected. In summary, however, this means that the grain boundary model shown in Fig. 4.27(a) may account for the high conversion efficiency of Cu(In,Ga)Se₂ solar cells compared with other polycrystalline thin film solar cells. It is not obvious how the grain boundary symmetry affects the solar cell efficiency since the energetic defect distribution as well as the valence-band offset must be considered.

On the contrary, a valence-band shift to higher energies at grain boundaries, as proposed in the case of the absorber exhibiting $[Cu]/([In] + [Ga]) = 0.43$ (see Fig. 4.27(b)), leads to an increased recombination rate at grain boundaries. Unfortunately, no simulations have been performed on that issue yet. However, this is expected to lead to a reduced conversion efficiency of the corresponding solar cells since the situation is inverse to the one in Fig. 4.27(a). The grain boundary properties of this absorber may therefore account to some parts for the inferior conversion efficiency of the corresponding solar cell of about 9.5 %, compared with the conversion efficiency of the standard absorber ($[Cu]/([In] + [Ga]) = 0.83$) of about 14.8 %.

4.6 Summary of grain boundaries in Cu(In,Ga)Se₂ and CuInS₂ thin films studied by TEM

In this chapter, grain boundaries in Cu(In,Ga)Se₂ and CuInS₂ absorbers were investigated by use of electron holography and STEM-EELS. The integral absorber composition, as well as the grain boundary type were varied in order to study the dependence of the grain boundary properties on the composition and the symmetry. This approach yielded the following results:

- A lowering of the averaged electrostatic potential in a region of 1 – 2 nm and a depth of 0.2 – 3 V was present at all grain boundaries studied. The depths of these potential wells depend strongly on the type of the grain boundary, i.e., its symmetry, and, less distinct, on the integral absorber composition. The lower the symmetry,

the deeper the potential wells. While the potential well depths varied strongly from grain boundary to grain boundary, even in identical layers, random grain boundaries generally exhibited the deepest potential wells.

- Estimations and numerical simulations on the screening of a bound grain boundary charge showed that a redistribution of free charge carriers close to the grain boundary does not contribute significantly to the potential wells (see Sec. 4.2.1.2). Possible contributions are a local change in composition, in ionicity of the atomic bonds, and in the atomic density. A reduced atomic density may be evoked by a local reconstruction of the lattice or from mere geometrical considerations if two adjacent grains, each grain terminated by a plane, are assembled. Multislice simulations showed that the latter may contribute significantly to a lowering of the averaged electrostatic potential since the simulated potential wells were even deeper than the measured ones (see Sec. 4.2.4).
- The presence of space charge or excess charge layers screening the electric field of a bound excess charge at grain boundaries during the measurement could not be excluded. The electrostatic contribution to the strain of corresponding potential distributions below the detection limit, however, was estimated to give an insignificant contribution to a change in the averaged electrostatic potential.
- In the case of the highest applied electron current density during the electron holography measurements, the generation of free charge carriers by the electron beam was found to perturb the potential distribution caused by mobile charge carriers significantly. This is one reason why an estimation of the presence of excess charge at grain boundaries in equilibrium was not possible. Another reason is the detection limit of the inline electron holography as applied in the present work (see Sec. 4.2.1.3).
- The presence of the averaged electrostatic potential wells at grain boundaries was found to be correlated with a local change in composition. It was estimated that these changes in composition give indeed rise to a major contribution to the potential wells.
- The local change in composition at grain boundaries strongly depends on the integral composition of the absorbers. In the standard absorber ($[Cu]/([In] + [Ga]) = 0.83$),

grain boundaries exhibited an increased In concentration, while the Cu and Se concentrations were reduced. Grain boundaries within absorbers exhibiting a composition close to the Cu(In,Ga)₃Se₅ phase ($[Cu]/([In] + [Ga]) = 0.43$) showed an increased Cu concentration, while the In concentration was decreased. The Se concentration did not change significantly.

- The local Cu and In concentrations showed anticorrelated behavior at all investigated grain boundaries, independently of the integral composition of the absorber. Based on symmetry considerations, this finding can hardly be explained by a pure geometrical model of the grain boundary. A local lattice reconstruction with respect to the local composition is much more probable.
- Based on the experimental findings and on published DFT calculations, a grain boundary model was established for the standard absorbers ($[Cu]/([In] + [Ga]) = 0.83$) and for an absorber exhibiting $[Cu]/([In] + [Ga]) = 0.43$. The model for grain boundaries within the standard absorber involves a valence-band shift to lower energies at the grain boundary, which is less pronounced if the grain boundary is highly symmetric. It is in agreement with the model of space charge and an additional neutral tunneling barrier at grain boundaries (see Sec. 2.3.2.4) as well as with the model of a simple valence band offset (Sec. 2.3.2.2). The two other models, i.e., the model of benign grain boundaries (see Sec. 2.3.2.1) and the model of Seto (see Sec. 2.3.2.3), do not take into account a strong change in the local composition. It was further proposed that a shift of the valence band edge to higher energies is present at grain boundaries within the absorber exhibiting $[Cu]/([In] + [Ga]) = 0.43$.

Chapter 5

Concluding remarks and outlook

The aim of the present work was to gain a deeper insight into the properties of grain boundaries within polycrystalline Cu(In,Ga)Se₂ and CuInS₂ layers applied as absorber layers in highly efficient thin-film solar cells. For this purpose, the microscopic properties of grain boundaries from the few 10 nm range down to the Å range have been studied. In the following, the most important results as well as conclusions are summarized, and next steps are suggested.

In general, the local Coulomb potential at and in the vicinity of grain boundaries plays a significant role in the current transport properties of any polycrystalline material. Electron holography in transmission electron microscopy allows a direct measurement of the Coulomb potential on a microscopic scale from the μm range down to the nm range. By use of this method, it was shown that the Coulomb potential, averaged parallel to the plane of the grain boundary, is reduced in an 1 – 2 nm wide region at the grain boundaries by up to 0.2 – 3 V. While the widths of these potential wells were always similar, their depths varied between individual grain boundaries, even within the same layer, with the integral composition of the absorber, and the symmetry of the grain boundaries. The higher the grain boundary symmetry, the less pronounced was the measured potential well.

A redistribution of free charge carriers screening the electric field of a bound grain boundary charge was excluded as a main contribution to the potential wells (see Sec. 4.2.1.2). However, it was found that the electron beam (in TEM) may perturb the potential distribution caused by a redistribution of free charge carriers significantly due to a generation of additional free charge carriers with a density of up to 10^{16} cm^{-3} , which is in the order of

magnitude of the doping density of Cu(In,Ga)Se₂. The presence of a bound excess charge carrier density of about $N_i = 10^{12} \text{ cm}^{-2}$ at grain boundaries during the measurement is compatible with the measurement results. Even if this value can be transferred to the equilibrium state without the perturbation by the electron beam (in TEM), this is higher than bound charge carrier densities discussed in the literature and is therefore not a significant confinement [26, 107–110]. Owing to the high spatial coherence, further off-axis electron holography measurements on the Coulomb potential at grain boundaries within polycrystalline Cu(In,Ga)Se₂ and CuInS₂ layers may provide better estimates of the magnitudes of possible bound charge carrier densities. However, the generation of free charge carriers by the electron beam has to be kept at a minimum.

Significant contributions to the measured potential wells may arise from local distortions of the lattice. These comprise a reduced atomic density owing to the grain boundary geometry or owing to a relaxation of the interatomic bonds and a correlated change in the ionicity of the bonds, as well as a reconstruction of the grain boundary structure and its vicinity, including compositional changes. With the help of a structural $\Sigma 9$ grain boundary model and multislice simulations, it was shown that the geometrical assembly of two perfect crystal lattices, each lattice terminated by a plane, may cause a significantly reduced local atomic density at the grain boundary and a corresponding lowering of the averaged electrostatic potential. The presence of surface grooves at the grain boundary vacuum interface was not investigated experimentally. Further AFM or STM measurements are required to study this issue.

By use of STEM-EELS, the presence of potential wells at grain boundaries was correlated with a local change in composition occurring within a similar range (1 – 2 nm). The change in composition was estimated to contribute significantly to the potential wells (see Sec. 4.4.2.1). However, there may be further contributions. The contributions of a lattice relaxation, a change in ionicity, and a reconstruction of the local crystal lattice to the potential wells at grain boundaries could not be estimated in the present work. A comparison of the performed measurements with DFT calculations is required to evaluate the possible scenarios described above. Such DFT calculations are already in progress in the case of the $\Sigma 9$ grain boundary studied in the present work. It is further suggested to perform HRTEM at the $\Sigma 9$ grain boundary by use of a C_s corrected TEM to estimate a possible change in the local atom density and to obtain an adequate structural model.

The local composition change at random grain boundaries was found to depend strongly on

the integral composition of the absorbers. In the standard absorber ($[Cu]/([In] + [Ga]) = 0.83$), grain boundaries exhibited a Cu and a strong Se deficiency, as well as an In enrichment. In the absorber with composition close to that of the $Cu(In,Ga)_3Se_5$ phase ($[Cu]/([In] + [Ga]) = 0.43$), Cu was enriched at the grain boundary, while In was deficient, and Se did not change significantly. The In and Cu concentrations at grain boundaries exhibited an anticorrelated behavior at all grain boundaries studied. Based on this finding, it was concluded that the changes in composition measured by use of EELS may not arise from a geometrical assembly of two grains alone (see Sec. 4.4.2.4). A local lattice reconstruction in terms of a change in composition is more probable. As the evaluation of the local Ga and Na concentrations is difficult by use of EELS, it might be advantageous to determine local changes in composition at grain boundaries by use of energy dispersive X-ray spectroscopy in STEM mode using a C_s corrected TEM.

The role of the impurity atoms Na and O is not clear. O was only found at a grain boundary within the standard absorber ($[Cu]/([In] + [Ga]) = 0.83$). The Na concentration measured by use of APT at a grain boundary within the absorber exhibiting $[Cu]/([In] + [Ga]) = 0.67$ was about 2 at.%, which is much too small to contribute significantly to the potential wells. However, the impurities, even if only present in a small atomic concentration, may be involved in neutralizing a possible bound grain-boundary charge.

A local reconstruction of the crystal lattice at grain boundaries and defect segregation were proposed as possible causes for the detected change in composition. The former may be tested with the aid of DFT calculations, which are currently performed. Moreover, modeling of the defect segregation in either equilibrium or non equilibrium may give further insight into the origin of the changes in composition. In this context, it has to be considered that Cu is highly mobile in $Cu(In,Ga)Se_2$ and may respond to bound grain boundary charges by electromigration, as proposed for surfaces [196]. Additional measurements on the local compositions at grain boundaries within $Cu(In,Ga)Se_2$ absorbers exhibiting $[Cu]/([In] + [Ga]) > 1$ may also assist in understanding whether a defect segregation is the cause of the compositional changes.

Combining the results, a model was proposed describing the electronic band diagram at grain boundaries within $Cu(In,Ga)Se_2$ absorbers exhibiting $[Cu]/([In] + [Ga]) = 0.83$ and $[Cu]/([In] + [Ga]) = 0.43$. The model is similar to those based on DFT calculations [29, 33, 34], suggesting a lowering of the valence-band maximum upon a decrease in the local Cu and an increase in the local In concentrations. In the case of absorbers with $[Cu]/([In] + [Ga]) =$

0.83, such a lowering of the valence-band maximum was proposed to be present in an about 1 nm wide region around the grain-boundary core. The magnitude of this valence-band offset was suggested to decrease with an increasing grain boundary symmetry. Device simulations by Taretto et al. [195] and Gloeckler et al. [82] showed that such a valence-band offset may account for an effective passivation of grain boundaries, leading to an improvement of the conversion efficiency of the corresponding solar cells compared with the case without the offset. The grain boundary properties revealed in the present work may therefore explain the superior conversion efficiency of Cu(In,Ga)Se₂ thin-film solar cells compared with other polycrystalline thin-film solar cells.

For the first time, a grain boundary model was proposed for absorbers with composition close to the phase Cu(In,Ga)₃Se₅. In this case (absorber with $[Cu]/([In] + [Ga]) = 0.43$), a valence-band maximum shift to higher potential energies was suggested to be present at grain boundaries. Such an offset is expected to reduce the solar cell conversion efficiency. This may account to some parts for the inferior conversion efficiency of the corresponding solar cell compared with the absorber with composition of $[Cu]/([In] + [Ga]) = 0.83$.

Appendix A

Wave aberration function

The wave aberration function is given by [120, 123, 147]

$$\begin{aligned} \chi(\vec{q}, \Delta f) = & 2\pi k \left[\frac{1}{2} \Delta f \left(\frac{q}{k} \right)^2 \right. && \text{defocus} \\ & + \frac{1}{2} A_2 \left(\frac{q}{k} \right)^2 \cos(2(\alpha - \alpha_{A_2})) && \text{twofold astigmatism} \\ & + \frac{1}{3} B \left(\frac{q}{k} \right)^3 \cos(\alpha - \alpha_B) && \text{axial coma} \\ & + \frac{1}{3} A_3 \left(\frac{q}{k} \right)^3 \cos(3(\alpha - \alpha_{A_3})) && \text{threefold astigmatism} \\ & + \frac{1}{4} C_s \left(\frac{q}{k} \right)^4 && \text{spherical aberration} \\ & \left. + \dots \right], && \end{aligned} \tag{A.1}$$

where C_s is the spherical aberration coefficient, A_2 and A_3 the two- and threefold astigmatism coefficient, and B the axial coma coefficient. \vec{q} is expressed by its modulus q and the azimuth angle of the vector \vec{q} . α_{A_2} and α_{A_3} are azimuth angle offsets.

The envelope functions may be described as [147]

$$E^{\text{sc}}(\vec{q}) = \exp \left(- \left(\frac{k\theta_{\text{coh}}}{2} \right)^2 (\nabla \chi(\vec{q}, \Delta f))^2 \right) \tag{A.2}$$

$$E^{\text{tc}}(\vec{q}) = \exp\left(-\frac{1}{2}\left(\frac{\pi\Delta}{k}\right)^2 q^4\right) \quad (\text{A.3})$$

and

$$E^{\text{ap}}(\vec{q}) = \begin{cases} 1 & \text{for } q \leq q_{\max} \\ 0 & \text{else} \end{cases}, \quad (\text{A.4})$$

where θ_{coh} is the illumination aperture half width, and Δ is the focal spread. By use of the energy spread ΔE of the beam electrons, the instability ΔU of the acceleration voltage U , and the instability ΔI of the electromagnetic lens current I , Δ is given by

$$\Delta = C_c \sqrt{\left(\frac{\Delta E}{eU}\right)^2 + \left(\frac{\Delta U}{U}\right)^2 + \left(\frac{2\Delta I}{I}\right)^2}, \quad (\text{A.5})$$

where C_c is the chromatic aberration coefficient.

Appendix B

Transmission cross coefficient

The transmission cross coefficient is given by [134]

$$\begin{aligned} \text{TCC}(\vec{q}', \vec{q}'') &= \iint H(\delta f) F(\vec{q}_{\text{ill}}) \\ &\times \exp(-i(\chi(\vec{q}' + \vec{q}_{\text{ill}}, \Delta f' + \delta f) - \chi(\vec{q}'' + \vec{q}_{\text{ill}}, \Delta f'' + \delta f))) d\vec{q}_{\text{ill}} d\delta f, \end{aligned} \quad (\text{B.1})$$

where $\vec{q}_{\text{ill}} = k\vec{\alpha}$ is the illumination direction, and $\vec{q}' = \vec{q} + \vec{q}''$. $F(\vec{q}_{\text{ill}})$ and $H(\delta f)$ are normalized distribution functions describing the angular distribution of the illumination source and the focal spread. If the angular distribution of the illumination can be described by a Gaussian function, the focal spread is zero, and the aberration function comprises only the defocus and the spherical aberration terms, see Appendix Sec. A, then the TCC may be approximated by [134]

$$\begin{aligned} \text{TCC}(q', q'') &= \exp\left(-\left(\frac{k\theta_{\text{coh}}}{2}\right)^2 \left(\frac{\delta\chi(q', \Delta f)}{\delta q'} - \frac{\delta\chi(q'', \Delta f)}{\delta q''}\right)^2\right) \\ &\times \exp(-i(\chi(q', \Delta f) - \chi(q'', \Delta f))). \end{aligned} \quad (\text{B.2})$$

If only the defocus term of the aberration function is considered in the first term, this yields

$$\begin{aligned} \text{TCC}(q', q'') &= \exp(-(\pi\theta_{\text{coh}}\Delta f q)^2) \\ &\times \exp(-i(\chi(q', \Delta f) - \chi(q'', \Delta f))). \end{aligned} \quad (\text{B.3})$$

Bibliography

- [1] M. A. Green, K. Emery, Y. Hishikawa, and W. Warta. Solar cell efficiency tables (version 37). *Prog. Photovolt: Res. Appl.*, 19(1):84–92, 2011.
- [2] S. Chichibu, T. Mizutani, K. Murakami, T. Shioda, T. Kurafuji, H. Nakanishi, S. Niki, P. J. Fons, and A. Yamada. Band gap energies of bulk, thin-film, and epitaxial layers of CuInSe₂ and CuGaSe₂. *J. Appl. Phys.*, 83(7):3678–3689, April 1998.
- [3] M. I. Alonso, K. Wakita, J. Pascual, M. Garriga, and N. Yamamoto. Optical functions and electronic structure of CuInSe₂, CuGaSe₂, CuInS₂, and CuGaS₂. *Phys. Rev. B*, 63(7):075203–, January 2001.
- [4] H. Neumann, W. Hörig, V. Savelev, J. Lagzdonis, B. Schumann, and G. Kühn. The optical properties of CuInS₂ thin films. *Thin Solid Films*, 79(2):167–171, May 1981.
- [5] P. Würfel and U. Würfel. *Physics of Solar Cells*. WILEY-VCH, Weinheim, 2009.
- [6] R. L. Anderson. Germanium-Gallium Arsenide Heterojunctions. *IBM Journal of Research and Development*, 4(3):283–287, 1960.
- [7] R. L. Anderson. Experiments on Ge-GaAs heterojunctions. *Solid-State Electronics*, 5(5):341–351, September 1962.
- [8] T. Löher, W. Jaegermann, and C. Pettenkofer. Formation and electronic properties of the CdS/CuInSe₂ (011) heterointerface studied by synchrotron-induced photoemission. *J. Appl. Phys.*, 77(2):731–738, January 1995.
- [9] S.-H. Wei and A. Zunger. Band offsets at the CdS/CuInSe₂ heterojunction. *Appl. Phys. Lett.*, 63(18):2549–2551, November 1993.

- [10] B. Johnson, L. Korte, T. Lussky, J. Klaer, and I. Lauermann. CuInS₂–CdS heterojunction valence band offset measured with near-UV constant final state yield spectroscopy. *J. Appl. Phys.*, 106(7):073712–6, October 2009.
- [11] Y. Hashimoto, K. Takeuchi, and K. Ito. Band alignment at CdS/CuInS₂ heterojunction. *Appl. Phys. Lett.*, 67(7):980–982, August 1995.
- [12] R. Klenk. Characterisation and modelling of chalcopyrite solar cells. *Thin Solid Films*, 387(1-2):135–140, 2001.
- [13] L. Pauling. The nature of the chemical bond. Application of results obtained from the quantum mechanics and from a theory of paramagnetic susceptibility to the structure of molecules. *J. Am. Chem. Soc.*, 53(4):1367–1400, April 1931.
- [14] H. G. Grimm and A. Sommerfeld. Über den Zusammenhang des Abschlusses der Elektronengruppen im Atom mit den chemischen Valenzzahlen. *Zeitschrift für Physik A Hadrons and Nuclei*, 36(1):36–59, 1926.
- [15] J. L. Shay, B. Tell, H. M. Kasper, and L. M. Schiavone. p-d Hybridization of the Valence Bands of I-III-VI₂ Compounds. *Phys. Rev. B*, 5(12):5003–, June 1972.
- [16] J. E. Jaffe and Alex Zunger. Electronic structure of the ternary chalcopyrite semiconductors CuAlS₂, CuGaS₂, CuInS₂, CuAlSe₂, CuGaSe₂, and CuInSe₂. *Phys. Rev. B*, 28(10):5822–, November 1983.
- [17] K. S. Knight. The crystal structures of CuInSe₂ and CuInTe₂. *Materials Research Bulletin*, 27(2):161–167, February 1992.
- [18] S. C. Abrahams and J. L. Bernstein. Piezoelectric nonlinear optic CuGaS₂ And CuInS₂ crystal structure: sublattice distortion In A^IB^{III}C₂^{VI} and A^{II}B^{IV}C₂^V type chalcopyrites. *J. Of Chem. Phys.*, 59(10):5415–5422, 1973.
- [19] S. C. Abrahams and J. L. Bernstein. Piezoelectric nonlinear optic CuGaSe₂ and CdGeAs₂: Crystal structure, chalcopyrite microhardness, and sublattice distortion. *J. Chem. Phys.*, 61(3):1140–1146, 1974.
- [20] C. Persson. Anisotropic hole-mass tensor of CuIn_{1-x}Ga_x(S,Se)₂: Presence of free carriers narrows the energy gap. *Appl. Phys. Lett.*, 93(7):072106–3, August 2008.
- [21] S.-H. Wei and A. Zunger. Band offsets and optical bowings of chalcopyrites and Zn-based II-VI alloys. *J. Appl. Phys.*, 78(6):3846–3856, September 1995.

- [22] W. Shockley and H. J. Queisser. Detailed Balance Limit of Efficiency of p-n Junction Solar Cells. *J. Appl. Phys.*, 32(3):510–519, March 1961.
- [23] S.-H. Wei, S. B. Zhang, and A. Zunger. Effects of Ga addition to CuInSe₂ on its electronic, structural, and defect properties. *Appl. Phys. Lett.*, 72(24):3199–3201, June 1998.
- [24] S. Siebentritt, M. Igalson, C. Persson, and S. Lany. The electronic structure of chalcopyrites—bands, point defects and grain boundaries. *Prog. Photovolt: Res. Appl.*, 18(6):390–410, 2010.
- [25] T. Meyer. *Reversible Relaxationsphänomene im elektrischen Transport von Cu(In,Ga)Se₂*. PhD thesis, Universität Oldenburg, 1999.
- [26] L. L. Kazmerski, M. S. Ayyagari, and G. A. Sanborn. CuInS₂ thin films: Preparation and properties. *J. Appl. Phys.*, 46(11):4865–4869, November 1975.
- [27] H. Neumann. Vacancy formation enthalpies in A^IB^{III}C₂^{VII} chalcopyrite semiconductors. *Cryst. Res. Technol.*, 18(7):901–906, 1983.
- [28] S. Fiechter, Y. Tomm, K. Diesner, and T. Weiss. Homogeneity Ranges, Defect Phases and Defect Formation Energies in A^IB^{III}C₂^{VII} Chalcopyrites (A = Cu; B = Ga, In; C = S, Se). *Jpn. J. Appl. Phys.*, 39-1:123–126, 2000.
- [29] S. B. Zhang, Su-Huai Wei, Alex Zunger, and H. Katayama-Yoshida. Defect physics of the CuInSe₂ chalcopyrite semiconductor. *Phys. Rev. B*, 57(16):9642–9656, April 1998.
- [30] A. Klein and W. Jaegermann. Fermi-level-dependent defect formation in Cu-chalcopyrite semiconductors. *Appl. Phys. Lett.*, 74(16):2283–2285, April 1999.
- [31] I. Dirnstorfer, Mt. Wagner, D. M. Hofmann, M. D. Lampert, F. Karg, and B. K. Meyer. Characterization of CuIn(Ga)Se₂ Thin Films. *phys. stat. sol. (a)*, 168(1):163–175, 1998.
- [32] T. Gödecke, T. Haalboom, and F. Ernst. Phase equilibria of Cu-In-Se I. Stable states and nonequilibrium states of the In₂Se₃-Cu₂Se subsystem. *Zeitschrift Für Metallkunde*, 91(8):622–634, August 2000.

- [33] C. Persson and A. Zunger. Anomalous Grain Boundary Physics in Polycrystalline CuInSe₂: The Existence of a Hole Barrier. *Phys. Rev. Lett.*, 91(26):266401–, December 2003.
- [34] C. Persson and A. Zunger. Compositionally induced valence-band offset at the grain boundary of polycrystalline chalcopyrites creates a hole barrier. *Applied Physics Letters*, 87(21):211904, 2005.
- [35] D. Schmid, M. Ruckh, F. Grunwald, and H. W. Schock. Chalcopyrite/defect chalcopyrite heterojunctions on the basis of CuInSe₂. *J. Appl. Phys.*, 73(6):2902–2909, March 1993.
- [36] H. Mönig, C. H. Fischer, R. Caballero, C. A. Kaufmann, N. Allsop, M. Gorgoi, R. Klenk, H. W. Schock, S. Lehmann, M. C. Lux-Steiner, and I. Lauermann. Surface Cu depletion of Cu(In,Ga)Se₂ films: An investigation by hard X-ray photoelectron spectroscopy. *Acta Materialia*, 57(12):3645–3651, July 2009.
- [37] S. M. Wasim, C. Rincon, G. Marin, and J. M. Delgado. On the band gap anomaly in I–III–VI₂, I–III₃–VI₅, and I–III₅–VI₈ families of Cu ternaries. *Applied Physics Letters*, 77(1):94–96, 2000.
- [38] G. B. Abdullaev, Z. A. Aliyarova, and G. A. Asadov. Preparation of Cu₂Se Single Crystals and Investigation of their Electrical Properties. *phys. stat. sol. (b)*, 21(2):461–464, 1967.
- [39] K. G. Kerimov, A. M. Musaev, F. Y. Aliev, A. G. Rustamov, and E. I. Manafly. Investigation of the electrical properties of Cu₂Se single crystals at low temperatures. *phys. stat. sol. (a)*, 5(3):K191–K193, 1971.
- [40] M. Bodegard and L. Stolt. Influence of sodium on the Grain structure of CuInS₂ films for photovoltaic applications. In *12th European Photovoltaic Solar Energy Conference*, 1994.
- [41] J. Holz, F. Karg, and H. von Philipsborn. The effect of substrate impurities on the electronic conductivity in cis thin films. In *12th European Photovoltaic Solar Energy Conference*, 1994.
- [42] K. Granath, M. Bodegard, and L. Stolt. The effect of NaF on Cu(In,Ga)Se₂ thin film solar cells. *Sol. Energy Mater. Sol. Cells*, 60(3):279–293, January 2000.

- [43] D. Rudmann, G. Bilger, M. Kaelin, F. J. Haug, H. Zogg, and A. N. Tiwari. Effects of NaF coevaporation on structural properties of Cu(In,Ga)Se₂ thin films. *Thin Solid Films*, 431-432:37–40, May 2003.
- [44] R. Kimura, T. Mouri, T. Nakada, S. Niki, Y. Lacroix, T. Matsuzawa, K. Takahashi, and A. Kunioka. Photoluminescence Properties of Sodium Incorporated in CuInSe₂ Thin Films. *Jpn. J. Appl. Phys.*, 38:L289–L291, 1999.
- [45] M. Lammer, U. Klemm, and M. Powalla. Sodium co-evaporation for low temperature Cu(In,Ga)Se₂ deposition. *Thin Solid Films*, 387(1-2):33–36, May 2001.
- [46] B. M. Keyes, F. Hasoon, P. Dippo, A. Balcioglu, and F. Abulfotuh. Influence of Na on the electro-optical properties of Cu(In,Ga)Se₂. In *Conference Record Of The Twenty Sixth IEEE Photovoltaic Specialists Conference*, pages 479–482. Ieee, 1997.
- [47] D. J. Schroeder and A. A. Rockett. Electronic effects of sodium in epitaxial CuIn_{1-x}Ga_xSe₂. *J. Appl. Phys.*, 82(10):4982–4985, November 1997.
- [48] D. Rudmann. *Effects of sodium on growth and properties of Cu(In,Ga)Se₂ thin films and solar cells*. PhD thesis, ETH Zürich, 2004.
- [49] D. Rudmann, D. Bremaud, H. Zogg, and A. N. Tiwari. Na incorporation into Cu(In,Ga)Se₂ for high-efficiency flexible solar cells on polymer foils. *J. Appl. Phys.*, 97(8):084903, April 2005.
- [50] Z.B. Li, X. Wang, and K.L. Yao. Electronic structures and optical properties of by first-principle calculations. *Solid State Communications*, 150(33-34):1514–1517, September 2010.
- [51] Y. Yan, C.-S. Jiang, R. Noufi, Su-Huai Wei, H. R. Moutinho, and M. M. Al-Jassim. Electrically Benign Behavior of Grain Boundaries in Polycrystalline CuInSe₂ Films. *Phys. Rev. Lett.*, 99(23):235504–, December 2007.
- [52] L. Kronik, D. Cahen, and H. W. Schock. Effects of Sodium on Polycrystalline Cu(In,Ga)Se₂ and Its Solar Cell Performance. *Adv. Mater.*, 10(1):31–36, 1998.
- [53] G. Dagan, F. Abou-Elfotuh, D. J. Dunlavy, R. J. Matson, and D. Cahen. Defect level identification in copper indium selenide (CuInSe₂) from photoluminescence studies. *Chemistry of Materials*, 2(3):286–293, May 1990.

- [54] A. M. Gabor, J. R. Tuttle, D. S. Albin, M. A. Contreras, R. Noufi, and A. M. Hermann. High-efficiency CuIn_xGa_{1-x}Se₂ solar cells made from (In_x,Ga_{1-x})₂Se₃ precursor films. *Appl. Phys. Lett.*, 65(2):198–200, July 1994.
- [55] C. A. Kaufmann, R. Caballero, T. Unold, R. Hesse, R. Klenk, S. Schorr, M. Nichterwitz, and H.-W. Schock. Depth profiling of Cu(In,Ga)Se₂ thin films grown at low temperatures. *Sol. Energy Mater. Sol. Cells*, 93(6-7):859–863, June 2009.
- [56] A. M. Gabor, J. R. Tuttle, M. H. Bode, A. Franz, A. L. Tennant, M. A. Contreras, R. Noufi, D. G. Jensen, and A. M. Hermann. Band-gap engineering in Cu(In,Ga)Se₂ thin films grown from (In,Ga)₂Se₃ precursors. *Sol. Energy Mater. Sol. Cells*, 41-42:247–260, June 1996.
- [57] R. Klenk, T. Walter, H.-W. Schock, and D. Cahen. A model for the successful growth of polycrystalline films of CuInSe₂ by multisource physical vacuum evaporation. *Adv. Mater.*, 5(2):114–119, 1993.
- [58] R. Scheer, A. Neisser, K. Sakurai, P. Fons, and S. Niki. Cu(In_{1-x}Ga_x)Se₂ growth studies by in situ spectroscopic light scattering. *Appl. Phys. Lett.*, 82(13):2091–2093, March 2003.
- [59] K. Sakurai, R. Hunger, R. Scheer, C. A. Kaufmann, A. Yamada, T. Baba, Y. Kimura, K. Matsubara, P. Fons, H. Nakanishi, and S. Niki. In situ diagnostic methods for thin-film fabrication: utilization of heat radiation and light scattering. *Prog. Photovolt: Res. Appl.*, 12(2-3):219–234, 2004.
- [60] L. K. Fionova and A. V. Artemyev. *Grain Boundaries in Metals and Semiconductors*. Les Editions de Physique, France, 1993.
- [61] T. I. Kamins. Hall Mobility in Chemically Deposited Polycrystalline Silicon. *J. Appl. Phys.*, 42(11):4357–4365, October 1971.
- [62] M. E. Cowher and T. O. Sedgwick. Chemical Vapor Deposited Polycrystalline Silicon. *J. Electrochem. Soc.*, 119(11):1565–1570, November 1972.
- [63] A. L. Fripp and L. H. Slack. Resistivity of Doped Polycrystalline Silicon Films. *J. Electrochem. Soc.*, 120(1):145–146, January 1973.

- [64] W. Siegel, G. Kühnel, and H. A. Schneider. On the determination of the carrier concentration in large-grain polycrystalline InP, GaAs, and GaP by Hall effect measurements. *phys. stat. sol. (a)*, 87(2):673–681, 1985.
- [65] Y. H. Lo, J. M. Hong, M. C. Wu, and S. Wang. The transport and isolation properties of polycrystalline GaAs selectively grown by molecular beam epitaxy. *Electron Device Letters, IEEE*, 7(10):586–588, 1986.
- [66] M. K. Sharma and D. P. Joshi. Electrical conduction model for polycrystalline GaAs films. *J. Appl. Phys.*, 102(3):033704–7, August 2007.
- [67] Y. Sato, J. P. Buban, T. Mizoguchi, N. Shibata, M. Yodogawa, T. Yamamoto, and Y. Ikuhara. Role of Pr Segregation in Acceptor-State Formation at ZnO Grain Boundaries. *Phys. Rev. Lett.*, 97(10):106802–, September 2006.
- [68] Iris Visoly-Fisher, Sidney R. Cohen, and David Cahen. Direct evidence for grain-boundary depletion in polycrystalline CdTe from nanoscale-resolved measurements. *Appl. Phys. Lett.*, 82(4):556–558, January 2003.
- [69] I. Visoly-Fisher, S.R. Cohen, A. Ruzin, and D. Cahen. How Polycrystalline Devices Can Outperform Single-Crystal Ones: Thin Film CdTe/CdS Solar Cells. *Advanced Materials*, 16(11):879–883, 2004.
- [70] I. Visoly-Fisher, S. Cohen, K. Gartsman, A. Ruzin, and D. Cahen. Understanding the Beneficial Role of Grain Boundaries in Polycrystalline Solar Cells from Single-Grain-Boundary Scanning Probe Microscopy. *Adv. Funct. Mater.*, 16(5):649–660, 2006.
- [71] M. Krejci, A. N. Tiwari, H. Zogg, P. Schwander, H. Heinrich, and G. Kostorz. Rotational twins in heteroepitaxial CuInSe₂ layers on Si(111). *J. Appl. Phys.*, 81(9):6100–6106, May 1997.
- [72] Y. Yan, R. Noufi, and M. M. Al-Jassim. Grain-Boundary Physics in Polycrystalline CuInSe₂ Revisited: Experiment and Theory. *Phys. Rev. Lett.*, 96(20):205501–, May 2006.
- [73] Y. Yan, K.M. Jones, C.S. Jiang, X.Z. Wu, R. Noufi, and M.M. Al-Jassim. Understanding the defect physics in polycrystalline photovoltaic materials. *Physica B: Condensed Matter*, 401-402:25–32, December 2007.

- [74] D. Cahen and R. Noufi. Defect chemical explanation for the effect of air anneal on CdS/CuInSe₂ solar cell performance. *Appl. Phys. Lett.*, 54(6):558–560, February 1989.
- [75] L. Kronik, U. Rau, J.-F. Guillemoles, D. Braunger, H.-W. Schock, and D. Cahen. Interface redox engineering of Cu(In,Ga)Se₂ - based solar cells: oxygen, sodium, and chemical bath effects. *Thin Solid Films*, 361-362:353–359, February 2000.
- [76] D. Liao and A. Rockett. Epitaxial growth of Cu(In, Ga)Se₂ on GaAs(110). *J. Appl. Phys.*, 91(4):1978–1983, February 2002.
- [77] J. E. Jaffe and A. Zunger. Defect-induced nonpolar-to-polar transition at the surface of chalcopyrite semiconductors. *Phys. Rev. B*, 64(24):241304–, November 2001.
- [78] S. B. Zhang and S.-H. Wei. Reconstruction and energetics of the polar (112) and ($\overline{1}\overline{1}2$) versus the nonpolar (220) surfaces of CuInSe₂. *Phys. Rev. B*, 65(8):081402–, February 2002.
- [79] J. Y. W. Seto. The electrical properties of polycrystalline silicon films. *J. Appl. Phys.*, 46(12):5247–5254, 1975.
- [80] S. Sadewasser, Th. Glatzel, S. Schuler, S. Nishiwaki, R. Kaigawa, and M. Ch. Lux-Steiner. Kelvin probe force microscopy for the nano scale characterization of chalcopyrite solar cell materials and devices. *Thin Solid Films*, 431-432:257–261, May 2003.
- [81] W. K. Metzger and M. Gloeckler. The impact of charged grain boundaries on thin-film solar cells and characterization. *J. Appl. Phys.*, 98(6):063701, 2005.
- [82] M. Gloeckler, J. R. Sites, and W. K. Metzger. Grain-boundary recombination in Cu(In,Ga)Se₂ solar cells. *J. Appl. Phys.*, 98(11):113704, 2005.
- [83] D. Azulay, O. Millo, I. Balberg, H.-W. Schock, I. Visoly-Fisher, and D. Cahen. Current routes in polycrystalline CuInSe₂ and Cu(In,Ga)Se₂ films. *Sol. Energy Mater. Sol. Cells*, 91(1):85–90, January 2007.
- [84] M. Hafemeister, S. Siebentritt, J. Albert, M. Ch. Lux-Steiner, and S. Sadewasser. Large Neutral Barrier at Grain Boundaries in Chalcopyrite Thin Films. *Phys. Rev. Lett.*, 104(19):196602–, May 2010.

- [85] S. Siebentritt, S. Sadewasser, M. Wimmer, C. Leendertz, T. Eisenbarth, and M. C. Lux-Steiner. Evidence for a Neutral Grain-Boundary Barrier in Chalcopyrites. *Phys. Rev. Lett.*, 97(14):146601–, October 2006.
- [86] N. C.-C. Lu, L. Gerzberg, C.-Y. Lu, and J. D. Meindl. A conduction model for semiconductor-grain-boundary-semiconductor barriers in polycrystalline-silicon films. *Electron Devices, IEEE Transactions*, 30(2):137–149, 1983.
- [87] C. Lei, C. M. Li, A. Rockett, and I. M. Robertson. Grain boundary compositions in Cu(InGa)Se₂. *J. Appl. Phys.*, 101(2):024909–7, January 2007.
- [88] M. J. Hetzer, Y. M. Strzhemechny, M. Gao, M. A. Contreras, A. Zunger, and L. J. Brillson. Direct observation of copper depletion and potential changes at copper indium gallium diselenide grain boundaries. *Appl. Phys. Lett.*, 86(16):162105–3, April 2005.
- [89] D. W. Niles, M. Al-Jassim, and K. Ramanathan. Direct observation of Na and O impurities at grain surfaces of CuInSe₂ thin films. *J. Vac. Sci. Technol. A*, 17(1):291–296, January 1999.
- [90] N. Ott, G. Hanna, U. Rau, J. H. Werner, and H. P. Strunk. Texture of Cu(In,Ga)Se₂ thin films and nanoscale cathodoluminescence. *Journal of Physics: Condensed Matter*, 16(2):S85, 2004.
- [91] M. J. Romero, K. Ramanathan, M. A. Contreras, M. M. Al-Jassim, R. Noufi, and P. Sheldon. Cathodoluminescence of Cu(In,Ga)Se₂ thin films used in high-efficiency solar cells. *Appl. Phys. Lett.*, 83(23):4770–4772, December 2003.
- [92] D. Abou-Ras, C. T. Koch, V. Küstner, P. A. van Aken, U. Jahn, M. A. Contreras, R. Caballero, C. A. Kaufmann, R. Scheer, T. Unold, and H.-W. Schock. Grain-boundary types in chalcopyrite-type thin films and their correlations with film texture and electrical properties. *Thin Solid Films*, 517(7):2545 – 2549, 2009.
- [93] G. Hanna, T. Glatzel, S. Sadewasser, N. Ott, H. P. Strunk, U. Rau, and J. H. Werner. Texture and electronic activity of grain boundaries in Cu(In,Ga)Se₂ thin films. *Applied Physics A: Materials Science & Processing*, 82:1–7, 2006.
- [94] J. Kavalakkatt. Elektrische Eigenschaften von Korngrenzen in Chalkopyrithalbleitern. Master's thesis, Technische Universität Berlin, 2010.

- [95] M. Nichterwitz, D. Abou-Ras, K. Sakurai, J. Bundesmann, T. Unold, R. Scheer, and H.-W. Schock. Influence of grain boundaries on current collection in Cu(In,Ga)Se₂ thin-film solar cells. *Thin Solid Films*, 517(7):2554–2557, February 2009.
- [96] E. Cadel, N. Barreau, J. Kessler, and P. Pareige. Atom probe study of sodium distribution in polycrystalline Cu(In,Ga)Se₂ thin film. *Acta Materialia*, 58(7):2634–2637, April 2010.
- [97] S. Sadewasser. Microscopic characterization of individual grain boundaries in Cu-III-VI₂ chalcopyrites. *Thin Solid Films*, 515(15):6136–6141, May 2007.
- [98] D. Fuertes Marrón, S. Sadewasser, A. Meeder, Th. Glatzel, and M. Ch. Lux-Steiner. Electrical activity at grain boundaries of Cu(In,Ga)Se₂ thin films. *Phys. Rev. B*, 71(3):033306–, January 2005.
- [99] C. Leendertz, F. Streicher, M. Ch. Lux-Steiner, and S. Sadewasser. Evaluation of kelvin probe force microscopy for imaging grain boundaries in chalcopyrite thin films. *Appl. Phys. Lett.*, 89(11):113120–3, September 2006.
- [100] C.-S. Jiang, R. Noufi, J. A. AbuShama, K. Ramanathan, H. R. Moutinho, J. Pankow, and M. M. Al-Jassim. Local built-in potential on grain boundary of cu(in,ga)se₂ thin films. *Appl. Phys. Lett.*, 84(18):3477–3479, May 2004.
- [101] C.-S Jiang, R. Noufi, K. Ramanathan, J. A. AbuShama, H. R. Moutinho, and M. M. Al-Jassim. Does the local built-in potential on grain boundaries of Cu(In,Ga)Se₂ thin films benefit photovoltaic performance of the device? *Appl. Phys. Lett.*, 85(13):2625–2627, September 2004.
- [102] S. Siebentritt, T. Eisenbarth, M. Wimmer, C. Leendertz, F. Streicher, S. Sadewasser, and M. C. Lux-Steiner. A Σ3 grain boundary in an epitaxial chalcopyrite film. *Thin Solid Films*, 515(15):6168–6171, May 2007.
- [103] R. Mainz, F. Streicher, D. Abou-Ras, S. Sadewasser, R. Klenk, and M. C. Lux-Steiner. Combined analysis of spatially resolved electronic structure and composition on a cross-section of a thin film Cu(In_{1-x}Ga_x)S₂ solar cell. *phys. stat. sol. (a)*, 206(5):1017–1020, 2009.
- [104] M. J. Romero, C.-S. Jiang, R. Noufi, and M. Al-Jassim. Photon emission in CuInSe₂ thin films observed by scanning tunneling microscopy. *Appl. Phys. Lett.*, 86(14):143115–3, April 2005.

- [105] M. J. Romero, C.-S. Jiang, R. Noufi, and M. Al-Jassim. Lateral electron transport in Cu(In,Ga)Se₂ investigated by electro-assisted scanning tunneling microscopy. *Appl. Phys. Lett.*, 87(17):172106–3, October 2005.
- [106] M. J. Romero, C.-S. Jiang, J. Abushama, H. R. Moutinho, M. M. Al-Jassim, and R. Noufi. Electroluminescence mapping of CuGaSe₂ solar cells by atomic force microscopy. *Appl. Phys. Lett.*, 89(14):143120–3, October 2006.
- [107] T. Datta, R. Noufi, and S. K. Deb. Electrical conductivity of p-type CuInSe₂ thin films. *Appl. Phys. Lett.*, 47(10):1102–1104, November 1985.
- [108] R. Chakrabarti, B. Maiti, S. Chaudhuri, and A.K. Pal. Photoconductivity of Cu(In, Ga)Se₂ films. *Sol. Energy Mater. Sol. Cells*, 43(3):237–247, October 1996.
- [109] A. Virtuani, E. Lotter, M. Powalla, U. Rau, J. H. Werner, and M. Acciarri. Influence of Cu content on electronic transport and shunting behavior of Cu(In,Ga)Se₂ solar cells. *J. Appl. Phys.*, 99(1):014906–11, January 2006.
- [110] T. B. Rissom. *Elektrische Transporteigenschaften von epitaktischen und polykristallinen Chalkopyrit-Schichten*. PhD thesis, Freie Universität Berlin, 2007.
- [111] S. Schuler, S. Nishiwaki, J. Beckmann, N. Rega, S. Brehme, S. Siebentritt, and M. C. Lux-Steiner. Charge carrier transport in polycrystalline CuGaSe₂ thin films. In *Conference Record Of The Twenty-Ninth IEEE Photovoltaic Specialists Conference 2002*, pages 504–507, 2002.
- [112] S. Siebentritt and S. Schuler. Defects and transport in the wide gap chalcopyrite CuGaSe₂. *J. Phys. Chem. Solids*, 64(9-10):1621–1626, September 2003.
- [113] R. Caballero, V. Izquierdo-Roca, X. Fontané, C.A. Kaufmann, J. Álvarez García, A. Eicke, L. Calvo-Barrio, A. Pérez-Rodríguez, H. W. Schock, and J. R. Morante. Cu deficiency in multi-stage co-evaporated Cu(In,Ga)Se₂ for solar cells applications: Microstructure and Ga in-depth alloying. *Acta Materialia*, 58(9):3468–3476, May 2010.
- [114] H. Alexander. *Physikalische Grundlagen der Elektronenmikroskopie*. B. G. Teubner, Stuttgart, 1997.
- [115] J. C H. Spence and J. M. Zuo. *Electron Microdiffraction*. Springer, 1992.

- [116] D. Gabor. A new microscopic principle. *Nature*, 161(4098):777–778, 1948.
- [117] J. M. Cowley. Twenty forms of electron holography. *Ultramicroscopy*, 41(4):335–348, June 1992.
- [118] C. T. Koch and A. Lubk. Off-axis and inline electron holography: A quantitative comparison. *Ultramicroscopy*, 110(5):460–471, April 2010.
- [119] T. Latychevskaia, P. Formanek, C. T. Koch, and A. Lubk. Off-axis and inline electron holography: Experimental comparison. *Ultramicroscopy*, 110(5):472–482, April 2010.
- [120] H. Lichte and M. Lehmann. Electron holography–basics and applications. *Rep. Prog. Phys.*, 71(1):016102–, 2008.
- [121] G. Möllenstedt and H. Düker. Beobachtungen und Messungen an Biprisma-Interferenzen mit Elektronenwellen. *Z. Phys.*, 145(3):377–397, 1956.
- [122] D. Geiger, H. Lichte, M. Linck, and M. Lehmann. Electron Holography with a C_s -Corrected Transmission Electron Microscope. *Microsc. Microanal.*, 14(01):68–81, 2008.
- [123] M. Lehmann and H. Lichte. Tutorial on off-axis electron holography. *Microsc. Microanal.*, 8(6):447–466, December 2002.
- [124] D. Van Dyck, H. Lichte, and J. C. H. Spence. Inelastic scattering and holography. *Ultramicroscopy*, 81(3-4):187–194, April 2000.
- [125] M. Lehmann. Influence of the elliptical illumination on acquisition and correction of coherent aberrations in high-resolution electron holography. *Ultramicroscopy*, 100(1-2):9–23, July 2004.
- [126] H. Lichte, K. H. Hermann, and F. Lenz. Electron Noise In Off-Axis Image Plane Holography. *Optik*, 77(3):135–140, October 1987.
- [127] A. Harscher and H. Lichte. Experimental study of amplitude and phase detection limits in electron holography. *Ultramicroscopy*, 64(1-4):57–66, August 1996.
- [128] L. J. Allen, H. M. L. Faulkner, K. A. Nugent, M. P. Oxley, and D. Paganin. Phase retrieval from images in the presence of first-order vortices. *Phys. Rev. E*, 63(3):037602, March 2001.

- [129] L. A. Bursill, J. C. Barry, and P. R. W. Hudson. Fresnel diffraction at (100) platelets in diamond - attempt at defect structure-analysis by high-resolution (3 Å) phase-contrast microscopy. *Phil. Mag. A*, 37(6):789–812, 1978.
- [130] M. Rühle and S. L. Sass. The detection of the change in mean inner potential at dislocations in grain-boundaries in nio. *Phil. Mag. A*, 49(6):759–782, 1984.
- [131] D. R. Rasmussen and C. B. Carter. On the fresnel-fringe technique for the analysis of interfacial films. *Ultramicroscopy*, 32(4):337 – 348, 1990.
- [132] F. Kara, R. E. Dunin-Borkowski, C. B. Boothroyd, J. A. Little, and W. M. Stobbs. Fresnel contrast analysis of composition changes and space charge at grain boundaries in mullite. *Ultramicroscopy*, 66(1-2):59–71, November 1996.
- [133] R. E. Dunin-Borkowski. The development of fresnel contrast analysis, and the interpretation of mean inner potential profiles at interfaces. *Ultramicroscopy*, 83(3-4):193–216, June 2000.
- [134] K. Ishizuka. Contrast transfer of crystal images in TEM. *Ultramicroscopy*, 5(1-3):55–65, 1980.
- [135] C. T. Koch. A flux-preserving non-linear inline holography reconstruction algorithm for partially coherent electrons. *Ultramicroscopy*, 108(2):141–150, 2008.
- [136] S. Bhattacharyya, C. T. Koch, and M. Rühle. Projected potential profiles across interfaces obtained by reconstructing the exit face wave function from through focal series. *Ultramicroscopy*, 106(6):525–538, 2006.
- [137] H. Düker. Lichtstarke Interferenzen mit einem Biprisma für Elektronenwellen. *Zeitschrift Für Naturforschung Part A*, 10(3):256–257, 1955.
- [138] A. Lubk, D. Wolf, and H. Lichte. The effect of dynamical scattering in off-axis holographic mean inner potential and inelastic mean free path measurements. *Ultramicroscopy*, 110(5):438–446, April 2010.
- [139] S. Raimes. *The Wave Mechanics of Electrons in Metals*. North-Holland Pub. Co. : Interscience, Amsterdam, 1961.
- [140] W. D. Rau, P. Schwander, F. H. Baumann, W. Hppner, and A. Ourmazd. Two-Dimensional Mapping of the Electrostatic Potential in Transistors by Electron Holography. *Phys. Rev. Lett.*, 82(12):2614–, March 1999.

- [141] R. F. Egerton and S. C. Cheng. Measurement of local thickness by electron energy-loss spectroscopy. *Ultramicroscopy*, 21(3):231 – 244, 1987.
- [142] R. F. Egerton. *Electron Energy-Loss Spectroscopy in the Electron Microscope*. Plenum Press, New York, 1996.
- [143] R. F. Egerton and M. Malac. EELS in the TEM. *Journal of Electron Spectroscopy and Related Phenomena*, 143(2-3):43–50, 2005.
- [144] W. Sigle. Analytical transmission electron microscopy. *Annual Review of Materials Research*, 35(1):239–314, 2005.
- [145] L. Reimer, U. Zepke, J. Moesch, S. Schulze-Hillert, M. Ross-Messemmer, W. Probst, and E. Weimer. *A Reference Handbook of Standard Data for Identification and Interpretation of Electron Energy Loss Spectra and for Generation of Electron Spectroscopic Images*. Carl Zeiss, Oberkochen, 1992.
- [146] M. Watanabe, D. B. Williams, and M. G. Burke. Atomic-level analytical electron microscopy of diffusional phase transformations. In *Proc. Inter. Conf. on Solid-Solid Phase Transformations in Inorganic Materials 2005, Vol. 2*, volume 2, pages 431–442. Minerals, Metals & Materials Soc, 2005.
- [147] D. B. Williams and C. B. Carter. *Transmission Electron Microscopy*. Springer, 2009.
- [148] <http://temsample.in2p3.fr/>.
- [149] T. F. Kelly and M. K. Miller. Invited review article: Atom probe tomography. *Review Of Scientific Instruments*, 78(3):031101, March 2007.
- [150] S. M. Sze and K. K. Ng. *Physics of Semiconductor Devices*. John Wiley & Sons, 2006.
- [151] H. Föll. Semiconductors I, 2005. lecture notes.
- [152] D. B. Holt and D. C. Joy. *SEM microcharacterization of semiconductors*. Academic Press, 1989.
- [153] H. Bethe. Zur Theorie des Durchgangs schneller Korpuskularstrahlen durch Materie. *Annalen der Physik*, 397(3):325–400, 1930.
- [154] M. Born. Quantenmechanik der Stossvorgänge. *Zeitschrift für Physik A Hadrons and Nuclei*, 38(11):803–827, November 1926.

- [155] S. M. Seltzer and M. J. Berger. Evaluation of the collision stopping power of elements and compounds for electrons and positrons. *Int. J. Appl. Radiat. Isot.*, 33(11):1189 – 1218, 1982.
- [156] S. M. Seltzer and M. J. Berger. Procedure for calculating the radiation stopping power for electrons. *Int. J. Appl. Radiat. Isot.*, 33(11):1219 – 1226, 1982.
- [157] E. Fermi. The Ionization Loss of Energy in Gases and in Condensed Materials. *Phys. Rev.*, 57(6):485–, March 1940.
- [158] R. M. Sternheimer and R. F. Peierls. General Expression for the Density Effect for the Ionization Loss of Charged Particles. *Phys. Rev. B*, 3(11):3681, June 1971.
- [159] W. H. Bragg and R. Kleeman. On the α particles of radium, and their loss of range in passing through various atoms and molecules. *Philos. Mag. Series 6*, 10(57):318–340, 1905.
- [160] K. Puech, S. Zott, K. Leo, M. Ruckh, and H.-W. Schock. Determination of minority carrier lifetimes in CuInSe₂ thin films. *Appl. Phys. Lett.*, 69(22):3375–3377, November 1996.
- [161] T. Unold, J. Klaer, and W. K. Metzger. Minority carrier lifetime in Cu(In,Ga)S₂ thin films and solar cells. unpublished.
- [162] M. V. Yakushev, R. W. Martin, A. V. Mudryi, and A. V. Ivaniukovich. Excited states of the A free exciton in CuInS₂. *Appl. Phys. Lett.*, 92(11):111908–3, March 2008.
- [163] M. V. Yakushev, F. Luckert, C. Faugeras, A. V. Karotki, A. V. Mudryi, and R. W. Martin. Excited states of the free excitons in CuInSe₂ single crystals. *Appl. Phys. Lett.*, 97(15):152110–3, October 2010.
- [164] M. Burgelman, P. Nollet, and S. Degraeve. Modelling polycrystalline semiconductor solar cells. *Thin Solid Films*, 361-362:527–532, February 2000.
- [165] Siegfried Hunklinger. *Festkörperphysik*. Oldenbourg, 2007.
- [166] A. P. Sutton and R. W. Balluffi. *Interfaces in Crystalline Materials*. Oxford University Press, 1995.

- [167] W. Shockley and W. T. Read. Statistics of the recombinations of holes and electrons. *Phys. Rev.*, 87(5):835–842, 1952.
- [168] L. D. Landau, A. M. Kosevich, and E. M. Lifshitz. *Theory of Elasticity (Theoretical Physics, Vol 7)*. Butterworth Heinemann, 1984.
- [169] B. Fernandez and S. M. Wasim. Sound Velocities and Elastic Moduli in CuInTe₂ and CuInSe₂. *phys. stat. sol. (a)*, 122(1):235–242, 1990.
- [170] J. A. Ibers. Atomic scattering amplitudes for electrons. *Acta Crystallographica*, 11(3):178–183, Mar 1958.
- [171] D. Rez, P. Rez, and I. Grant. Dirac–Fock calculations of X-ray scattering factors and contributions to the mean inner potential for electron scattering. *Acta Crystallogr. Sect. A*, 50(4):481–497, Jul 1994.
- [172] L.-M. Peng. Electron scattering factors of ions and their parameterization. *Acta Crystallogr. Sect. A*, 54(4):481–485, Jul 1998.
- [173] P. A. Doyle and P. S. Turner. Relativistic Hartree–Fock X-ray and electron scattering factors. *Acta Crystallogr. Sect. A*, 24(3):390–397, May 1968.
- [174] A. Weickenmeier and H. Kohl. Computation of absorptive form factors for high-energy electron diffraction. *Acta Crystallogr. Sect. A*, 47(5):590–597, Sep 1991.
- [175] S. Lehmann. *Leerstellen-Verbindungen im System Cu-Ga-Se: Eine strukturelle Studie an Kompakt- und Schichtmaterial*. PhD thesis, Freie Universität Berlin, 2007.
- [176] S. Lehmann. personal communications: $a = 5.75555(1)$, $c = 11.530307(1)$. personal communications: $a = 5.75555(1)$, $c = 11.530307(1)$.
- [177] S. Lehmann, D. Fuertes Marrón, M. León, R. Feyerherm, E. Dudzik, E. J. Friedrich, M. Tovar, Y. Tomm, C. Wolf, S. Schorr, Th. Schedel-Niedrig, M. Ch. Lux-Steiner, and J. M. Merino. Long-range structure of Cu(In_xGa_{1-x})₃Se₅: A complementary neutron and anomalous x-ray diffraction study. *J. Appl. Phys.*, 109(1):013518–11, January 2011.
- [178] D. Abou-Ras, S. Schorr, and H. W. Schock. Grain-size distributions and grain boundaries of chalcopyrite-type thin films. *Journal of Applied Crystallography*, 40(5):841–848, Oct 2007.

- [179] N. I. Medvedeva, E. V. Shalaeva, M. V. Kuznetsov, and M. V. Yakushev. First-principles study of deformation behavior and structural defects in CuInSe₂ and Cu(In,Ga)Se₂. *Phys. Rev. B*, 73(3):035207, January 2006.
- [180] P. A. Stadelmann. EMS - a software package for electron diffraction analysis and HREM image simulation in materials science. *Ultramicroscopy*, 21(2):131 – 145, 1987.
- [181] S. L. Dudarev, L. M. Peng, and M. J. Whelan. On the Doyle-Turner representation of the optical-potential for RHEED calculations. *Surface Science*, 330(1):86–100, June 1995.
- [182] G. Pozzi. The influence of the external field on transmission electron microscopy observations of electric fields at interfaces. *Journal of Physics D: Applied Physics*, 29(7):1807, 1996.
- [183] R. E. Dunin-Borkowski and W. O. Saxton. The Electrostatic Contribution to the Forward-Scattering Potential at a Space Charge Layer in High-Energy Electron Diffraction. II. Fringing Fields. *Acta Crystallogr. Sect. A*, 53(2):242–250, 1997.
- [184] U. Rau, D. Braunger, R. Herberholz, H. W. Schock, J.-F. Guillemoles, L. Kronik, and David Cahen. Oxygenation and air-annealing effects on the electronic properties of Cu(In,Ga)Se₂ films and devices. *J. Appl. Phys.*, 86(1):497–505, 1999.
- [185] C. T. Koch. Determination of grain boundary potentials in ceramics: Combining impedance spectroscopy and inline electron holography. *Int. J. Mater. Res.*, 101(1):43–49, January 2010.
- [186] V. Ravikumar, R. P. Rodrigues, and Vinayak P. Dravid. Direct Imaging of Spatially Varying Potential and Charge across Internal Interfaces in Solids. *Phys. Rev. Lett.*, 75(22):4063, November 1995.
- [187] V. Ravikumar, R. P. Rodrigues, and V. P. Dravid. An investigation of acceptor-doped grain boundaries in SrTiO₃. *Journal of Physics D: Applied Physics*, 29(7):1799–1806, 1996.
- [188] V. Ravikumar, R. P. Rodrigues, and V. P. Dravid. Space-charge distribution across internal interfaces in electroceramics using electron holography. 1. Pristine grain boundaries. *J. Am. Ceram. Soc.*, 80(5):1117–1130, May 1997.

- [189] V. Ravikumar, R. P. Rodrigues, and V. P. Dravid. Space-charge distribution across internal interfaces in electroceramics using electron holography. 2. Doped grain boundaries. *J. Am. Ceram. Soc.*, 80(5):1131–1138, May 1997.
- [190] Z. G. Mao, R. E. Dunin-Borkowski, C. B. Boothroyd, and K. M. Knowles. Direct measurement and interpretation of electrostatic potentials at 24 degrees [001] tilt boundaries in undoped and niobium-doped strontium titanate bicrystals. *J. Am. Ceram. Soc.*, 81(11):2917–2926, November 1998.
- [191] K. Gartsman, L. Chernyak, V. Lyahovitskaya, D. Cahen, V. Didik, V. Kozlovsky, R. Malkovich, E. Skoryatina, and V. Usacheva. Direct evidence for diffusion and electromigration of Cu in CuInSe₂. *J. Appl. Phys.*, 82(9):4282–4285, November 1997.
- [192] O. C. Hellman, J. A. Vandebroucke, J. Rusing, D. Isheim, and D. N. Seidman. Analysis of three-dimensional atom-probe data by the proximity histogram. *Microsc. Microanal.*, 6(5):437–444, September 2000.
- [193] S. B. Zhang, S. H. Wei, and A. Zunger. Stabilization of ternary compounds via ordered arrays of defect pairs. *Phys. Rev. Lett.*, 78(21):4059–4062, May 1997.
- [194] P. E. Flewitt and R. K. Wild. *Grain Boundaries: Their Microstructure and Chemistry*. John Wiley & Sons, 2001.
- [195] K. Tarett and U. Rau. Numerical simulation of carrier collection and recombination at grain boundaries in Cu(In,Ga)Se₂ solar cells. *J. Appl. Phys.*, 103(9):094523–11, May 2008.
- [196] R. Herberholz, U. Rau, H.W. Schock, T. Haalboom, T. Gödecke, F. Ernst, C. Beilharz, K.W. Benz, and D. Cahen. Phase segregation, Cu migration and junction formation in Cu(In,Ga)Se₂. *Eur. Phys. J. Appl. Phys.*, 6(2):131–139, 1999.

Acknowledgments

I would like to acknowledge everybody who helped and supported me during the last three years:

At first, I would like to thank Prof. Dr. Hans-Werner Schock for giving me the opportunity to perform my doctoral thesis at the Helmholtz-Zentrum, for supervising, and supporting me. I would also like to express my thanks to Prof. Dr. Bernd Rech who acted as additional supervisor. Prof. Dr. Hannes Lichte I would like to thank for accepting to perform as external supervisor of my thesis, and for the critical and helpful discussions on my work.

I would like to express my special thanks to my tutor Dr. Daniel Abou-Ras, who always supported me. His good mood, motivation, advice and vision always encouraged me. Dr. Thomas Unold, the head of our “analytics“ group, I would like to thank for the valuable discussions on the basic physics of our work.

Dr. Christoph T. Koch, Dr. Bernhard Schaffer, and John Sandino, I would like to acknowledge for the fruitful cooperation and for sharing their expertise on their TEM methods.

I would also like to thank: Dr. Markus Wollgarten for introducing me to TEM and his help with technical problems, Peter Schubert-Bischoff and Ulrike Bloeck for the introduction into and their help with TEM specimen preparation, especially with respect to my special requirements, and Holger Kropf, Miroslava Schaffer and Jens Dietrich for their effort in FIB preparation of TEM specimens. Dr. Björn Marsen I would like to thank for his help with the modeling of the grain boundaries and image simulation.

Dr. Raquel Caballero, Dr. Thorsten Rissom, Joachim Klaer, Carola Kelch and Michael Kirsch I would like to express my thanks for providing me the solar cells.

Special thanks also to all my coworkers and friends at the institute E-I3 who contributed to the pleasant work atmosphere, especially to my roommate Melanie Nichterwitz for being a fabulous colleague and friend, and for correcting my thesis.

The time at the institute would not have been half as nice without my running buddies Melanie, Sonia, Dieter, Stephan, Julian, Sascha, Christian, Daniel, Ole. Thank you for the exhausting or relaxing 6 - 42K.

I would also like to acknowledge my flatmates for the great time I could spend with them, their support and patience, especially at the end of the thesis.

Special thanks to Achim, who put a lot of effort into correcting my English.

Last but not least, I would like to thank my parents and my dear Cari for their ongoing support.

Ich versichere an Eides statt, dass ich diese Dissertation selbstständig verfasst habe. Die benutzten Hilfsmittel und Quellen sind in der Arbeit vollständig angegeben. Die Dissertation ist bis auf die gekennzeichneten Teile noch nicht veröffentlicht worden. Ich habe weder früher noch gleichzeitig ein Promotionsverfahren bei einem anderen Fachbereich bzw. einer anderen Hochschule beantragt.

Berlin, den 31. Januar 2011

.....

Sebastian Simon Schmidt

